Title

Ultrafast Dynamics of Adenine Derivatives Studied by Time-Resolved Photoelectron Spectroscopy in Water Microjets

Author

Williams, Holly Lynn

Publication Date

2017

Ultrafast Dynamics of Adenine Derivatives Studied by Time-Resolved Photoelectron Spectroscopy in Water Microjets

by

Holly Lynn Williams

A dissertation submitted in partial satisfaction of the

requirements for the degree of

Doctor of Philosophy

in

Chemistry

in the

Graduate Division

of the

University of California, Berkeley

Committee in charge:

Professor Daniel M. Neumark, Chair
Professor Richard J. Saykally
Professor Roger W. Falcone

Fall 2017

Ultrafast Dynamics of Adenine Derivatives Studied by Time-Resolved Photoelectron Spectroscopy in Water Microjets

by

Holly Lynn Williams

Abstract

Ultrafast Dynamics of Adenine Derivatives Studied by Time-Resolved Photoelectron Spectroscopy in Water Microjets

by

Holly Lynn Williams

Doctor of Philosophy in Chemistry

University of California, Berkeley

Professor Daniel M. Neumark, Chair

Femtosecond time-resolved photoelectron spectroscopy (TRPES) in liquid microjets is a powerful tool for elucidating the ultrafast photoinduced dynamics of species in the condensed phase. A pump pulse first excites the molecule of interest and is then followed by a probe pulse, which detaches the nascent electron distribution to vacuum at varying time-delays. The transient lifetimes, solvation timescales, and binding energies of the molecule can then be elucidated by tracking the time-evolving photoelectron distribution with a magnetic bottle time-of-flight spectrometer.

Of particular interest to many fields of chemistry and biology is the process by which DNA and its nucleic acid (NA) constituents shed excess energy imparted by UV radiation. Beyond their intrinsic interest, study of UV-photoexcited NA constituents can also provide fundamental insights into the non-adiabatic processes of organic molecules generally. DNA components are known to undergo rapid de-excitation through a slew of conical intersections that involve ring-puckering modes of the nitrogenous base. Importantly, the local environment and small structural changes in the NA constituent are known to drastically affect these dynamics. For this reason, a bottom-up approach to DNA photophysics is necessary.

This dissertation explores the photodeactivation of the NA constituents adenosine and adenosine monophosphate in aqueous solution. In a series of pseudo-degenerate experiments, 4.69-4.97eV and 6.20eV photons were used as both the pump and probe pulses. The lowest $\pi\pi^*$ excited state was populated by photons ranging in energy from 4.69-4.97eV, and this state was found to decay *via* internal conversion to vibrationally hot ground state on a sub-ps

timescale. Another non-adiabatic channel was seen at an excitation energy of 6.20eV, and was tentatively assigned to the decay of a higher-lying $\pi\pi^*$ excited state.

These experiments mark the first reported use of a 6.20eV pulse to study the photoinduced dynamics in NA constituents with TRPES in liquid microjets. As a probe pulse, the 6.20eV pulse provides a fuller picture of the excited state relaxation dynamics. When used as a pump, this pulse is posited to interrogate different excited states than previously studied by others. Regardless, in both cases, information about the ground electronic state is energetically inaccessible.

The lack of information regarding the ground state dynamics of NA constituents, and, in fact, many solvated species, remains an outstanding issue for TRPES in liquid microjets. The second half of this dissertation focuses on remedying this through the implementation of a new XUV source. High harmonic generation in a semi-infinite gas cell will be used to produce a femtosecond probe pulse ranging in energy from 20-100eV. With a more energetic probe, new regimes of fundamental physical chemistry in the condensed phase will be accessible.

To Eugene and Katarzyna

Contents

List of Figures

List of Tables

Acknowledgments

I am fortunate to be surrounded by a great many people who have helped me throughout this endeavor. Their knowledge, support, and guidance have profoundly impacted me.

Dan has been a tremendous adviser, and I am humbled to have worked in his group for the past five years. His keen eye, expansive knowledge, and standards of excellence served as the crucible by which my scientific mind was refined. He also tolerated my penchant for snark, which in and of itself was a Herculean task.

I am forever indebted to our administrative assistant, Michelle Haskins, who fearlessly marched me through seemingly endless bureaucratic red tape and provided me with a steady supply of sweets. Eric Granlund, Emanuel Druga, Mark Thompson, Doug Kresse from Coherent, and the rest of the shop and facilities personnel were life-savers during "The Dark Ages." With their expertise and patience, all the broken equipment was revived.

I was incredibly lucky to work alongside Dr. Madeline Elkins and Blake Erickson on the liquid microjet project. Madeline was hugely influential and taught me all the skills that I needed in order to survive after she graduated. She is one of the best scientists I know, and I still miss her presence in lab terribly. Blake is supremely sharp and sarcastic, and has kept me on my toes since joining lab. He is an incredibly capable scientist, and I know a luminous graduate experience—one filled with XUV light—lies ahead of him.

Alice Kunin and Dr. Weili Li were also my effective femtosecond labmates, and I owe a great debt of gratitude to them. Although they were all the way at the opposite end of the hall, not a day went by that we didn't lean on each other for support, both moral and technical. Thank you for feeding me and making me laugh.

My gratitude to the Neumark group is beyond measure. In my time with the group, I have been privileged to work with outstanding scientists who I am also proud to call dear friends. In particular, Dr. Marissa Weichman has been a close friend, one who is destined for academic glory. One day I will tell my grandchildren about her, I'm sure. Dr. Neil Cole-Filipiak, Mark Shapero, and Erin Sullivan were all stalwart companions who made graduate school more bearable.

Thank you to my family and to my friends outside of the Latimer sub-basement. Dr. Tom Oliver was my friend and neighbor at the beginning of my time here at UC Berkeley, and his confidence in me always buoyed my spirits. To Kasia and my pets, thank you for keeping me sane.

Finally, thank you to my husband-to-be, Eugene. Without him, none of this would have been possible. я тебя люблю.

Part I

Introduction and Methods

Chapter 1

Introduction

1.1 Overview

The interaction of ionizing radiation with cellular material is known to produce many reactive photoproducts, and can ultimately result in genetic damage. DNA can undergo a rich variety of photoinduced processes that span multiple energy regimes and timescales.[1–3] The photostability of this macromolecule is attributed, in part, to its ability to rapidly funnel away excess energy. Acquiring a better understanding of the fundamental chemical underpinnings of this phenomenon is the central task of this dissertation.

Due to the complexity of the cellular environment, a bottom-up approach has been widely adopted to study DNA photodeactivation. Nucleic acid constituents—namely nucleobases, nucleosides, and nucleotides—have been the subject of intense scrutiny in both the gas and solution phases.[4–7] The surrounding aqueous environment has been shown to profoundly impact these systems; thus, a complete accounting of the various intra- and intermolecular effects that drive photodeactivation demands the presence of water.

This dissertation is focused on exploring the photoinduced dynamics of nucleic acid constituents using time-resolved photoelectron spectroscopy in liquid microjets. First, the theoretical foundations used in tracking non-adiabatic dynamics in the condensed phase are presented in Chapter 1. Chapter 2 details the experimental apparatus and liquid microjet engineering considerations. Then, the photodeactivation of adenosine and adenosine monohosphate in water are investigated in Chapter 3. Finally, Chapters 4 and 5 detail the design and implementation of a new table-top source of femtosecond XUV pulses for future experiments.

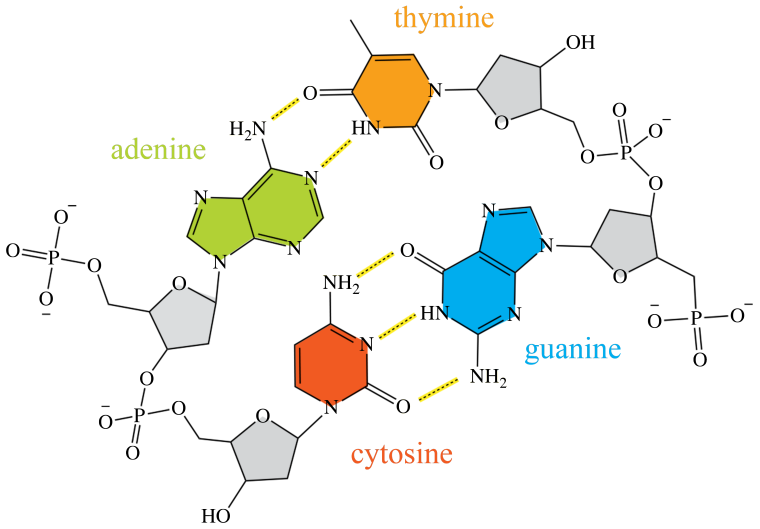

Figure 1.1: DNA double strand featuring adenine (green), thymine (orange), guanine (blue), and cytosine (red). Hydrogen bonds are indicated by dashed, highlighted bonds. The ribose moiety is shaded in grey.

1.2 Photochemistry of DNA Subunits

The building blocks of nucleic acids (NAs) are nucleotide monomers. Nucleotides comprise a nucleobase (NB)—adenine, cytosine, thymine, guanine, or uracil—that is bound to a ribose and a phosphate moiety through a glycosidic linkage. Nucleobases are aromatic heterocyclic compounds that form two distinct groups: six-membered rings called pyrimidines and fused rings called purines. To form a single stranded NA, the phosphate of one monomer connects to the ribose group of an adjacent monomer; to form a double helix, NBs of one strand hydrogen bond with their base pair on the opposite strand. Pyrimidines specifically base pair to a purine partner. The basic structure of NAs shown in Figure 1.1.

Monomers, single base pairs, stacked NBs, and NA oligomers all absorb ultraviolet (UV) light and undergo various de-excitation processes, many of which can lead to the formation of undesirable photoproducts.[8] Excess energy is removed in these systems across several timescale regimes. This is illustrated in Figure 1.2. In monomers, de-excitation occurs on a sub-ps timescale; in polynucleotides, this process occurs on a pico- to nano-second timescale. For the purposes of this dissertation, discussion of these dynamics will be restricted to monomers.

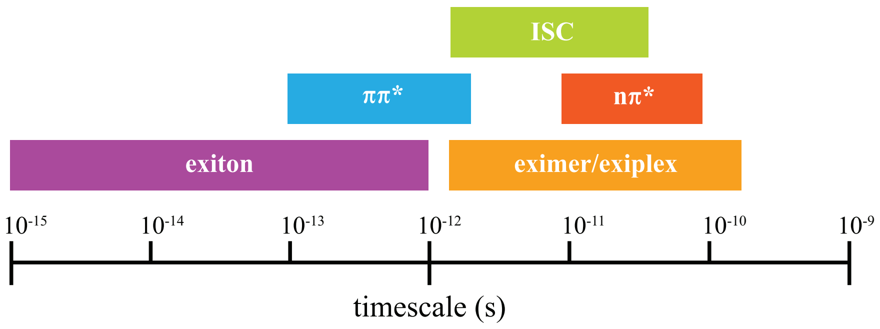

Figure 1.2: Timescales for DNA dynamics subsequent to photoexcitation at 4.7eV. Exitons, eximers, and exiplexes are excited states of stacked NAs. Monomers show both singlet excited state decay ($\pi\pi^*$ and nπ^*) and intersystem crossing (ISC) to triplet states, which persist for microseconds.

1.2.1 Absorption of UV Radiation

Nucleic acid constituents are good UV chromophores, and exhibit strong absorption cross sections in this spectral region.[1, 9] Two absorption peaks—one centered ~200nm and the other centered ~260nm—are seen in all NA constituents. The absorption spectra for several NBs are shown in Figure 1.3. Nucleosides and -tides show similar absorption spectra as their NB counterparts. In NAs, a single absorption band peaks near 260nm.

Advances in quantum chemistry calculations have enabled the study of the excited state potential energy surfaces of NA constituents in both gas and solution phases with good accuracy.[6, 7] Energy ordering of these excited states depends strongly on the environment, and thus our discussion will be constrained to the condensed phase results relevant to the liquid microjet technique described in Chapter 2. Although the relative ordering of excited states changes between gas and solution phase, the shape of the potential energy surfaces is generally invariant to environment.

Both UV absorption bands are attributed to excitation of the π system of the NB. Discussion of the electronic structure will thus be limited to NBs—these are well studied and demonstrate several characteristics common across NA constituents. Several close-lying excited states are energetically accessible near 4.7eV (260nm) and are singlet states of $\pi\pi^*$ or nπ^* character.

Transitions to the $\pi\pi^*$ states dominate the optical absorption spectra at 260nm, but the return of the electron population to the ground state has been found to involve an interplay between the $\pi\pi^*$ and nπ^* states, and possibly other triplet states. The nπ^* excited states are found to lie higher in energy than the $\pi\pi^*$ states in both pyrimidine and purine NA constituents in water. The destabilization of the nπ^* state in water can be explained by a

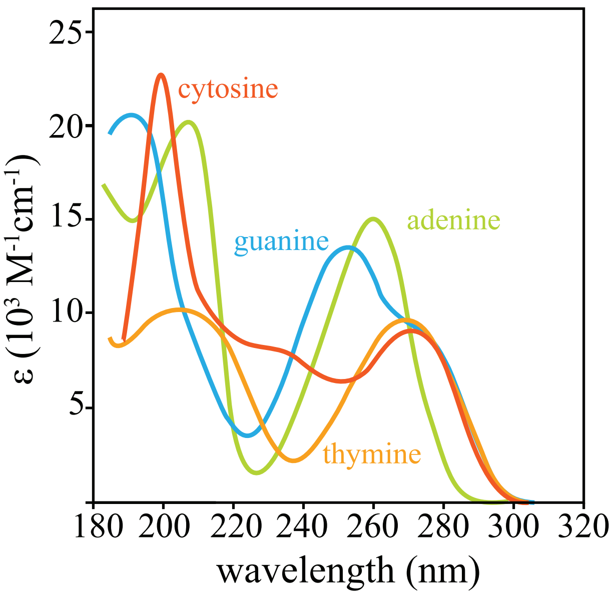

Figure 1.3: Absorption spectra for NBs and DNA. Adapted from References [1] and [5].

decrease in the solute-solvent hydrogen bond strength. Because this excitation involves the transfer of an electron from the oxygen lone pair into a π^* molecular orbital, one potential hydrogen bond donor is removed.

Nucleic acid constituents have low fluorescence yield, on the order of 10^{-4}.[1] This implies that excess energy is dissipated primarily through non-radiative means (*i.e.* bond dissociation, internal conversion). As we will see in Section 1.2.2, although the deactivation pathways of NA constituents show dependencies on the constituent composition, these systems are generally found to return to their ground states within a few picoseconds through various conical intersections (CI)—crossings between the potential energy surfaces of the initial and final states—that involve distortions of the NB ring.

1.2.2 Photoinduced Dynamics

Time-resolved pump-probe spectroscopies opened a new window into the photophysics of NA constituents, and have since been widely used in conjunction with theoretical calculations to study the dynamic behavior of these systems.[4, 5] Excited state deactivation of monomers has been found to be extremely efficient.[1] Purines and pyrimidines exhibit

---

[1] Extended polymer NA systems return to their ground states on a much longer timescale than NA constituents.

nucleobase	**lifetimes (ps)**	**pathway**
thymine	0.72	$\pi\pi^* \rightarrow S_0$
	30	$\pi\pi^* \rightarrow n\pi^* \rightarrow S_0$
cytosine	0.2	$\pi\pi^* \rightarrow S_0$
	1.3	$\pi\pi^* \rightarrow n\pi^* \rightarrow S_0$
adenine (9H)	0.18	$\pi\pi^* \rightarrow S_0$
guanine (gas phase)	0.46	$\pi\pi^* \rightarrow S_0$

Table 1.1: Excited state lifetimes for DNA NBs in aqueous solution following excitation at 250nm, as measured by femtosecond transient absorption. Guanine is not sufficiently soluble at neutral pH for study, and instead, the gas phase lifetime is provided. Adapted from References [1] and [10].

slightly different decay dynamics when photoexcited at 4.7eV, but all decay within a few picosecond timescale. Furthermore, higher photoexcitation energies have been correlated to shorter excited state decay lifetimes. This potentially indicates competitive decay channels. The measured lifetimes for NB in aqueous solution are organized in Table 1.1.

In uracil and thymine, two relaxation pathways to the ground state, S_0, have been identified following excitation at 4.7eV.[11, 12] The first directly transfers $\pi\pi^* \rightarrow S_0$. The second pathway first traps population into another excited state of nπ*character and follows $\pi\pi^* \rightarrow n\pi^* \rightarrow S_0$. Characterization of cytosine photodeactivation pathways is somewhat more contentious because the nπ* excited state is calculated to lie significantly above the $\pi\pi$* excited state in solution. However, transient absorption studies have found that the decay pathway is likely in agreement with uracil and thymine.[10, 13]

Quantum calculations paint a somewhat simpler picture for purines.[14] In both adenine and guanine, a ring-puckering CI returns the excited state to S_0 *via* $\pi\pi^* \rightarrow S_0$. The nπ* excited state lies sufficiently high in energy above S_0 such that it cannot be accessed near 4.7eV and has not been seen to be populated through a CI with $\pi\pi$*. In adenine, a dissociative $\pi\sigma$* state is also postulated to play a role at higher excitation energies, but has yet to be experimentally observed in water.[15, 16]

Although NA constituent photodeactivation mechanisms display many similarities, small structural changes have been shown to greatly impact dynamics. For example, adenine is known to have two tautomers—7H and 9H—at neutral pH which have dramatically different decay lifetimes. The biologically relevant tautomer, 9H, decays with a sub-ps lifetime while the 7H tautomer exhibits a several picosecond lifetime.[17] Clearly, experimental study of NB derivatives is critical to understanding the subtle effects that can impact the excited state dynamics of NA systems.

1.2.3 Open Problems

A detailed map of the photoactivated processes in NA constituents has been the subject of an extensive body of research, yet many outstanding questions remain.[1] In particular, the role of long-lived triplet excited states—which have been implicated as precursors to many photoproducts, including pyrimidine dimers—is somewhat opaque given the low intersystem crossing yields and the ultrafast decay timescale of the singlet excited states. The involvement of higher-lying excited states, including the nπ* excited state in purines and the $\pi\sigma$* state in adenine, are also the subject of debate. Theoretical calculations of the excited states of nucleosides and nucleotides are somewhat limited, and study of extended NAs is yet a young area of research. Finally, the states giving rise to the 200nm absorption band, and their subsequent relaxation mechanism, are ill-studied across NA constituents. This rich variety of complex questions thus requires continued attention in order to construct a holistic understanding of DNA photochemistry and photophysics.

Several time-resolved spectroscopic techniques—including transient absorption, fluorescence upconversion, and photoelectron spectroscopy—have been employed to study NBs. Time-resolved photoelectron spectroscopy is a powerful technique for monitoring radiationless transitions with state specificity. When coupled to a liquid microjet, dynamics of solutes in an aqueous environment can also be explored. This dissertation focuses on the implementation of this technique to shed light on new facets of the dynamics of NA constituents in water. To this end, the remainder of this chapter will focus on providing a foundational understanding of the technique and its application to the study of non-adiabatic dynamics in the condensed phase.

1.3 Principles of Photoelectron Spectroscopy

A photon can eject an electron from a parent molecule provided the photon has more energy than the electron binding energy (eBE). If this is indeed the case, then the bound electron can be projected onto an appropriate unbound continuum state, and any energy in excess of the eBE manifests as electron kinetic energy (eKE). The relationship between the photon energy (hν), eBE, and eKE is then related by Equation 1.1.

$$eBE = h\nu - eKE \tag{1.1}$$

Experimentally, this is realized by intersecting a species of interest with a laser beam and recording the kinetic energy of the nascent photoelectrons—this technique is photoelectron spectroscopy (PES).[8] Ionization selection rules are somewhat relaxed because the outgoing photoelectron can carry the necessary symmetry for any given transition. In principle, any state can be photoionized and, consequently, there are no dark states in PES like there are in other optical spectroscopies. Furthermore, charged particles can be easily steered and focused and detection of electrons is extremely sensitive.

1.3.1 Selection Rules

Electron photodetachment is a vertical process and is therefore governed by the Born-Oppenheimer approximation (BOA).[18, 19] Under this paradigm, electrons of a molecule move much faster than the nucleus. The electronic coordinates are thus parametrized by the nuclear coordinates and the molecular wavefunction is separable. This is shown in Equation 1.2, where Ψ is the total molecular wavefunction and ψ_e and ψ_v correspond to the electronic and vibrational wavefunctions, respectively.

$$|\Psi\rangle = |\psi_e\rangle\, |\psi_v\rangle \tag{1.2}$$

To calculate the optical transition rate from some initial state, Ψ^i, to some final state, Ψ^f, we first define the Hamiltonian with first order perturbation theory.[18] This is shown in Equation 1.3, where ω is the angular frequency of the electromagnetic field.

$$\begin{aligned}\hat{H} &= \hat{H}_0 + \hat{V}(t)\\ &= \hat{H}_0 + \hat{V}_0 sin(\omega t)\end{aligned} \tag{1.3}$$

Invoking the electric dipole approximation allows us to re-express $\hat{V}(t)$ in terms of the polarization vector, $\vec{\epsilon}$, and dipole operator, $\vec{\boldsymbol{\mu}}$, of the perturbing field. This is given by Equation 1.4.

$$\langle \Psi^f | \hat{V}(t) | \Psi^i \rangle \propto \langle \Psi^f | \vec{\epsilon} \cdot \vec{\boldsymbol{\mu}} | \Psi^i \rangle \tag{1.4}$$

Fermi's Golden Rule (FGR) can then be used to approximate the transition rate, $\Gamma_{f\leftarrow i}$.[18] It is described by Equation 1.5, where $\rho(E_f)$ is the density of final states. Note that Ψ^f is part of a near continuum of states in this treatment.

$$\Gamma_{f\leftarrow i} \propto |\, \langle \Psi^f | \vec{\epsilon} \cdot \vec{\boldsymbol{\mu}} | \Psi^i \rangle\, |^2 \rho(E_f) \tag{1.5}$$

Here we can see that $\Gamma_{f \leftarrow i}$ depends on the strength of the coupling between the initial and final wavefunctions through $\vec{\boldsymbol{\mu}}$. Under the BOA, $\vec{\boldsymbol{\mu}}$ is also separable into electronic, $\vec{\boldsymbol{\mu}}_e$, and nuclear, $\vec{\boldsymbol{\mu}}_n$, components. After substituting the separable forms of Ψ (Equation 1.2) and $\vec{\boldsymbol{\mu}}$ into Equation 1.5, $\Gamma_{f \leftarrow i}$ can be simplified as shown in Equation 1.6. Note that $\langle \psi_e^f | \psi_e^i \rangle = \delta_{if}$; $\vec{\boldsymbol{\mu}}$ is of odd parity, so ψ_e^f and ψ_e^i must necessarily have opposite parity to each other.

$$\begin{aligned}\Gamma_{f \leftarrow i} &\propto |\, \langle \psi_e^f \psi_v^f | \vec{\boldsymbol{\mu}}_e + \vec{\boldsymbol{\mu}}_n | \psi_e^i \psi_v^i \rangle \,|^2 |\, \langle \psi_n^f | \psi_n^i \rangle \,|^2 \\ &\propto |\, \langle \psi_e^f | \vec{\boldsymbol{\mu}}_e | \psi_e^i \rangle \langle \psi_v^f | \psi_v^i \rangle + \langle \psi_e^f | \psi_e^i \rangle \langle \psi_v^f | \vec{\boldsymbol{\mu}}_n | \psi_v^i \rangle \,|^2 \\ &\propto |\, \langle \psi_e^f | \vec{\boldsymbol{\mu}}_e | \psi_e^i \rangle \,|^2 |\, \langle \psi_v^f | \psi_v^i \rangle \,|^2\end{aligned} \tag{1.6}$$

Finally, because the photoelectron is ionized from the molecule, $|\psi_e^f\rangle$ can be rewritten in terms of the photoelectron, $|k\rangle$, and bound core electrons, $|\phi_e^f\rangle$. Thus, $\Gamma_{f \leftarrow i}$ can be re-expressed according to Equation 1.7.

$$\Gamma_{f \leftarrow i} \propto |\, \langle k, \phi_e^f | \vec{\boldsymbol{\mu}}_e | \psi_e^i \rangle \,|^2 |\, \langle \psi_v^f | \psi_v^i \rangle \,|^2 \tag{1.7}$$

Hence, we arrive at the selection rules for PES—both terms in Equation 1.7 must be non-zero for a transition to be allowed.[2] The first term contains the electronic symmetry condition; because the photoelectron is ejected from the molecule, it can leave with whatever wavefunction is required to fulfill the condition. The second term is the so-called "Franck-Condon (FC) factor" ($|\, \langle \psi_v^f | \psi_v^i \rangle \,|^2$).[20] Good overlap of the initial and final nuclear wavefunctions is needed to appreciably access a transition; transitions with zero FC overlap are forbidden, even if the detachment photon energy is sufficient.

1.4 Time-Resolved Photoelectron Spectroscopy

The rise in reliable[3] commercial ultrafast lasers has enabled real-time monitoring of molecular dynamics by numerous pump-probe spectroscopies.[21] Dynamics subsequent to electronic excitation involve the coupled flow of energy between electronic and nuclear configurations. In general, PES has the capacity to disentangle these configurations, which—when carried out in a time-resolved manner—greatly aids in understanding deactivation mechanisms.

---

[2] Chapter 1 of M. L. Weichman's dissertation provides an excellent treatment of PES selection rules.

[3] somewhat

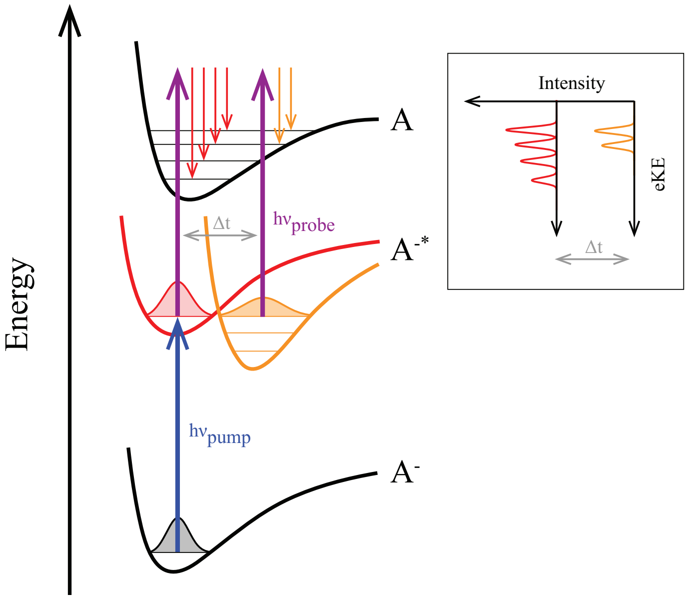

Figure 1.4: Schematic of TRPES, where the relevant potential energy surfaces are shown. The anion ground state is indicated by A^-, the anion excited state is indicated by A^{-*}, and the neutral is indicated by A. The resulting photoelectron spectra at two pump-probe delays are shown in the inset to the right.

In time-resolved photoelectron spectroscopy (TRPES), a pump pulse first prepares the state of interest and a subsequent probe pulse generates photoelectrons by coupling the prepared state to the ionization continuum (*i.e.* photodetachment or photoionization). The time delay between the pump and probe is varied to follow the nascent photoelectron distribution as it evolves. Provided sufficient probe energy, the ensuing wavepacket can, in principle, be tracked directly throughout the entire relaxation process.[8, 22–25] With its femtosecond laser pulse capabilities, our apparatus can readily monitor short-lived excited states, radiationless decay pathways, and vibrational relaxation processes along the ground state surface.

TRPES is schematically shown in Figure 1.4. Spectra are typically plotted in eBE because it is photon-invariant. Feature intensity depends on the absorption and detachment cross-sections. The vertical binding energy (VBE), or the peak of the feature, is fundamental to the spectrum—it corresponds to the transition with maximum FC overlap.

As an introductory exercise to the theoretical treatment of TRPES, consider a simple system comprising three states: the ground state, $|\Psi^i\rangle$, excited state, $|\Psi^m\rangle$, and ionized state, $|\Psi^f\rangle$. This system is defined by Equation 1.8, where k is the sum over all three states. The eigenfunctions of the time-independent Schrödinger equation are given by $|\psi_k\rangle$ and $c_k(t)$ $= \langle\psi_k|\Psi(t)\rangle$.

$$\begin{aligned} |\Psi(t)\rangle &= \sum_k c_k(t)\,|\psi_k\rangle \\ &= \sum_k c_k(0) e^{\dfrac{-iE_k t}{\hbar}}\,|\psi_k\rangle \end{aligned} \tag{1.8}$$

The excited and ionized states are assumed to be populated through single photon processes and the $|\Psi^m\rangle$ to $|\Psi^f\rangle$ transition is considered irreversible. The coefficient $c_f(t)$ can then be calculated using second-order time-dependent perturbation theory.[18] Assuming that $t_0 = 0$, we can write $c_f(t)$ according to the interaction representation, as shown in Equation 1.9. Note that the notation ω_{ab} is shorthand for $\omega_a - \omega_b$, where $\omega_a = {}^{E_a}/_{\hbar}$.

$$\begin{aligned} c_f(t) = \delta_{fi} &- \frac{i}{\hbar}\int_0^t dt'\,\langle\Psi^f|\hat{V}(t')|\Psi^i\rangle\, e^{i\omega_{fi}t'} \\ &- \frac{1}{\hbar^2}\int_0^t\int_0^{t'} dt'dt''\,\langle\Psi^f|\hat{V}(t')|\Psi^m\rangle\,\langle\Psi^m|\hat{V}(t'')|\Psi^i\rangle\, e^{i\omega_{fm}t'}e^{i\omega_{mi}t''} \end{aligned} \tag{1.9}$$

Both the first and second terms in Equation 1.9 are zero, leaving only the third term.[4] We can further simplify this expression by applying the BOA and electric dipole approximations. The wavefunctions $|\Psi^n\rangle$ are given by Equation 1.10, and $c_f(t)$ is given by Equation 1.11, where $\hat{H}_{probe}$ is the nuclear Hamiltonian for the detached potential energy surface. Recall $|k\rangle$ is the wavefunction for the photoelectron and $|\phi_e^f\rangle$ is the wavefunction for the core electrons.

$$|\Psi^i\rangle = |\psi_e^i\rangle\,|\psi_v^i\rangle \qquad |\Psi^m\rangle = |\psi_e^m\rangle\,|\psi_v^m\rangle \qquad |\Psi^f\rangle = |k\rangle\,|\phi_e^f\rangle\,|\psi_v^f\rangle \tag{1.10}$$

$$\begin{aligned} c_f(t) \propto \int_0^t\int_0^{t'} dt'dt''\,&\langle k,\phi_e^f|\vec{\boldsymbol{\mu}}_e\cdot\vec{\epsilon}_{probe}(t')|\psi_e^m\rangle\,\langle\psi_e^m|\vec{\boldsymbol{\mu}}_e\cdot\vec{\epsilon}_{pump}(t'')|\psi_e^i\rangle \\ &\times e^{-i(\omega_f t' - \omega_i t'')/\hbar}\,\langle\psi_v^f|e^{i\hat{H}_{probe}(t' - t'')/\hbar}|\psi_v^m\rangle \end{aligned} \tag{1.11}$$

Calculation of the photoelectron spectrum, $S(\Delta t)$, at some pump-probe delay Δt is straightforward, as $S(\Delta t) \propto |c_f(t)|^2$. Notably, this depends on time-evolving FC factors.

---

[4] The second cancels because the pump photon is assumed to be insufficiently energetic to detach the photoelectron from $|\Psi^i\rangle$.

1.5 Non-Adiabatic Molecular Dynamics

The BOA breaks down when the nuclear and electronic motions of a molecule couple.[5] Dynamics resulting from this behavior are called "non-adiabatic" and many ultrafast relaxation processes, including those important to photochemistry, involve strong and rapid non-adiabatic couplings.[24] This section will focus in particular on "internal conversion"—a radiationless transition between two different electronic states. Prerequisite to internal conversion are an initial electronic state and equivalently energetic vibrational levels of a lower lying electronic state which can effectively couple.[6] These vibrational levels are generally a dense manifold in polyatomic molecules.

The coupling between an initial electronic state, $|\psi_e^i\rangle$, and final electronic state, $|\psi_e^f\rangle$, is accounted for by the non-adiabatic coupling operator contained in the electronic Hamiltonian. It is a vector differential operator, and depends on the derivative coupling vector, $\boldsymbol{F}_{f\leftarrow i}$, described by Equation 1.12 for $i \neq f$.

$$\begin{aligned}\boldsymbol{F}_{f\leftarrow i} &= \langle \psi_e^f | \boldsymbol{\nabla} \psi_e^i \rangle \\ &= \frac{\langle \psi_e^f | \boldsymbol{\nabla} \hat{H}_e | \psi_e^i \rangle}{E_i - E_f}\end{aligned} \tag{1.12}$$

We see that the non-adiabatic coupling depends inversely on the energy difference between the two adiabatic states. This is the so-called "energy gap law"—the coupling between two states is stronger the smaller the energy gap between them.[26, 27]

1.5.1 Conical Intersections

The unique case in which the potential energy surfaces of the adiabatic states $|\Psi^f\rangle$ and $|\Psi^i\rangle$ are degenerate is called a "conical intersection" (CI).[27–29] This occurs in the strong coupling limit, where the coupling is infinite. CIs provide a path for rapid electronic relaxation on a femtosecond timescale[7] and are nearly ubiquitous in polyatomic systems. Computational methods to simulate the dynamics of polyatomic molecules are often ill-equipped to

---

[5] This is often called "vibronic" coupling.

[6] IC occurs in states with the same spin, if the states have different spin this process is called an intersystem crossing.

[7] Hence the slang "photochemical funnel."

perform fully quantum mechanical calculations, particularly for systems in the condensed phase. Direct study of the potential energy surfaces through femtosecond pump-probe techniques is thus invaluable to the study of non-adiabatic processes.

To better understand the existence of CIs, consider a two-state system given by Equation 1.13 and the corresponding Hamiltonian, where $H_{nm} = \langle \phi_m | \hat{H} | \phi_n \rangle$, given by Equation 1.14.[18, 19] The wavefunctions for each adiabatic state, Ψ_n, are assumed to be a linear combination of diabatic states ϕ_n with coefficients c_{nm}.

$$\begin{bmatrix} \Psi_1 \\ \Psi_2 \end{bmatrix} = \begin{bmatrix} c_{11} & c_{12} \\ c_{21} & c_{22} \end{bmatrix} \begin{bmatrix} \phi_1 \\ \phi_2 \end{bmatrix} \tag{1.13}$$

$$\hat{H} = \begin{bmatrix} H_{11} & H_{12} \\ H_{21} & H_{22} \end{bmatrix} \tag{1.14}$$

The eigenvalues for this problem are shown in Equation 1.15.

$$E_{1,2} = \frac{H_{11} + H_{22}}{2} \pm \sqrt{\frac{(H_{11} - H_{22})^2}{4} + H_{12}^2} \tag{1.15}$$

Because the adiabatic states must be degenerate, $E_1 = E_2$. Thus we arrive at the conditions for a CI, given by Equations 1.16 and 1.17.

$$H_{11} - H_{22} = 0 \tag{1.16}$$

$$H_{12} = H_{21} = 0 \tag{1.17}$$

These conditions can be satisfied in an $N - 2$ dimensional subspace, where N is the number of degrees of freedom. Notably, CIs are not single points, but rather an $N - 2$ dimensional seam.[8]

1.6 Dynamics in the Condensed Phase

The unique properties of water and their effects on chemical dynamics cannot be understated.[30] Solvation can dramatically affect potential energy surfaces, so much so that the

---

[8] When the potential energy surfaces are plotted in two dimensions, they form a cone at the intersection.

course of a chemical reaction can be changed. Photoisomerization, proton and electron transfer, and excess energy dissipation are all enabled by strong coupling between water and solute molecules.

Solvation can be described simply if water is treated as a structureless dielectric continuum.[31–33] The so-called "Born model" for the free energy of solvation of a single, monatomic ion treats the change in energy between gas and solution phases as a change in the energy content of the environment surrounding the solute.

We begin by recalling that the molar Gibbs free energy can be generally expressed by Equation 1.18, where N is the number of components, n_i is moles, and μ_i is the chemical potential.

$$G = \sum_{i=1}^{N} n_i \cdot \mu_i \tag{1.18}$$

The electrostatic potential energy of an ion of radius R and charge q in a medium with a dielectric constant ϵ can be expressed by Equation 1.19.

$$\begin{aligned} \mu_i(\epsilon) &= \frac{\partial U}{\partial N_i} \\ &= \frac{1}{2}\frac{q^2}{4\pi\epsilon R} \end{aligned} \tag{1.19}$$

Substituting Equation 1.19 in for μ_i, ΔG_{solv} is then the difference in energy between the vacuum and solution. This is given by Equation 1.20, where N_A is Avogadro's number. The dielectric constant in vacuum is given by ϵ_0; the relative dielectric constant is then given by $\epsilon_r = {}^{\epsilon}/_{\epsilon_0}$.

$$\begin{aligned} \Delta G_{solv} &= N_A[\mu(\epsilon) - \mu(\epsilon_0)] \\ &= \frac{1}{2}\frac{N_A q^2}{4\pi\epsilon_0 R}\Big(\frac{1}{\epsilon_r} - 1\Big) \end{aligned} \tag{1.20}$$

This can be used to determine the energetic and entropic cost of solvation.[9] Notably, this treatment considers solvation as an equilibrium effect. With the advent of ultrafast laser

---

[9] Recall, $\Delta G = \Delta H - T\Delta S$, where ΔH is the heat of the process, and ΔS the entropy.

spectroscopies, the dynamics of solvation can be interrogated in real time. Considering water as a dielectric continuum is typically not appropriate for computational studies of chemical dynamics in the condensed phase. The low mass of hydrogen gives rise to nuclear quantum effects, such as nuclear tunneling and zero-point energy. Cooperative hydrogen bonding in liquid water further complicates accurate accounting of solvation effects.[34]

1.6.1 Vibrational Cooling and Solvation Dynamics

When a solute undergoes a vertical transition, such as one in TRPES, the orientation of the local solvent molecules immediately after the excitation is still in the thermalized configuration for the initial state. The solvent molecules will subsequently reorient to adapt their configuration to the excited state in a series of steps. An initial sub-picosecond "inertial response" involves rotations and subsequent librations of the first solvent shell. This is followed by collective motions which are diffusive in nature and happen on pico- to nanosecond timescales.[35, 36]

This behavior has a number of effects on the photoelectron spectra. First, vibrational and rotational detail are typically smeared out by the high density of solvent shell configurations sampled. Second, the eBE of a species is often increased in solution if solvation is favorable. Finally, solvation shifts with lifetimes of ∼1ps are common in water. These are characterized by spectral shifts to tighter binding energies and spectral narrowing as the equilibrium configuration is approached. An illustrative example of typical solvation dynamics seen in TRPES photoelectron spectra is shown in Figure 1.5.

Large polyatomic molecules in the gas phase can provide their own heat bath—energy in a high-lying vibrational mode is redistributed to lower lying modes without changing the total energy of the molecule. This is called intramolecular vibrational energy redistribution. In the condensed phase, the solvent can expedite vibrational relaxation of the solute through both solvent-assisted intramolecular vibrational energy redistribution[10] and intermolecular vibrational relaxation. This discussion will focus on the latter.

Energy from a solute can be irreversibly transfered to the surrounding solvent by coupling of the solute and solvent modes—this is intermolecular vibrational relaxation.[38, 39] This typically takes place on a picosecond timescale and is sometimes referred to as "vibrational cooling". Strictly speaking, vibrational cooling refers only to intermolecular processes; intramolecular processes are generally assumed to be fully complete before cooling.

Intermolecular vibrational relaxation can be described by a simple collision model, similar

---

[10] Whereby the solute-solvent modes couple.

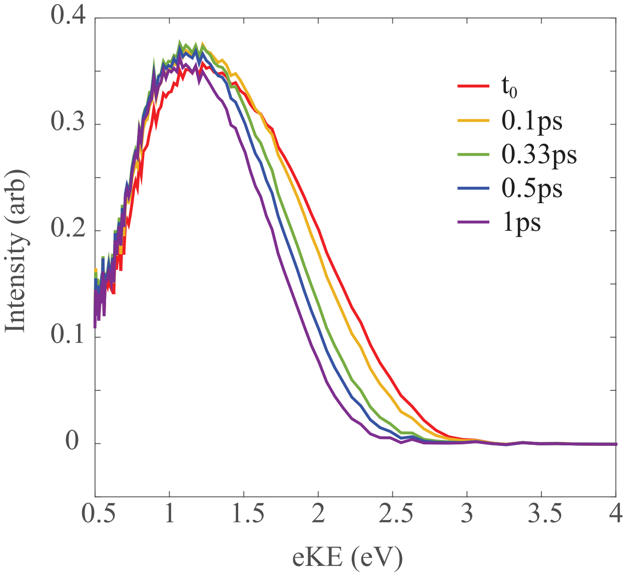

Figure 1.5: Photoelectron spectra of e^-_{aq} generated *via* charge-transfer-to-solvent from KI in water. At early times, spectra are broad and electrons are less tightly bound; as pump-probe delay increases, the spectra are seen to shift to tighter binding energies and narrow in width as the solvent undergoes reorganization. See Reference [37] for more details.

to the one used in the gas phase.[31] Notably, however, the collisional relaxation rate in solution is not bimolecular, as in the gas phase, but unimolecular. This is a consequence of the high molecule density in the condensed phase. The collision relaxation rate law can then be defined by Equation 1.21, where $[C^*]$ is concentration of vibrationally excited solute molecules, and k is the unimolecular rate coefficient.[11]

$$\frac{d[C^*]}{dt} = -k[C^*] \tag{1.21}$$

Fermi's Golden Rule can be used to approximate the vibrational relaxation rate if the solute is assumed to be a diatomic harmonic oscillator and the solvent is treated as a bath of harmonic oscillators. The system must also be constrained to obey energy conservation. The Hamiltonian can then be expressed by Equation 1.22, where $\hat{H}_B$ is the Hamiltonian for a harmonic bath, $\hat{H}_D$ for the diatomic harmonic oscillator solute, and $\hat{V}$ is the operator that describes solute-bath coupling.

$$\hat{H} = \hat{H}_B + \hat{H}_D + \hat{V} \tag{1.22}$$

---

[11] Recall, $k = {}^1\!/\tau$ where τ is the relaxation time.

We will now consider the transition between states $|i\rangle$ and $|f\rangle$ of the diatomic solute, which are eigenstates of $\hat{H}_D$. The initial and final eigenstates of the bath Hamiltonian are given by $|\alpha\rangle$ and $|\alpha'\rangle$, respectively. The FGR expression for the transition, $\Gamma_{f\leftarrow i}$, is then given by Equation 1.23, where the thermal distribution of states in the manifold have been averaged over and all final states have been summed. The bath partition function is given by Q, $\beta = {}^{1}\!/_{k_BT}$ where k_B is Boltzmann's constant and T is temperature, and the density of states is given by the sum of $\delta(E_i + \epsilon_\alpha - E_f - \epsilon_{\alpha'})$.

$$\Gamma_{f\leftarrow i} \propto \sum_{\alpha} \frac{e^{-\beta(E_i+\epsilon_\alpha)}}{Q_\alpha} \sum_{\alpha'} |\langle\alpha', f|\hat{V}|i,\alpha\rangle|^2 \delta(E_i + \epsilon_\alpha - E_f - \epsilon_{\alpha'}) \tag{1.23}$$

This can then be rewritten in time correlation form to give Equation 1.24.

$$\begin{aligned}\Gamma_{f\leftarrow i} &\propto \sum_{\alpha} \frac{e^{-\beta(E_i+\epsilon_\alpha)}}{Q_\alpha} \sum_{\alpha'} \langle\alpha|\hat{V}_{if}|\alpha'\rangle \langle\alpha'|\hat{V}_{fi}|\alpha\rangle \int_{-\infty}^{+\infty} dt e^{it(E_i + \epsilon_\alpha - E_f - \epsilon_{\alpha'})/\hbar} \\ &\propto \int_{-\infty}^{+\infty} dt e^{it(E_i - E_f)/\hbar} \langle\hat{V}_{if}(t)\hat{V}_{fi}(0)\rangle_T\end{aligned} \tag{1.24}$$

As we learned previously, the key parameters that govern the rate of energy transfer are the coupling strength between the solute-bath modes and the energy gap between initial and final states.

1.7 Summary of Systems Studied and Outlook

Chapter 3 of this dissertation focuses on a recently finished study of the excited state deactivation dynamics of the DNA components adenosine (Ado) and adenosine monophosphate (AMP). Femtosecond TRPES in a water microjet was used with photon energies ranging from 4.69-6.20eV. Two absorption bands were studied; the lowest-lying $\pi\pi^*$ excited state was populated by 4.69-4.97eV photons while 6.20eV photons were proposed to excite a higher-lying $\pi\pi^*$ transition.

The $\pi\pi^*$ excited state was found to decay on a timescale ranging from ~210-270fs in Ado and ~240-290fs in AMP. These lifetimes were assigned to the internal conversion of the S_1 $\pi\pi^*$ excited state to vibrationally hot ground state, S_0, and were found to inversely depend on the photoexcitation energy. Photoexcitation at 6.20eV produced a transient signal bound by ~4eV in both Ado and AMP. A lifetime was only recoverable in AMP and found to be

~300fs. Spectral analysis suggests that a high-lying $\pi\pi^*$ excited state is initially populated and subsequently relaxes to the S_1 $\pi\pi^*$ excited state before internal conversion to hot S_0.

Notably, the probe photon energies used in these experiments were insufficient to photodetach electrons from the ground state—bound by ~7.5eV—and observe dynamics along this surface. This belies a common short-coming of TRPES studies that employ conventional femtosecond table-top lasers: photons in excess of 6.2eV are unavailable with solid-state frequency-mixing techniques.

Chapter 4 addresses this concern by introducing a technique known as "high-harmonic generation," which up-converts the output of a commercial femtosecond laser into the extreme ultraviolet to soft X-ray regime. Efforts are currently underway to experimentally realize this on the liquid microjet project, and these plans are described in detail in Chapter 5. We hope to open new frontiers in the investigation of chemical dynamics in the condensed phase with this new setup.

1.8 References

1. *Photoinduced phenomena in nucleic acids I: Nucleobases in the gas phase and in solvents* (eds Barbatti, M., Borin, A. C. & Ullrich, S.) (Springer International Publishing, Cham, 2015).
2. Cadet, J., Mouret, S., Ravanat, J.-L. & Douki, T. Photoinduced damage to cellular DNA: Direct and photosensitized reactions. *Photochem. Photobiol.* **88,** 1048 (2012).
3. Alizadeh, E. & Sanche, L. Precursors of solvated electrons in radiobiological physics and chemistry. *Chem. Rev.* **112,** 5578 (2012).
4. Crespo-Hernández, C. E., Cohen, B., Hare, P. M. & Kohler, B. Ultrafast excited-state dynamics in nucleic acids. *Chem. Rev.* **104,** 1977 (2004).
5. Middleton, C. T. *et al.* DNA excited-state dynamics: From single bases to the double helix. *Annu. Rev. Phys. Chem.* **60,** 217 (2009).
6. Improta, R., Santoro, F. & Blancafort, L. Quantum mechanical studies on the photophysics and the photochemistry of nucleic acids and nucleobases. *Chem. Rev.* **116,** 3540 (2016).
7. Shukla, M. K. & Leszczynski, J. Electronic spectra, excited state structures and interactions of nucleic acid bases and base assemblies: A review. *J. Biomol. Struct. Dyn.* **25,** 93 (2007).
8. Neumark, D. M. Time-resolved photoelectron spectroscopy of molecules and clusters. *Annu. Rev. Phys. Chem.* **52,** 255 (2001).

9. Voet, D., Gratzer, W. B., Cox, R. A. & Doty, P. Absorption spectra of nucleotides, polynucleotides, and nucleic acids in the far ultraviolet. *Biopolymers* **1,** 193 (1963).
10. Hare, P. M., Crespo-Hernández, C. E. & Kohler, B. Internal conversion to the electronic ground state occurs via two distinct pathways for pyrimidine bases in aqueous solution. *Proc. Natl. Acad. Sci. U.S.A.* **104,** 435 (2007).
11. Gustavsson, T. *et al.* Singlet excited-state behavior of uracil and thymine in aqueous solution: A combined experimental and computational study of 11 uracil derivatives. *J. Am. Chem. Soc.* **128,** 607 (2006).
12. Buchner, F., Nakayama, A., Yamazaki, S., Ritze, H.-H. & Lübcke, A. Excited-state relaxation of hydrated thymine and thymidine measured by liquid-jet photoelectron spectroscopy: Experiment and simulation. *J. Am. Chem. Soc.* **137,** 2931 (2015).
13. Sharonov, A., Gustavsson, T., Carré, V., Renault, E. & Markovitsi, D. Cytosine excited state dynamics studied by femtosecond fluorescence upconversion and transient absorption spectroscopy. *Chem. Phys. Lett.* **380,** 173 (2003).
14. Improta, R., Santoro, F. & Blancafort, L. Quantum mechanical studies on the photophysics and the photochemistry of nucleic acids and nucleobases. *Chem. Rev.* **116,** 3540 (2016).
15. Roberts, G. M., Marroux, H. J. B., Grubb, M. P., Ashfold, M. N. R. & Orr-Ewing, A. J. On the participation of photoinduced N-H bond fission in aqueous adenine at 266 and 220nm: A combined ultrafast transient electronic and vibrational absorption spectroscopy study. *J. Phys. Chem. A* **118,** 11211 (2014).
16. Perun, S., Sobolewski, A. L. & Domcke, W. Photostability of 9H-adenine: Mechanisms of the radiationless deactivation of the lowest excited singlet states. *Chem. Phys.* **313,** 107 (2005).
17. Cohen, B., Hare, P. M. & Kohler, B. Ultrafast excited-state dynamics of adenine and monomethylated adenines in solution: Implications for the nonradiative decay mechanism. *J. Am. Chem. Soc.* **125,** 13594 (2003).
18. Schatz, G. C. & Ratner, M. A. *Quantum mechanics in chemistry* (Dover Publications, Inc., 2002).
19. Voorhis, T. V. *5.73 Introductory Quantum Mechanics I* <`https://ocw.mit.edu`> (Massachusetts Institute of Technology: MIT OpenCourseWare, Fall 2005).
20. Tokmakoff, A. *5.74 Introductory Quantum Mechanics II* <`https://ocw.mit.edu`> (Massachusetts Institute of Technology: MIT OpenCourseWare, Spring 2009).
21. Pedersen, S. & Zewail, A. H. Femtosecond real time probing of reactions XXII. Kinetic description of probe absorption, fluorescence, depletion and mass spectrometry. *Mol. Phys.* **89,** 1455 (1996).
22. Stolow, A. Femtosecond time-resolved photoelectron spectroscopy of polyatomic molecules. *Annu. Rev. Phys. Chem.* **54,** 89 (2003).

23. Stolow, A., Bragg, A. E. & Neumark, D. M. Femtosecond time-resolved photoelectron spectroscopy. *Chem. Rev.* **104,** 1719 (2004).

24. Stolow, A. & Underwood, J. G. *Time-resolved photoelectron spectroscopy of nonadiabatic dynamics in polyatomic molecules* 497 (John Wiley & Sons, Inc., 2008).

25. Suzuki, T. Time-resolved photoelectron spectroscopy of non-adiabatic electronic dynamics in gas and liquid phases. *Int. Rev. Phys. Chem.* **31,** 265 (2012).

26. Englman, R. & Jortner, J. The energy gap law for radiationless transitions in large molecules. *Mol. Phys.* **18,** 145 (1970).

27. Worth, G. A. & Cederbaum, L. S. Beyond Born-Oppenheimer: Molecular dynamics through a conical intersection. *Annu. Rev. Phys. Chem.* **55,** 127 (2004).

28. Matsika, S. & Krause, P. Nonadiabatic events and conical intersections. *Annu. Rev. Phys. Chem.* **62,** 621 (2011).

29. Domcke, W. & Yarkony, D. R. Role of conical intersections in molecular spectroscopy and photoinduced chemical dynamics. *Annu. Rev. Phys. Chem.* **63,** 325 (2012).

30. Chandler, D. *Introduction to modern statistical mechanics* (Oxford University Press, 1987).

31. Nitzan, A. *Chemical dynamics in the condensed phases: Relaxation, transfer, and reactions in condensed molecular systems* (Oxford University Press, Oxford, New York, 2006).

32. Levine, R. D. *Molecular reaction dynamics* (Cambridge University Press, 2005).

33. Atkins, P. W. & MacDermott, A. J. The Born equation and ionic solvation. *J. Chem. Ed.* **59,** 359 (1982).

34. Bakker, H. J. & Skinner, J. L. Vibrational spectroscopy as a probe of structure and dynamics in liquid water. *Chem. Rev.* **110,** 1498 (2010).

35. Aherne, D., Tran, V. & Schwartz, B. J. Nonlinear, nonpolar solvation dynamics in water: The roles of electrostriction and solvent translation in the breakdown of linear response. *J. Phys. Chem. B* **104,** 5382 (2000).

36. Rosspeintner, A., Lang, B. & Vauthey, E. Ultrafast photochemistry in liquids. *Annu. Rev. Phys. Chem.* **64,** 247 (2013).

37. Elkins, M. H., Williams, H. L. & Neumark, D. M. Dynamics of electron solvation in methanol: Excited state relaxation and generation by charge-transfer-to-solvent. *J. Chem. Phys.* **142,** 234501 (2015).

38. Elles, C. G. & Crim, F. F. Connecting chemical dynamics in gases and liquids. *Annu. Rev. Phys. Chem.* **57,** 273 (2006).

39. Owrutsky, J. C., Raftery, D. & Hochstrasser, R. M. Vibrational relaxation dynamics in solutions. *Annu. Rev. Phys. Chem.* **45,** 519 (1994).

Chapter 2

Experimental Methods

2.1 Overview

The current experimental setup comprises a commercial ultrafast laser, liquid microjet, and photoelectron spectrometer. Data analysis is performed in MATLAB with home-brewed code. The design of a new XUV source is described in Section III and will be implemented in short order by Blake A. Erickson.

2.2 Liquid Microjet Technique

Photoelectron spectroscopy necessitates that experiments be performed in vacuum; inelastic scattering events alter the observed kinetic energies of the photoejected electrons. Practically speaking, this means that the mean free path—the average distance traveled by a particle between collisions—of the electron must be greater than the electron flight length. Mean free path, λ, is described below by Equation 2.1, where σ is the molecular collision cross-section, ρ is the number density of the vapor, k_B is the Boltzmann constant, T is the temperature, P is the vapor pressure, and c is the ratio of the particle and gas velocities.[1][1–4]

$$\begin{aligned} \lambda &= \frac{1}{c\sigma\rho} \\ &= \frac{k_B T}{c\sigma P} \end{aligned} \tag{2.1}$$

---

[1] This ratio is difficult to calculate, but typically ranges from ∼0.75-1.5.

Liquids with high vapor pressures have been historically difficult to study because the equilibrium vapor density renders λ prohibitively short. In water, σ is generally $\sim$30Å^2, and $\lambda \approx 10\mu m$ in water at its equilibrium vapor pressure at 277K. We employ a cylindrical liquid microjet to overcome this obstacle.

First described by Manfred Faubel and coworkers, the microjet enables the introduction of high vapor pressure liquids into vacuum.[5, 6] Microjets are thin, fast-flowing liquid jets that satisfy the Knudsen condition, which is to say the diameter of the jet is the same as or smaller than λ in equilibrium vapor. Under this paradigm, evaporation is effectively collision-free. Thus, the gas density at the surface of the liquid jet is greatly reduced, and λ of electrons photoejected from the jet is increased. A skimmer can also be used to cut into the vapor jacket around the liquid core, further reducing the number of collisions an outgoing particle might undergo in the vapor. For example, a 5μm diameter water microjet (at 252K) skimmed 1mm away from the surface will have $\lambda = 250\mu m$.[4] The low vapor density also reduces the gas load such that a modest turbomolecular pump may be used to evacuate the sample chamber into the sub-mTorr regime. Moreover, the microjet affords a sample which is continually renewed, impervious to laser burn, and has a high target density.

2.2.1 Microjet Design and Implementation

Our microjet design mirrors that of the Saykally group[7] at UC Berkeley and is described in detail in the dissertation of Alexander T. Shreve.[8] The microjet principally comprises an inline sub-micron filter, a Swagelok union, and a jet aperture (see Figure 2.2a). The aperture is constructed by securing a fused-silica capillary in a jacket of polyether ether ketone (PEEK) tubing with a Swagelok ferrule. PEEK tubing is resistant to corrosion by a variety of chemicals. A diamond wheel cutter is used to evenly score the capillary to ensure straight flow of the microjet. This design affords a laminar flow regime of several millimeters and a turbulent flow regime of several centimeters.

The diameter of these microjets can range from 5-100μm; our lab uses 20μm ID capillaries. Empirically, we have found that a constant flow rate of 0.2-0.3mL/min and backing pressure of 80atm produces the most stable water microjets. The temperature of the microjet can be calculated through an evaporative cooling model,[9] and is found to be $\sim$280K at the laser interaction region, 1mm down from the exit of the capillary.[2] Because DNA components are expensive, we have begun the practice of recycling solutions. Recycled solution was analyzed and found not to differ significantly in concentration from fresh solution. Used solutions are sub-micron filtered before reuse and can be recycled in this way $\sim$3 times before the solute

---

[2] The code for this model is written in Igor Pro and maintained by the Saykally group. It is also described in the dissertation of Alexander T. Shreve.

concentration drops appreciably.

Conveniently, alignment of the laser beams onto the microjet is made obvious by a Fraunhofer diffraction pattern that is present when the laser and microjet are spatially overlapped. The microjet acts as a single slit for most wavelengths currently used (200-800nm). Average laser powers must be kept under 200μW; beyond this limit space charge effects result in plasma generation.[10, 11]

The original Faubel microjets (Microliquids, GmbH) are formed from pulled capillaries. Because the Saykally design loads pressure onto a smaller surface area than the Faubel microjets, a higher backing pressure is used for a comparable flow rate. However, these microjets are more inexpensive to implement and we have found no considerable difference in stability.

Our pump is a 500mL capacity syringe pump (Teledyne Isco, Model 500D), but a peristaltic pump would work equally well and could afford easy switching between solvents. The syringe pump valve manufacturer was changed to Vindum Engineering (MV-210-HC) in 2016 at the suggestion of Royce K. Lam.[3] Vindum valves have been found to be more robust and, as of the time of this writing, only one valve has needed to be serviced. Finally, solutions of DNA components, which have modest water solubilities, were found to clog the microjet assembly somewhat more frequently. This was remedied by flushing the syringe pump and PEEK tubing with a 1M solution of HCl as needed.

2.2.2 Probe Depth Considerations

Of considerable interest to the liquid-phase community is determining whether or not spectral interrogation of the microjet occurs at the surface or in the liquid core for a given experiment.[11, 12] In condensed-phase matter, the emission intensity of electrons attenuates exponentially as a function of depth from the surface at which they were born. To understand the type of solvation environment that surrounds the solute of interest, it is helpful to know the effective electron attenuation length—the shortest distance between two points through which the electron intensity is reduced by $^1/_e$—as a function of eKE.[13] Most condensed phase materials qualitatively obey the same curve, the so-called "universal curve" as shown in Figure 2.1.

The universal curve does show some material dependence, and there is still some outstanding debate regarding the exact shape of the curve for liquid water.[13–15] However, it is generally accepted that the minimum attenuation length is on the order of 10Å, or four

---

[3] A Saykally group doctoral student (Ph.D. Fall 2017).

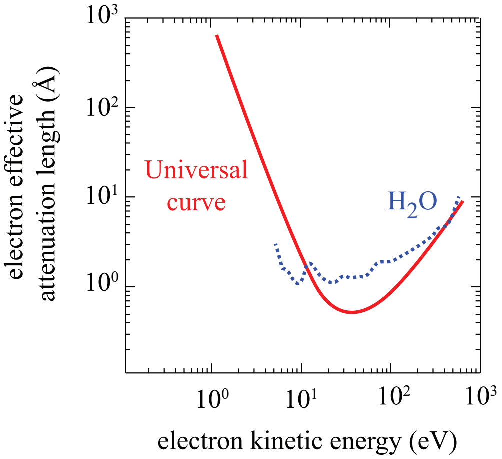

Figure 2.1: The universal curve (solid red line) and measured electron effective attenuation length measured for liquid water (blue dashed line). Adapted from References [13] and [14].

water monolayers, at 50-100eV electron kinetic energy.

Recently, the implementation of so-called "flat jets" has garnered much attention.[3, 16] These can be generated by orthogonally crossing two traditional cylindrical jets to form a flat liquid sheet.[4] A flat jet generated from two 10μm cylindrical jets is approximately 750μm x 500μm x 1μm. The shorter path length through flat jets as compared to cylindrical jets is one key advantage to this design. Additionally, higher pulse energies can be used on the jet without introducing space charge or multiphoton effects, and the larger surface area of flat jets may be more compatible with the diameter of the focused laser beam.

2.3 Photoelectron Spectrometer

The photoelectron spectrometer comprises two main regions, as shown in Figure 2.2: 1) the microjet trap and 2) the detector chamber. Our current apparatus was designed by Alexander T. Shreve, and an extensive discussion of the apparatus can be found in his dissertation.[8] Changes made to the Shreve design are discussed in the dissertation of Madeline H. Elkins.[17]

Briefly, the sample of interest is injected into vacuum *via* a liquid microjet, which is then crossed by femtosecond pump and probe laser pulses and subsequently cryotrapped. Photoejected electrons are sampled through a skimmer, steered down the time-of-flight (ToF)

---

[4] Assemblies can be purchased from Microliquids, GmbH.

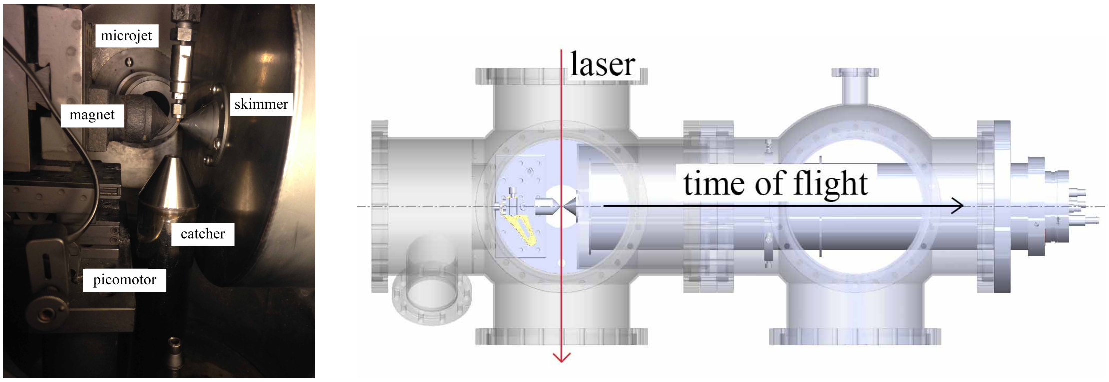

(a) Microjet

(b) Trap and detector chambers

Figure 2.2: Photoelectron spectrometer: (a) Microjet assembly in vacuum with optional catcher installed, (b) Top view of trap and detector chambers with laser and time of flight axes indicated. The microjet axis is into the plane of the page.

tube by a magnetic bottle, and collected by a microchannel plate chevron stack with a phosphor screen. This is pictured in Figure 2.2b and detailed below.

2.3.1 Microjet Trap

The assembled microjet is introduced into vacuum by a three-axis micrometer holster on formed bellows. This allows the microjet to be readily positioned inside of the chamber. When acquiring data, the microjet is centered 1mm from the skimmer orifice, and the capillary tip is moved above the orifice. Laser pulses are orthogonally crossed with the jet in front of the skimmer. A 900μm diameter skimmer is currently used to cut into the vapor jacket and limit the travel of photoelectrons through the vapor. Skimmer diameters of 300-500μm have also been used successfully.

The rare earth magnet component of the magnetic bottle is also located in this chamber, and is described fully in Section 2.3.2.1. For bottle alignment purposes, the magnet is mounted on a three-axis translation setup which can be moved *in vacuo* by picomotor piezo linear actuators (Newport, 8302).

A $150^{L}/_{s}$ turbomolecular pump (Leybold, Turbovac 151) is used to evacuate the chamber. This is backed by a rotary vane mechanical pump (Edwards, E2M8). The jet is cryotrapped with liquid nitrogen at the bottom of the chamber to assist the pumps, and a 7L dewar located in a secondary chamber (a four-way 10” ConFlat (CF) cross mounted to the left of the trap chamber in Figure 2.2, but not shown) is used to further enable a quick pump-down. Typical operating pressures are on the order of $\sim 10^{-4}$Torr.

Many researchers in the liquid microjet community utilize a “catcher” to cryotrap the microjet as soon as possible. This helps to lower the chamber pressure and prevents ice nucleation, which results in frozen microjets. A new catcher has been designed and will likely be installed in tandem with the new XUV source (see Appendix C for drawings). The microjet trap chamber, with optional catcher, is shown in Figure 2.2a.

2.3.1.1 Laser Power and Microjets

Excessively high laser power incident on the microjet can cause a number of undesirable effects: namely, space-charge, ponderomotive, and AC stark shift effects.[10, 11] Average powers, per beam, in excess of 200μW are to be avoided.

- Electron-electron repulsion results in a space charge effect which homogeneously broadens the photoelectron spectral features. This effect is often seen at the onset of the multiphoton laser power regime (peak laser intensity of $\sim 10^{10} W/cm^2$).
- A ponderomotive force by the laser pulse on the photoelectrons will often occur when entering the tunnel ionization laser power regime (peak laser intensity of $> 10^{14} W/cm^2$). Here, observed VBEs are typically offset.
- When the incident laser power exceeds ∼10mW, an AC Stark effect has been seen. This induces an instantaneous energy shift which can either increase or totally close resonant multiphoton transitions to certain ionization channels. For this reason, when calibrating the instrument and calculating streaming potentials, as described below, the incident power is kept below 5mW.

Laser-driven plasma formation is also possible in the tunnel ionization laser power regime (*aka* the strong field regime). This interaction results in the accumulation of quasi-free electrons in the microjet at the focus of the laser. For peak laser intensities above $\sim 10^{17} W/cm^2$ collective electron motions can be resonantly excited by the laser field; generated plasma oscillates in resonance with the laser frequency.

2.3.2 Detector Chamber

The detector chamber comprises a solenoid and microchannel plate detector with a phosphor screen, described in the sections below. It is designed such that the solenoid is not under vacuum so it can be easily removed and serviced if necessary, and to prevent a virtual leak. A gate valve cannot be added to isolate the chamber because the solenoid must abut the back of the skimmer for the magnetic bottle to operate properly; thus, the detector chamber is not under vacuum when the trap chamber is vented.[5]

Operating pressures in this region are $\sim 10^{-6}$Torr. The chamber is pumped by three turbomolecular pumps with a total pumping speed of $1400 ^{L}/_{s}$ (Leybold, Turbovac 150, 151, and 1000C), backed by a rotary vane mechanical pump (Edwards, E2M12).

2.3.2.1 Magnetic Bottle Spectrometer

A magnetic bottle is used in the spectrometer because it greatly increases the collection efficiency of photoelectrons—theoretically to 2π steradians.[18, 19] Without this bottle, the low signal levels would require greatly increasing the number of shots taken at each delay, rendering the required data acquisition period for time-resolved experiments prohibitively long. The magnetic bottle utilizes an inhomogeneous magnetic field and the Lorentz force, described by Equation 2.2, where $\vec{F}$ is the Lorentz force, q is the charge of the photoelectron, $\vec{v}$ is the photoelectron velocity, and $\vec{B}$ is the magnetic field.

$$\begin{aligned} \vec{F} &= q\vec{v} \times \vec{B} \\ &= qvBsin\theta \end{aligned} \tag{2.2}$$

As shown in Figure 2.3, a strong, diverging magnetic field first causes photoelectrons emitted with velocity components off-axis to the desired flight path to spiral axially around the field lines. These helically traveling photoelectrons then encounter a weak, homogeneous magnetic field, with field lines parallel to the ToF axis, and are guided along the flight path for collection. As the photoelectrons travel in this region, their spiral trajectories unravel and become collinear to the ToF axis. Assuming the total velocity is conserved, the cyclotron energy of the photoelectrons is converted into axial energy. The 3D cloud of photoelectrons emitted from the microjet is thus bent so that the trajectories of the photoelectrons are nearly parallel to the ToF axis.

Additionally, the photoelectron distribution is spatially magnified according to Equation 2.3, where M is the magnification factor, B_i is the magnitude of the initial magnetic field, and B_f is the the magnitude of the final magnetic field. Clearly, larger initial fields and smaller final fields result in greater magnification.

---

[5] We have not found this to significantly accelerate MCP degradation.

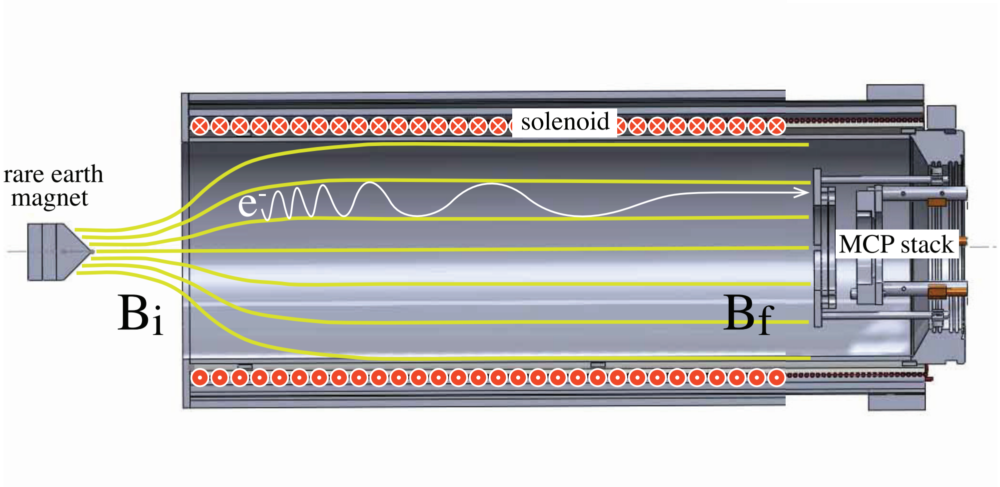

Figure 2.3: Schematic of the magnetic bottle assembly. Magnetic field lines are shown in bright green, and photoelectron trajectories are indicated in white.

$$M = \sqrt{\frac{B_i}{B_f}} \tag{2.3}$$

To experimentally realize the magnetic bottle, we employ rare-earth permanent magnets and a solenoid.[18] A stack of Nickel-coated, high-pull Samarium-cobalt (McMaster-Carr, 57325K93) and Neodymium (McMaster-Carr, 58605K85) disk magnets provide the strong initial magnetic field.[6] A magnetically soft iron cone (Ed Fagan Inc., Hiperco 50A) sits on the end of this stack to shape the magnetic field lines. Initial magnetic fields typically range from 5,000-10,000G in magnetic bottles[7]; our initial field strength is ∼10,000G. The solenoid is 26" long, and is made of 14 gauge copper wire coiled at ten turns per inch. The total length of copper wire used is 4200". From Ampere's Law, the field within a solenoid is defined according to Equation 2.4, where B is the magnitude of the magnetic field, μ/μ_0 is the relative magnetic permeability[8], n is the number of turns per unit length, and I the current applied to the wire.

$$B = \frac{\mu}{\mu_0} nI \tag{2.4}$$

---

[6] Notably, the permanent magnets, as with everything in the trap chamber, are subject to considerable corrosion despite their Nickel-based anti-corrosion casings. Bead-blasting only exacerbates this issue. However, even when pitted and corroded, the magnetic bottle operation was found to be largely unaffected.

[7] Measured as surface field strength.

[8] For copper, μ/μ_0 is 0.999994.

At the time of this writing, 2A of current is applied to the solenoid by a Kepco high current power supply[9], resulting in a final field of ∼15G.[10]

Finally, the rare earth magnet assembly sits in a holster which is also magnetically soft. This holster is attached to a 3-axis linear translation stage which is moved with picomotor piezo motor actuators (Newport, 8302) *in vacuo*. This allows the bottle to be properly aligned, as shown in Figure 2.5.

2.3.2.2 Microchannel Plate Detector and Phosphor Screen

A microchannel plate (MCP) is an electron multiplier consisting of a highly resistive material punctured by an array of channels coated to act as continuous electron multipliers.[20, 21] When certain particles strike the interior of a channel, secondary electrons are released; repeated strikes cause an electron cascade for every incident particle. A bias voltage is applied across the plate to accelerate the electrons from the front to the back of the plate.

When the electron cascade becomes sufficiently large, residual gas trapped in the plates can also become ionized. Positive ions produced by this process are then accelerated back to the front of the plate and during this transit they can strike the channel walls to produce secondary electrons that create an "after pulse". This ion feedback effect is suppressed by implementing a pair of MCPs each with short, slightly angled channels that are oriented orthogonally to the channels of the other MCP. This forms a chevron pattern, and the MCP configuration is named thusly. Most MCPs, including ours (Photonis, Imaging Quality Long-Life MCP 25/12/10/12 I 40:1 TC),[11,12] are used in pairs configured in a chevron stack.

The MCP assembly is shown in Figure 2.4. This detection scheme achieves a total gain of $\sim 10^8$ per photoelectron incident on the assembly. A grounded fine mesh grid sits in front of the detector assembly to terminate stray fields. The front and back MCPs are in electrical connection, and receive a bias voltage of ∼2.15kV.[13] A 2200pF bypass capacitor dampens any AC components from the high voltage power supply (Bertan, Model 205B-05R) and a 50kΩ resistor dampens ringing. After passing through the MCPs, the electron cascade is

---

[9] If the leads of the bottle are swapped, the photoelectrons will be defocused from the center and form a donut-shaped distribution.

[10] To create a simple degausser for the detector chamber, hook the leads of the bottle into a Variac to apply AC. Beware: stainless steel is notoriously difficult to degauss!

[11] We have found no operational difference between matched and un-matched sets.

[12] The original MCPs and phosphor screen were purchased from Beam Imaging Solutions, BOS-25-OPT01.

[13] This draws $\sim 50\mu$A of current from the power supply.

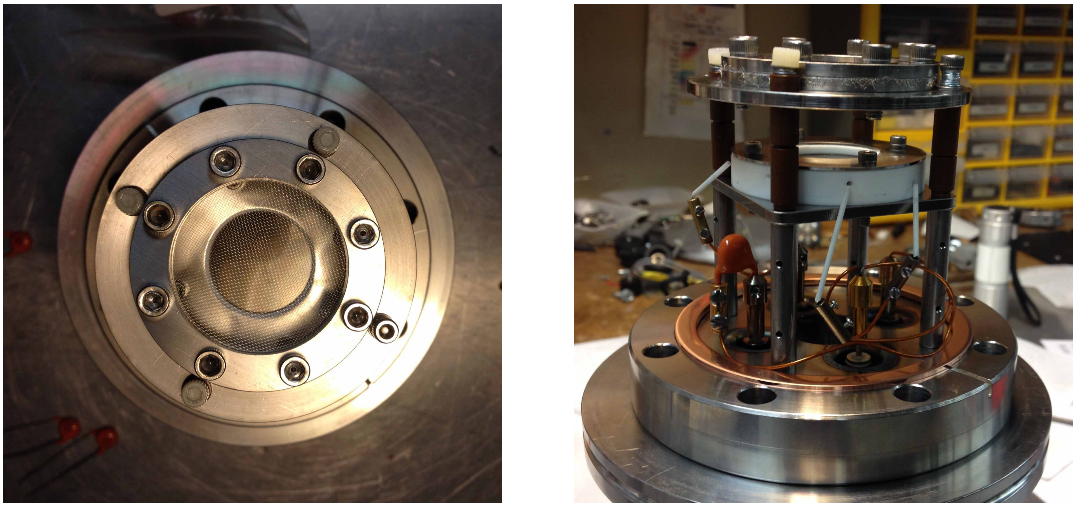

(a) Top view (b) Side view

Figure 2.4: The MCP assembly: (a) A fine mesh grid is grounded and placed in front of the MCPs to terminate stray field lines, (b) The MCP chevron and phosphor screen are housed in a white Teflon puck and wired to BNC-type pinouts on a 2-3/4” Conflat flange.

accelerated to a phosphor screen, which receives ~3.25kV.[14] The impinging cascade causes the phosphor to emit photons which are imaged by a charge-coupled device (a camera) for the sole purpose of aligning the magnetic bottle. Figure 2.5 shows the phosphor screen for a good magnetic bottle alignment—the photoelectron cloud should be round and tightly focused. Signal is capacitively coupled off of the back MCP by a 1000pF capacitor.[15] To mitigate impedance mismatch, each of the MCPs and the phosphor are connected to 1MΩ resistors.[16] The voltage in the circuit is regulated by a 50V Zener diode. The detector circuit diagram can be found in the dissertations of Shreve and Elkins.[8, 17]

Microchannel plates are so sensitive that, even in the absence of photoelectrons, stray ions or high-energy photons can cause an electron cascade. These “dark counts” originate from several sources, including thermionic emission from ion gauges and cosmic radiation. Typical dark count intensities in our apparatus are quite low, ~5-10mV.[17] Often, ringing is present in the dark count signal and is principally due to cross-talk between the layers of

---

[14] This draws 0μA.

[15] Signal could also be coupled off of the phosphor—we have found no considerable difference as compared to coupling off of the back MCP.

[16] These typically are the first to overheat and mushroom in the circuit.

[17] To measure dark counts, the signal off of the high-voltage applied MCP is measured on the oscilloscope in the absence of light and photoelectrons. The signal is self-triggered at ~1mV.

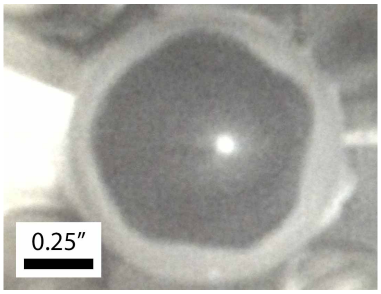

Figure 2.5: The phosphor image when the magnetic bottle is well-aligned.

the detector.[18] The period of the ringing from the MCPs is ∼8ns—this corresponds to an energy spread (between the peaks in the ringing signal) that is much smaller than typical bandwidth of solution-phase spectra, and is thus not accounted for in analysis of TRPES data.

2.4 Data Acquisition

The capacitively coupled signal from the MCPs is sent to an oscilloscope (Textronix, DPO 3034), which acts in part as a digital-to-analog converter. The oscilloscope is triggered by a TTL pulse sent from the Astrella system synchronization and delay generator. The pulse is delayed such that the laser spike is 16ns before the oscilloscope trigger.[19] Data is recorded by the oscilloscope for 2000ns after the trigger in 2ns bins. This is then averaged over 512 shots, and the averaged waveform is sent to the data acquisition computer to be written to file by the data acquisition software.

The LabVIEW data acquisition software was largely written by Alexander T. Shreve, but has since been modified to accommodate automated background scans.[8] It is described briefly herein; a fuller discussion of the main body of the code can be found in Appendix C of the Shreve dissertation; updates to the code can be found in Appendix B.1 of this dissertation. Currently, 1,024 shots are taken at each sequential delay, followed by 1,024 shots of each background. The laser pulses produce a static, two-photon, one-color signal, and these are collected at a pump-probe delay of zero. When this sequence is completed, the motorized stage is instructed to loop back to the first delay and start the process over again until the specified number of shots per stage delay are acquired. The delays and shots

---

[18] The characteristic period of electronic ring is on the order of tens of nanoseconds. If the source of the ring is due to signal reflection or impedance mismatch in the BNC cables, this can be confirmed by changing the cable length.

[19] This is for historical reasons and is largely arbitrary.

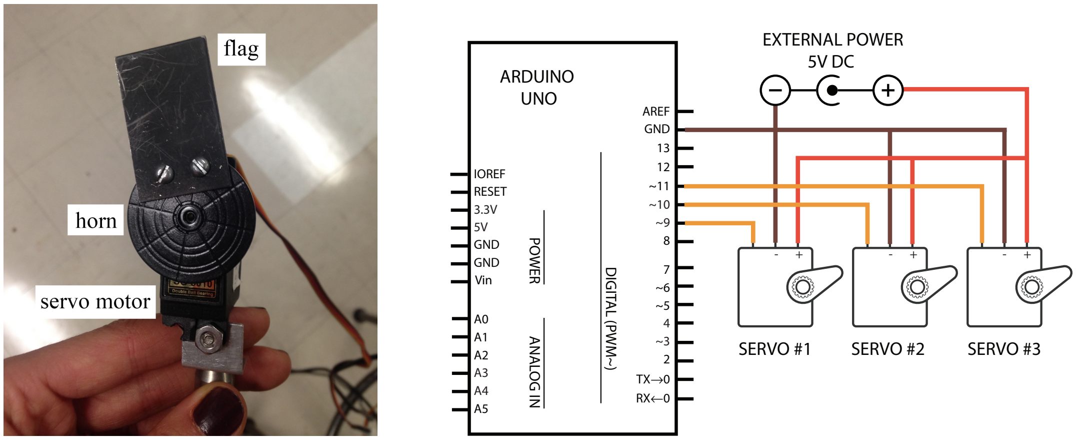

(a) Beam block (b) Circuit diagram

Figure 2.6: Arduino-controlled servo motors for automated background scans: (a) Each beam block comprises an aluminum flag mounted to the horn of a servo which is in turn mounted to an optical post, (b) The circuit diagram for the Arduino UNO and servo motors; digital pins 9, 10, and 11 are used to communicate with the servos, and the UNO and servos are powered by a standard 5V plug.

to be acquired are specified in the configuration table CSV file, which is called by the data acquisition software. As data packets are sent to the computer, they are 1) appended to the appropriate delay-specific CSV file and 2) summed along with the previous waveforms to generate a new total intensity for that delay. These combined sums are saved in a new CSV file—this is the useful output of the program.

The background scans have been automated through implementation of servo motors (AdaFruit Industries, TowerPro SG-5010) and an Arduino UNO microcontroller. Black aluminum flags were mounted to each servo horn to block the individual laser beams. Simple ASCII characters sent to the UNO control the flag positions, making integration into the existing acquisition software straightforward. The Arduino UNO code can be found in Appendix B.2, along with a brief explanatory text. The circuit diagram and a picture of the device are presented in Figures 2.6a and 2.6b.

2.4.1 Post-Processing

Before fitting TRPES data, it first undergoes a post-processing procedure in MATLAB. The MATLAB script used for this is described in detail in the Elkins dissertation.[17] The script is summarized by the code flow diagram pictured in Figure 2.7. Briefly, this script converts ToF data into eKE-space, subtracts the one-color, two-photon backgrounds, and accounts for the intentionally low discrimination by correcting the baseline level.

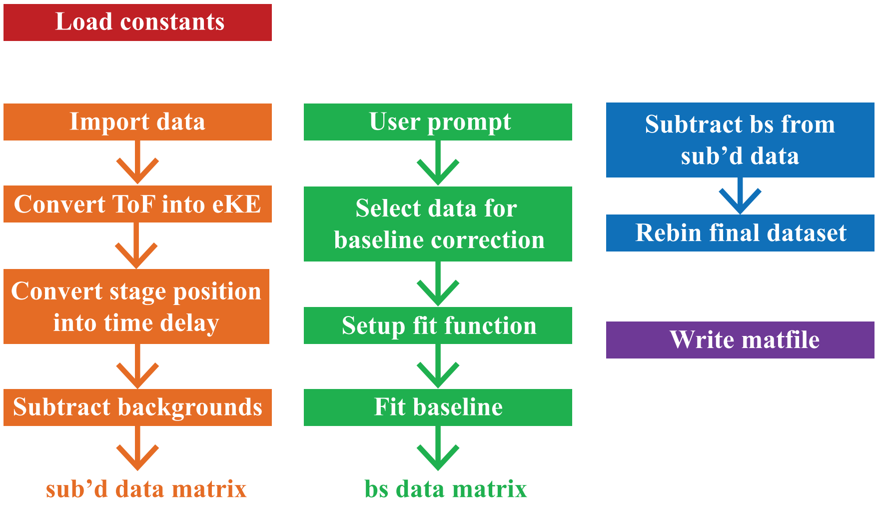

Figure 2.7: Sequence diagram for MATLAB script PostProcessor.m.

2.4.2 Time-of-Flight and Energy Resolution

The conversion between arrival time and eKE of a photoelectron is straightforward if the flight length is known. Electron kinetic energy is defined by Equation 2.5, where m_e is the electron mass, v is the photoelectron velocity, l is the flight length, and t is the time-of-arrival.

$$\begin{aligned} eKE &= \frac{m_e v^2}{2} \\ &= \frac{m_e l^2}{2t^2} \end{aligned} \tag{2.5}$$

Note that the center-of-mass velocity does not need to be accounted for because the flow of the microjet is orders of magnitude slower than the photoelectron flight time.

The conversion between the waveform in ToF and eKE space is a non-linear transformation, and thus the appropriate Jacobian must be invoked. This is given by Equation 2.6, where I_{eKE} is the intensity in eKE space, I_{ToF} is the intensity in time-of-flight space, and eKE is the electron kinetic energy at the point of interest.

$$I_{eKE} = \frac{I_{ToF}}{eKE^{3/2}} \tag{2.6}$$

Taken together, Equations 2.5 and 2.6 reveal several important features of eKE spectra.

First, and perhaps most obviously, eKE goes as t^{-2}, so early time photoelectrons have greater eKE than those that arrive later. Second, because eKE does not scale linearly with arrival time, there is greater point density at lower eKE than at higher eKE, in eKE space, for our detection scheme. Third, we notice that the feature widths in eKE spectra depend on their ToF. If we assume that a Gaussian feature has a FWHM of 2ns, we can see that in energy space, the feature will be sharper at lower eKE than at higher eKE.[20]

Instrumental resolution depends on the flight length and width of time bins on the detector. The energy resolution of a typical femtosecond laser pulse is ~30meV, and thus rarely affects the peak widths observed in our spectra. It is also worth noting that the magnetic bottle will slightly spread the arrival times of photoelectrons. An off-axis photoelectron with equivalent kinetic energy as one fully on axis will arrive slightly later in time if its cyclotron energy is not fully converted into axial energy. However, this has never noticeably affected the data, particularly given that features typically have a full width at half maximum (FWHM) of ~1eV. Finally, data below eKE 0.3eV is not analyzed; photons scattering off of water arrive at early times and generate considerable noise at low eKE because the MCPs are not gated.

2.4.3 Obtaining Accurate Electron Binding Energies

To obtain eBEs, observed ToF data must be calibrated and consistent. This necessitates: 1) regular spectrometer calibration and 2) measurement of the microjet streaming potential. Procedures for these are detailed in the dissertations of Elkins and Shreve, and the principles are described briefly below.[8, 17]

Rather conveniently, xenon can be multiphoton ionized to its cationic $^2P_{3/2}$ and $^2P_{1/2}$ states by readily available UV photons.[21,22] The flight tube length and time zero can be backed out by measuring the ToF of these photoelectrons at several photoionization wavelengths near resonance. These parameters are related by Equation 2.7, where t is the time-of-arrival, q_e is the charge of the electron, m_e is the mass of the electron, n is the number of photons involved in the multiphoton ionization, $h\nu$ is the photon energy, l is the flight length, and t_0 is time zero.

---

[20] Hence, cryo-SEVI.

[21] This is a 3-photon process; Xe has a 12.13eV IP.

[22] Argon, with a 4-photon ionization (15.76eV IP) can also be used.

$$\begin{aligned} t &= \frac{l}{\sqrt{\frac{2q_e}{m_e}(nh\nu - eBE)}} + t_0 \\ &= \frac{l}{\sqrt{\frac{q_e}{m_e}m}}\frac{1}{v} + t_0 \end{aligned} \tag{2.7}$$

When the Xe data is then plotted as t as a function of $1/v$ it can be fit by Equation 2.7. To generate a reconstruction error, the recovered values for l and t_0 are used to back-calculate the eBEs of the Xe $^2P_{3/2}$ and $^2P_{1/2}$ peaks and these are compared to their known values. Reconstruction errors should be on the order of 10meV. The known flight length and time zero[23] can also be compared to the values obtained from the fit as a secondary check. If the calibration is significantly off, the gas load or the laser power may be too high; if these are reasonable, the alignment of the magnetic bottle may be poor.

A charge separation is present at the solution-capillary interface. In conjunction with the flow velocity profile of the solution—which goes to zero at the walls of the capillary—this gives rise to a static microjet streaming potential, ϕ.[6, 22, 23] This must also be measured to report an accurate eKE. Fortunately, ϕ is effectively constant for any given microjet on any given day. To correct for it, we must simply measure ϕ (as described in the Elkins dissertation[17]) and offset the observed eKE by the appropriate amount, as shown by Equation 2.8.[24]

$$eBE = h\nu_{probe} - eKE - \phi \tag{2.8}$$

Typical ϕ are a few hundred meV and can vary in sign.[25] Usually, NaCl (100mM) is added to solutions which do not already contain ions to offset ϕ somewhat.

2.5 Analysis of Time-Resolved Data

Extracting dynamic information from TRPES data is often frustrated by the complexity of condensed phase systems. To this end, we have adopted several fitting routines. M. H. Elkins

---

[23] We obtain t_0 from the time-of-arrival of laser photons which hit the noble gas jet and are scattered to the detector.

[24] Conveniently, a calibration can also be done at the end of a ϕ measurement if necessary.

[25] Although with our recent DNA work, we have seen $|\phi|$ as large as 900meV!

provides a comprehensive discussion of these in her dissertation; however, a brief description is given here.[17]

In systems where features are clearly separated or isolated, lane integration is generally used to analyze time-evolving photoelectron spectra. Here, the total integrated intensity of a single feature is calculated over some narrow energy range at each delay, and the resulting intensity is plotted as a function of delay. This can then be fit by a sum of exponentials convolved with the Gaussian instrument response function (IRF).[26] A convolution is described by Equation 2.9, where $(f * g)(t)$ is the convolution and f and g are the functions which are to be convolved.

$$(f * g)(t) = \int_{-\infty}^{+\infty} dT f(T) g(t-T) = \int_{-\infty}^{+\infty} dT f(t-T) g(T) \tag{2.9}$$

Let us consider an excited state feature which decays with some monoexponential lifetime. An exponential must be multiplied by a Heaviside step function to describe the time-resolved behavior of the feature (see Equation 2.10). This is consequent to the vertical excitation transition, which instantaneously populates the excited state; before the pump pulse is present, it is assumed that the excited state is unpopulated. This population function, *I(t)* is given by Equation 2.10, where I_0 is the initial intensity, t_0 is time zero, τ is the monoexponential lifetime, and θ the Heaviside function.

$$I(t) = I_0 e^{-t/\tau} \theta(t - t_0) \tag{2.10}$$

To arrive at the fitting function, $I(t)$ must be convolved with the Gaussian temporal profile of the IRF. This is given by Equation 2.11, and can ultimately be expressed by Equation 2.12. A complete derivation of $f(t - t_0)$ can be found in the dissertation of G. B. Griffin.[24]

$$f(t - t_0) = \frac{I_0}{\sigma\sqrt{2}} \int_{-\infty}^{+\infty} dT e^{-T/2\sigma^2} I(t - t_0 - T) \tag{2.11}$$

$$f(t - t_0) = \frac{I_0}{2} e^{(\sigma^2/2\tau^2 - t\,-\,t_0/\tau)} \Big[erf\Big(\frac{t - t_0}{\sigma\sqrt{2}} - \frac{\sigma}{\tau\sqrt{2}} \Big) + 1 \Big] \tag{2.12}$$

As previously stated, lane integration is only appropriate for TRPES data containing either a single feature or multiple well-separated features. Great care must be taken to

---

[26] Recall, our experiment is currently limited by the pump-probe cross correlation—this is our IRF.

choose an appropriate energy lane when features have considerable spectral overlap. If the lane of interest is significantly contaminated by other features, the fit will not accurately report the lifetime of the feature represented by the chosen lane. Due to the high number of possible local environmental configurations, features in the condensed phase are quite broad (*i.e.* FWHM of 0.5-1.0eV) and different features often overlap. Consequently, we turn to a second technique that is capable of disentangling highly congested spectra—Global Lifetime Analysis.

2.5.1 Global Lifetime Analysis

Global Lifetime Analysis (GLA) is a nonlinear Levenberg-Marquardt fitting routine.[25–30] It is an iterative procedure which simultaneously fits the spectral and temporal components of TRPES data. Importantly, this algorithm is dependent on several assumptions:

1. Data can be decomposed into two parts, one that depends only on time $s_i(t)$ and another that depends only on energy $s_i(\lambda)$.
2. The energy features are assumed to change only in intensity; they do not change position or lineshape.
3. Kinetics are exponential, and the time-dependence of the data can be described by a sum of exponentials convolved with the IRF.

We begin by writing an expression for TRPES data, given by Equation 2.13, where $S(t, \lambda)$ is the full data set and n is the minimum number of components necessary to accurately describe the data.

$$S(t, \lambda) = \sum_{i=1}^{n} s_i(t) s_i(\lambda) \tag{2.13}$$

The third assumption of GLA allows us to rewrite $S(t, \lambda)$ so that it is defined according to Equation 2.12. The time-dependent component, $s_i(t)$, is now represented as an exponential decay convolved with the IRF (Equation 2.10). Each decay lifetime τ_j has an associated prefactor, DAS_{τ_j}, which depends on energy. This coefficient is the so-called "decay associated spectrum" (DAS). Notably, and despite its name, the DAS is *not* inherently a photoelectron spectrum. Rather, it is the part of the time-resolved photoelectron spectra that changes with the associated τ_j.

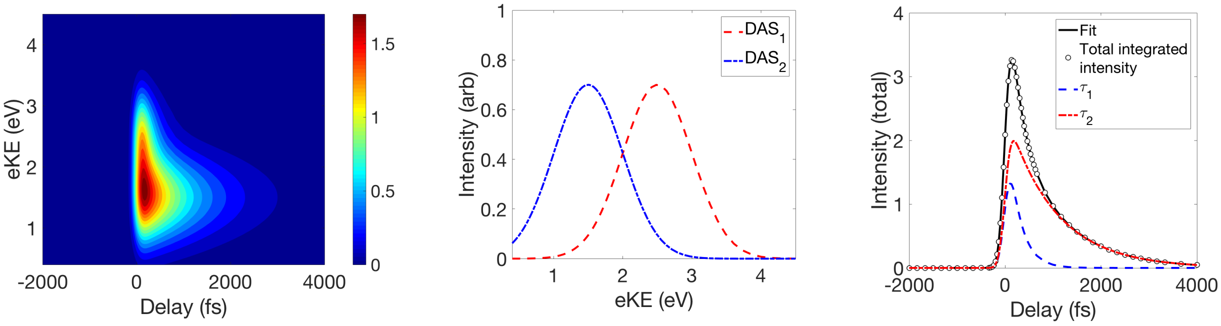

(a) Raw data (b) Decay associated spectra (c) Kinetic components

Figure 2.8: Case 1: (a) Filled contour plot of the two spectral features as they evolve in time, (b) DAS retrieved from GLA clearly show significant overlap, (c) The total integrated intensity plotted alongside each kinetic component.

$$S(t,\lambda) = \sum_{j=1}^{m} DAS_{\tau_j}(\lambda)[e^{-\,t/\tau_j} \cdot IRF] \tag{2.14}$$

To obtain a global fit, an initial guess for τ_j is first made and then the temporal and spectral components of $S(t,\lambda)$ are iterated upon until the algorithm converges. Lifetimes and DAS are the outputs. To better understand the advantages and limitations of GLA, let us consider the following two cases.

Case 1 Consider two features that spectrally overlap, but decay with different mono-exponential lifetimes. These are shown in Figure 2.8. Here, lane integration would prove insufficient to disentangle these features and qualitative assessment of the data cannot determine whether the time-resolved data show a single shifting feature or two separate features. However, if we perform GLA on this dataset, we see that the procedure readily disentangles this congested spectra. GLA gives two DAS and two lifetimes, each corresponding to one spectral feature.

Case 2 Now, let us consider two features which are spectrally-well separated and exchange populations. These are shown in Figure 2.9. If we performed lane integration analysis on this spectrum, we would quickly see that the high eKE feature decays to populate the low eKE feature. On the other hand, GLA will only return one DAS and one lifetime for these two features because they share a lifetime. Remember, DAS are *not* inherently spectra. In this fortuitous case, the low eKE feature persists well beyond the observation window. To accurately fit the data, an additional lifetime can be added to the GLA to account for this (essentially) static feature. Because the DAS for this second lifetime corresponds only to one feature, the spectra of each feature are readily recoverable if a kinetic model is applied

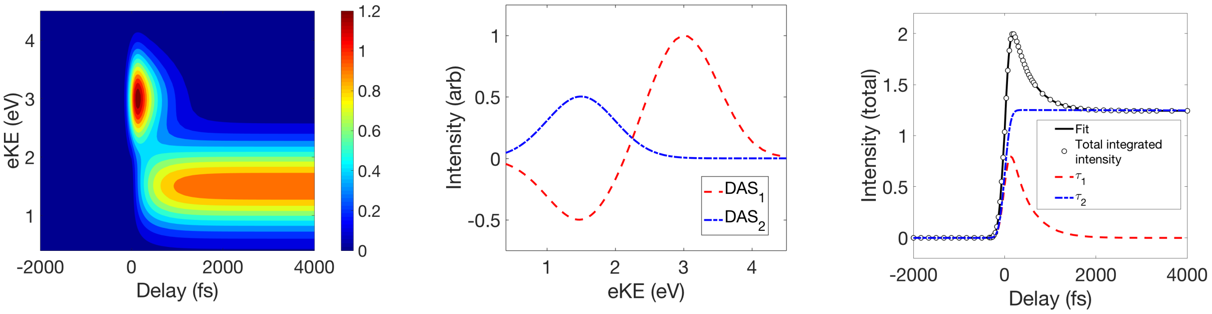

(a) Raw data (b) Decay associated spectra (c) Kinetic components

Figure 2.9: Case 2: (a) Filled contour plot of the two spectral features as they evolve in time; (b) DAS retrieved from GLA; (c) Total integrated intensity plotted alongside each kinetic component. Note that τ_2 is much larger than the observation window and is thus a stand-in for a non-evolving feature.

to the TRPES data.

One critical shortcoming of a GLA-based approach lies in the assumption that spectral features do not evolve. Consequently, GLA is unable to handle solvation shifts, which are ubiquitous to condensed phase dynamics, and characterized by features that narrow and shift to tighter eBE as they evolve. The algorithm typically interprets these shifts as spectrally-overlapping features which exchange, resulting in DAS that look like DAS_1 in Figure 2.9b. M. H. Elkins devised a work-around for this challenge, as described in her dissertation.[17] Additionally, Elkins discusses error analysis for GLA fits.

2.6 New Ultrafast Laser System

All of the ultrafast publications from our lab up until October 2016 resulted from work done using a commercially available titanium sapphire (Ti:Sapph) femtosecond system (Spectra Physics, Tsunami oscillator and Spitfire amplifier). This setup is described in Chapter 2 of the dissertation of Madeline H. Elkins.[17]

To generate higher order harmonics for the new XUV setup, described in Chapter 4, more power and shorter pulses than the extant Spectra Physics system could provide were needed. In October 2016, a new closed one-box Ti:Sapph laser—the Astrella—was purchased from Coherent, Inc. and installed in the laboratory to replace the old system. A brief overview of the setup, and its particular quirks, is detailed below for LPES students. Details concerning the principles and operation of ultrafast lasers can be found in Appendix A of this work and in the Elkins dissertation.[17]

The Astrella gives ~7.1W at 1kHz repetition rate and a pulse duration of 32fs (measured as standard deviation, σ). It comprises the Verdi-G oscillator pump laser, Vitara oscillator, Revolution amplifier pump laser, and amplifier itself. The Vitara suffers $\sim 60\%$ loss in the stretcher and ultimately seeds the amplifier with ~100mW. The amplifier cavity is a so-called "Z-scheme" design and is pumped by ~38W of 527nm light from the Revolution. An afterburner mirror behind the amplifier cavity reflects a small amount of fresh 527nm pump back through the Ti:Sapph crystal to give ~1W additional gain. Two Pockels cells act in concert; the first rotates the polarization of the oscillator seed to trap it in the cavity and the second rotates the polarization of the amplified light to let the pulse out. The Ti:Sapph gain medium is a slab cut at Brewster's angle and cooled with water. Finally, the compressor has an efficiency of $\sim 75\%$.

The output of the Astrella is split between two arms: (1) the quadrupler, which generates 200nm pulses and (2) the 1mJ White-Light TOPAS-Prime with NiRUVis Extension (Light Conversion) which generates tunable UV pulses. Currently, 1W is sent to each arm and the remaining 5W is dumped. Because the pulses are re-compressed before exiting the Astrella, the compression of each arm cannot be independently tuned. Different amounts of chirp—temporal separation in the red and blue edges of a pulse due to their different indices of refraction—are added to each arm because the beam paths are not identical. Consequently, an optimal compression for one arm may not be ideal for the other. Adding chirped mirrors to the quadrupler line could mitigate this issue.

2.6.1 Fourth Harmonic Generation

The fourth harmonic of the Astrella fundamental is generated through a series of sum frequency generation (SFG) processes carried out in β-barium borate (BBO) crystals (THATSHIGH Photoelectric Technology Co., Ltd.; Type 1, 10mm × 10mm clear aperture, p-coating, mounted). SFG is a second order nonlinear optical process, and thus can only occur in noncentrosymmetric materials with very high light intensities, such as those produced by ultrafast pulsed lasers.[31] The optical response of a non-linear material can be described by a power series expansion of the linear polarization. This is given by Equation 2.15, where $\tilde{P}(t)$ is the polarization, ϵ_0 is the permittivity of free space, $\chi^{(n)}$ is the n^{th} order optical susceptibility, and $\tilde{E}(t)$ is the optical field strength.

$$\tilde{P}(t) = \epsilon_0[\chi^{(1)}\tilde{E}(t) + \chi^{(2)}\tilde{E}^2(t) + \chi^{(3)}\tilde{E}^3(t) + ...] \tag{2.15}$$

The above assumes that the material is lossless and dispersionless, and that $\tilde{P}(t)$ and

$\tilde{E}(t)$ are scalar. To describe SFG, we start with Equation 2.16, which describes an optical field with two frequency components, ω_1 and ω_2. The complex conjugate is denoted by "c.c".

$$\tilde{E}(t) = E_1 e^{-i\omega_1 t} + E_2 e^{-i\omega_2 t} + c.c. \tag{2.16}$$

Substituting this in for the second-order term of Equation 2.15, we arrive at the simplified expression given by Equation 2.17.

$$\tilde{P}^{(2)}(t) = \sum_n P(\omega_n) e^{-i\omega_n t} \tag{2.17}$$

The term $P(\omega_1 + \omega_2)$ described SFG, and is enumerated below in Equation 2.18, where ϵ_0 is the permitivitty of free space. In the special case where $\omega_1 = \omega_2$, SFG is preferably called second harmonic generation (SHG).[27]

$$P(\omega_1 + \omega_2) = 2\epsilon_0 \chi^{(2)} E_1 E_2 \tag{2.18}$$

In SFG, ω_1 and ω_2 will interact with the non-linear medium to produce an outgoing field of frequency ω_3, where $\omega_3 = \omega_1 + \omega_2$. Notably, the above treatment ignores the position dependence of the optical field. To achieve wave-mixing, the proper phase relationship must also be maintained between the two input fields. This is the so-called "phase-matching condition", and is described by Equation 2.19, where $\vec{k}_n$ is the wavevector for frequency ω_n.

$$\vec{k}_3 = \vec{k}_1 + \vec{k}_2 \tag{2.19}$$

As stated above, this is practically realized through a series of BBO crystals, arranged as shown in Figure 2.10. Each crystal is 90-200μm thick and type I.[28] Typical efficiencies are $\sim$ 40% for SHG, $\sim$ 20% for third harmonic generation, and $\sim$ 4% for fourth harmonic generation. Thin crystals are used to minimize the extent to which the pulses are stretched in time. Because the mixed frequencies have different indices of refraction through the BBO, thicker crystals tend to introduce chirp. However, the intensity of the generated harmonic increases with the thickness of the crystal.

---

[27] Difference frequency generation (DFG) is described by $P(\omega_1 - \omega_2)$.

[28] Type I and Type II refer to the relative polarizations of the incident beams. For a Type I process, the input beams have the same polarization axis as the crystal (ordinary axis) and the generated output has orthogonal polarization (extraordinary axis).

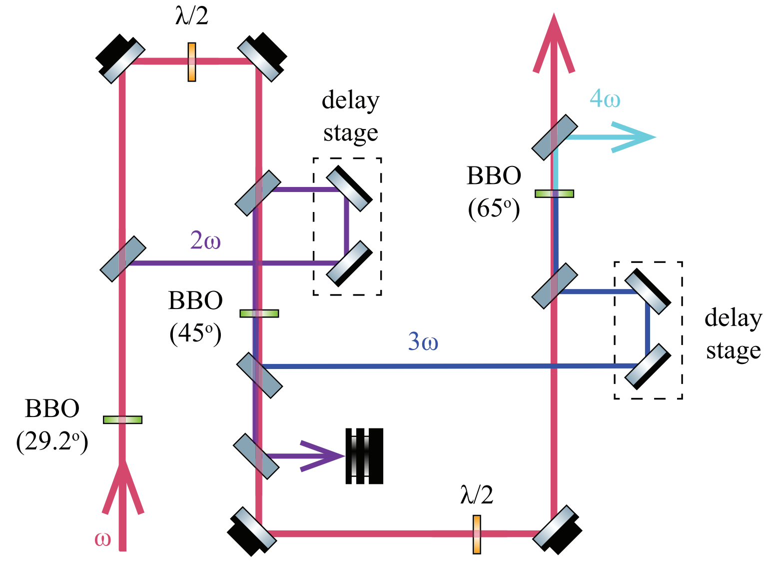

Figure 2.10: Beam path for quadrupler setup. BBO thicknesses range from 90-200μm and the phase matching angles are in parentheses. All optics are dielectric high reflectors, or long wave pass dielectric beamsplitters (BS) with minimum thickness. Half-wave plates ($\lambda/2$) are 90μm thick.

2.6.2 White-Light TOPAS with NiRUVis Extension

The TOPAS-Prime is an optical parametric amplifier (OPA) that is nearly ubiquitous in modern fs-laser systems. Optical parametric amplifiers are non-linear optical devices which utilize the $\chi^{(3)}$ optical susceptibility. Here, a pump photon generates white light continuum (WLC) in a non-linear medium. The pump photon (ω_1) is split into two photons, the signal (ω_2) and idler (ω_3), which obey energy conservation, described by Equation 2.20. Conventionally, the idler is the longest wavelength.

$$\omega_1 = \omega_2 + \omega_3 \tag{2.20}$$

Because any $\omega_2 < \omega_1$ can satisfy Equation 2.20, OPAs are tunable. The TOPAS-Prime can produce wavelengths ranging from ~235nm to ~2600nm through a variety of non-linear mixing processes. It is designed as a two-stage system; the first stage generates the WLC seed and the second amplifies the seed. The components for the various additional mixing processes are housed in the NiRUVis Extension. A portion of the pump is used as a fresh pump for sum-frequency processes for more efficient conversion. Operation has been confined largely to 240-265nm, which affords ~5-7mW of UV measured at the TOPAS-Prime output. Alignment notes can be found in Appendix A.2.2.

2.7 References

1. McQuarrie, D. A. & Simon, J. D. *Physical chemistry: A molecular approach* (University Science Books, 1997).
2. Faubel, M., Schlemmer, S. & Toennies, J. P. A molecular beam study of the evaporation of water from a liquid jet. *Z. Phys. D: At., Mol. Clusters* **10,** 269 (1988).
3. Faust, J. A. & Nathanson, G. M. Microjets and coated wheels: Versatile tools for exploring collisions and reactions at gas-liquid interfaces. *Chem. Soc. Rev.* **45,** 3609 (2016).
4. Wilson, K. R. *et al.* Investigation of volatile liquid surfaces by synchrotron X-ray spectroscopy of liquid microjets. *Rev. Sci. Instrum.* **75,** 725 (2004).
5. Faubel, M., Schlemmer, S. & Toennies, J. P. A molecular beam study of the evaporation of water from a liquid jet. *Z. Phys. D: At., Mol. Clusters* **10,** 269 (1988).
6. Faubel, M., Steiner, B. & Toennies, J. P. Photoelectron spectroscopy of liquid water, some alcohols, and pure nonane in free micro jets. *J. Chem. Phys.* **106,** 9013 (1997).
7. Wilson, K. R. *et al.* Investigation of volatile liquid surfaces by synchrotron x-ray spectroscopy of liquid microjets. *Rev. Sci. Instrum.* **75,** 725 (2004).
8. Shreve, A. T. *Photoelectron spectroscopy of solvated electrons in liquid microjets* PhD dissertation (UC Berkeley, 2012).
9. Smith, J. D., Cappa, C. D., Drisdell, W. S., Cohen, R. C. & Saykally, R. J. Raman thermometry measurements of free evaporation from liquid water droplets. *J. Am. Chem. Soc.* **128,** 12892 (2006).
10. Faubel, M., Siefermann, K. R., Liu, Y. & Abel, B. Ultrafast soft X-ray photoelectron spectroscopy at liquid water microjets. *Acc. Chem. Res.* **45,** 120 (2012).
11. Link, O. *et al.* Ultrafast electronic spectroscopy for chemical analysis near liquid water interfaces: Concepts and applications. *Appl. Phys. A* **96,** 117 (2009).
12. Jungwirth, P. & Tobias, D. J. Ions at the air/water interface. *J. Phys. Chem. B* **106,** 6361 (2002).
13. Ottosson, N., Faubel, M., Bradforth, S. E., Jungwirth, P. & Winter, B. Photoelectron spectroscopy of liquid water and aqueous solution: Electron effective attenuation lengths and emission-angle anisotropy. *J. Electron. Spectrosc. Relat. Phenom.* **177,** 60 (2010).
14. Suzuki, Y.-I., Nishizawa, K., Kurahashi, N. & Suzuki, T. Effective attenuation length of an electron in liquid water between 10 and 600eV. *Phys. Rev. E* **90,** 010302 (2014).
15. Seidel, R., Winter, B. & Bradforth, S. E. Valence electronic structure of aqueous solutions: Insights from photoelectron spectroscopy. *Annu. Rev. Phys. Chem.* **67,** 283 (2016).

16. Bush, J. W. M. & Hasha, A. E. On the collision of laminar jets: Fluid chains and fishbones. *J. Fluid Mech.* **511,** 285 (2004).
17. Elkins, M. H. *Dynamics of electron relaxation studied using time-resolved photoelectron spectroscopy in liquid microjets* PhD dissertation (UC Berkeley, 2015).
18. Kruit, P. & Read, F. H. Magnetic field paralleliser for 2π electron-spectrometer and electron-image magnifier. *J. Phys. E: Sci. Instrum.* **16,** 313 (1983).
19. Rijs, A. M., Backus, E. H. G., de Lange, C. A., Westwood, N. P. C. & Janssen, M. H. M. 'Magnetic bottle' spectrometer as a versatile tool for laser photoelectron spectroscopy. *J. Electron. Spectrosc. Relat. Phenom.* **112,** 151 (2000).
20. Gys, T. Micro-channel plates and vacuum detectors. *Nuclear Inst. and Methods in Physics Research, A* **787,** 254 (2015).
21. Ladislas Wiza, J. Microchannel plate detectors. *Nucl. Instr. Meth. Phys. Res.* **162,** 587 (1979).
22. Faubel, M. & Steiner, B. Strong bipolar electrokinetic charging of thin liquid jets emerging from 10μm PtIr nozzles. *Ber. Bunsenges. Phys. Chem.* **96,** 1167 (1992).
23. Kelly, D. N., Lam, R. K., Duffin, A. M. & Saykally, R. J. Exploring solid/aqueous interfaces with ultradilute electrokinetic analysis of liquid microjets. *J. Phys. Chem. C* **117,** 12702 (2013).
24. Griffin, G. B. *Time resolved photoelectron imaging of electronic relaxation dynamics in anionic clusters* PhD dissertation (UC Berkeley, 2009).
25. Knutson, J. R., Walbridge, D. G. & Brand, L. Decay-associated fluorescence spectra and the heterogeneous emission of alcohol dehydrogenase. *Biochemistry* **21,** 4671 (1982).
26. Van Stokkum, I. H. M., Larsen, D. S. & van Grondelle, R. Global and target analysis of time-resolved spectra. *Biochim. Biophys. Acta* **1657,** 82 (2004).
27. Elkins, M. H., Williams, H. L. & Neumark, D. M. Dynamics of electron solvation in methanol: Excited state relaxation and generation by charge-transfer-to-solvent. *J. Chem. Phys.* **142,** 234501 (2015).
28. Hendler, R. W. & Shrager, R. I. Deconvolutions based on singular value decomposition and the pseudoinverse: A guide for beginners. *J. Biochem. Bioph. Methods* **28,** 1 (1994).
29. Marciniak, H. & Lochbrunner, S. On the interpretation of decay associated spectra in the presence of time dependent spectral shifts. *Chem. Phys. Lett.* **609,** 184 (2014).
30. Shlens, J. A Tutorial on Principal Component Analysis. *CoRR.* arXiv: `1404.1100` (2014).
31. Boyd, R. W. *Nonlinear optics* 3rd ed. (Academic Press, Burlington, 2008).

Part II

Ultrafast Photophysics of DNA Components

Chapter 3

Ultrafast Excited State Relaxation of Adenosine and Adenosine Monophosphate Studied with Time-Resolved Photoelectron Spectroscopy in Liquid Microjets

H. L. Williams, B. A. Erickson, & D. M. Neumark. In preparation.

The excited state relaxation dynamics of adenosine and adenosine monophosphate were studied at multiple excitation energies using femtosecond time-resolved photoelectron spectroscopy in a water microjet. Photoexcitation wavelengths of 4.69-4.97eV and 6.20eV were observed to access the lowest $\pi\pi^*$ excited state, S_1, and a higher-lying excited state of possible $\pi\pi^*$ character, respectively. Electrons were photodetached from S_1 at 6.20eV and from the higher-lying excited state at 4.69-4.97eV. The S_1 $\pi\pi^*$ excited state was found to decay with a lifetime ranging from 220-270fs in adenosine and 240-290fs in adenosine monophosphate. This lifetime depends inversely on the pump photon energy. The higher-lying excited state decayed on a timescale ranging from 290-350fs, and was only measurable in adenosine monophosphate.

3.1 Introduction

DNA and its constituent components are the fundamental building blocks of life and are capable of a rich variety of photoinduced processes.[1, 2] Despite strong absorption bands in the UV regime—known to be genotoxic—DNA is remarkably photostable.[3–7] Consequently,

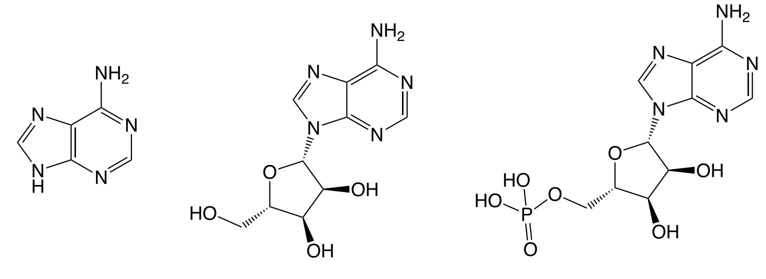

9*H*-Adenine

Adenosine

Adenosine monophosphate

Figure 3.1: Structures of the 9H tautomer of Ade, Ado, and AMP.

there is considerable interest in developing a fundamental, molecular-level understanding of photodeactivation in DNA. In particular, the mechanisms by which excess energy is funneled away from nucleic acid (NA) constituents, and the relationship between these dynamics and the composition of the NA constituent and surrounding environment, is a primary focus of research efforts. One of the most extensively studied DNA components is isolated adenine (Ade).[8, 9] Gas phase studies provide important insights into the fundamental chemistry of Ade, however, study of the isolated Ade nucleoside and nucleotide, adenosine (Ado) and adenosine monophosphate (AMP), respectively, has been hampered by experimental challenges.[10, 11] These systems are of particular interest because even modest structural alterations to nucleobases have been shown to dramatically impact dynamics.[12] Furthermore, it is important to understand the role that the aqueous environment surrounding cellular DNA plays in the spectroscopy and dynamics of NA constituents, as water both significantly alters the potential energy landscape of these molecules and acts as a major radiation dump.[6, 13, 14] Here, we investigate the ultrafast deactivation dynamics of photoexcited Ado and AMP in water microjets at several energies, ranging from 4.69-6.20eV, using time-resolved photoelectron spectroscopy.

Adenine and its derivatives (Figure 3.1) have strong UV absorption bands with maxima at ~260 and ~200nm (4.77 and 6.20eV).[15] These correspond to excitations of the system on the aromatic ring of the nitrogenous base. The electronic structure of isolated Ade has been extensively studied by transient absorption (TA), fluorescence upconversion (FU), time-resolved photoelectron spectroscopy (TRPES) and by theoretical techniques.[12, 13, 16–29] More recent efforts have also interrogated Ade in aqueous solution by employing the same experimental techniques.[6, 12, 16–18, 30–41] It is generally understood that UV light near 4.77eV photoexcites a $\pi\pi^*$ transition; transitions to low lying nπ^* excited states have weak oscillator strengths.[29] Theoretical modeling results for the electronic structure are confounded regarding the energy ordering of the nπ^* and $\pi\pi^*$ excited states because this depends heavily on the chosen ground state geometry in an aqueous environment. It is generally accepted, however, that nπ^* states of Ade and its derivatives are destabilized relative to the $\pi\pi^*$ states in water.[6]

A small fluorescence quantum yield (on the order of 10^{-4}) across DNA components suggests that quenching through non-radiative processes, such as bond dissociation or internal conversion, dominates the photoinduced dynamics.[3, 5] Multiple low-lying excited states in the Franck-Condon (FC) region and competitive relaxation processes render interpretation of photodeactivation mechanisms complex, but Ade and its derivatives are generally found to decay through internal conversion when photoexcited near the absorption band maxima. Recent theoretical work[30–32, 41, 42] on Ade-based NA constituents suggests that non-radiative relaxation occurs from the lowest $\pi\pi^*$ excited states—which can be further subdivided into L_a and L_b states[1]—to the ground state, S_0, *via* a multi-step process. First, any population in the L_b excited state undergoes a sub-100fs internal conversion to L_a. Then, L_a undergoes barrierless internal conversion to vibrationally hot S_0 on a sub-ps timescale. Relaxation to S_0 is remarkably efficient, and is typically attributed to a conical intersection (CI) between L_a and S_0 involving an out-of-plane deformation of the purine ring.[3, 6] The nπ^* excited state is typically not found to contribute significantly to de-excitation[33, 34], although this interpretation has been a matter of some debate.[35, 36] Following a return to S_0, excess vibrational energy is deposited into the surrounding aqueous environment on a picosecond timescale.[34]

The excited state dynamics of Ado and AMP in water have also been experimentally investigated, predominately using ultrafast time-resolved TA[12, 33, 34, 44], FU[17, 18, 37–40], and TRPES[16] techniques. The electronic character of both Ado and AMP has historically been considered to be similar to Ade because the sugar and phosphate moieties do not have absorptions in the UV regime.[3, 5] However, small structural modifications to nucleobases are known to have profound effects.[12, 22] Qualitative agreement of the excited state decay lifetimes suggests that all techniques track the internal conversion of the lowest $\pi\pi^*$ excited state, S_1, to S_0. This process is measured to occur on a timescale of 250-500fs for both Ado and AMP, and is interpreted in the same manner as Ade, explained above. Generally, nucleotides have been found to have longer S_1 lifetimes than those of their corresponding nucleosides, however, Ade derivatives show no such trend.[37] This suggests that the phosphorous moiety may have a limited effect on S_1 for this particular nucleobase series. Furthermore, Pecourt and coworkers[33, 34] observed full recovery of S_0 within picoseconds, precluding the assignment of any component of the relaxation mechanism to long-lived low-lying nπ^* states or possible triplet states.

The dynamics pursuant to excitation of the 200nm (6.20eV) absorption band in the condensed phase remain poorly understood in many DNA constituents, including in the family of Ade-based components. Circular dichroism (CD), magnetic CD, and linear CD studies suggest that two electronic transitions are responsible for the band, and tentatively assign at least one to a high-lying $\pi\pi^*$ excited state.[45–47] This has been corroborated by

---

[1] This labeling convention follows the Platt formalism.[43]

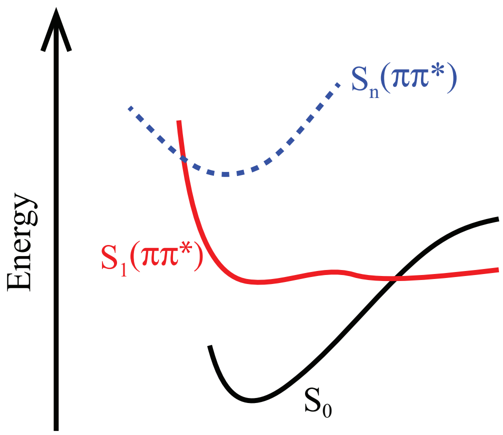

Figure 3.2: Schematic of the potential energy surface of Ade, where possible higher-lying $\pi\pi^*$ excited states are indicated by the blue dashed line. The shape of S_1 is adapted from Reference [6]

recent resonance Raman measurements with time-dependent density functional theory (TD-DFT) calculations,[48] which see different modes activated when Ade is excited at 200nm versus 260nm, indicating that the $\pi\pi^*$ transitions excited by 200nm and 260nm are indeed distinct. Although the existence of $\pi\pi^*$ excited states accessible near 6.20eV have been found with theoretical methods, nπ^* excited states with reasonable oscillator strength have also been found for hydrated Ade in this region.[7, 49, 50] Furthermore, Sobolewski and Domcke[24, 51] have proposed a repulsive $\pi\sigma^*$ state in the 9H Ade tautomer, which can be accessed above 5.5eV. However, it is unclear that this pathway exists in Ado and AMP, as it is attributed to N9 hydrogen abstraction; this hydrogen is replaced with a sugar in both Ado and AMP and presumably the β-glycosidic linkage cannot be as readily ruptured. To our knowledge, no dynamic studies of Ado and AMP in water subsequent to photoexcitation at 6.20eV have been reported until now.

The development of the liquid microjet has enabled the study of high vapor pressure liquids in vacuum.[52–54] Femtosecond time-resolved photoelectron spectroscopy in these microjets has been shown in recent years to be a powerful technique for the interrogation of species in the condensed phase.[14, 55–58] In these types of experiments, the system is electronically excited by a femtosecond pump pulse and the resulting distribution is photodetached by a femtosecond probe pulse at varying pump-probe delays. Provided sufficient probe energy, TRPES can, in theory, track electrons throughout an entire relaxation process and give the binding energies of all states involved. In this way, excited state lifetimes can be directly measured. Recent work by Buchner and coworkers[16] used this approach to measure the excited state lifetimes of Ade and Ado in water at variable pump and probe energies. They observed lifetimes that agreed well with previous TA and FU studies[4, 5], and suggested that above 5.0eV, the probe energy was sufficiently energetic to observe the full relaxation of the excited state.

In this paper, we characterize the ultrafast deactivation of Ado and AMP in aqueous solution subsequent to excitation by UV photons using TRPES in water microjets. This work extends the range of photon energies used to study the excited state relaxation mechanisms of Ade-based DNA components with a pseudo-degenerate pump-probe scheme. At positive pump-probe delays, Ado and AMP are photoexcited at 4.67-4.97eV and photodetached at 6.20eV; this pump-probe scheme is reversed for negative delays. This work marks the first use of a 6.20eV probe for TRPES experiments on NA constituents in order to provide a more complete perspective of the photodeactivation dynamics. Pump energies ranging from 4.69-4.97eV excite the $\pi\pi^*$ state corresponding to the 260nm absorption band, while a 6.20eV pump used to promote electrons into a high-lying excited state corresponding to the 200nm absorption band, which has been previously unexplored by time-resolved experiments (Figure 3.2). Moreover, AMP is investigated by TRPES in water for the first time. We report S_1 lifetimes of 250fs in both Ado and AMP for pump photon energies <5eV, and observe an inverse dependence of the magnitude of the lifetime on the pump photon energy. Excited state dynamics consequent to a 6.20eV pump provide possible evidence for the emergence of a new decay channel involving a higher-lying $\pi\pi^*$ excited state. This is more pronounced in AMP, suggesting that the phosphate moiety may have a nontrivial effect on the electronic structure of higher-lying excited states in NA constituents.

3.2 Methods

Our experimental apparatus has been described in detail previously[57, 58], and is summarized briefly here. To collect PE spectra, a liquid microjet[52–54] was crossed by two femtosecond laser pulses and the resulting photoelectrons were measured via magnetic bottle time-of-flight (ToF).[59] Time-resolved photoelectron spectroscopy experiments were conducted according to the scheme outlined in Equation 3.1, where a variable-energy femtosecond UV pump pulse (4.69-4.97eV), $h\nu_1$, first excited Ado or AMP and a 6.20eV femtosecond probe pulse, $h\nu_2$, then photodetached the nascent electron distribution. The delay between the pump and probe pulses, Δt, was varied to obtain time-resolved data. This scheme applies to positive pump-probe delays only. Because Ado and AMP are strong absorbers of all energies used, this experiment is pseudo-degenerate. For negative delays, the pump-probe scheme is reversed, such that $h\nu_2$ acts as the pump pulse and $h\nu_1$ acts as the probe pulse.

$$A \xrightarrow{h\nu_1} A^* \xrightarrow{\Delta t, h\nu_2} A^{\cdot +} + e^- \tag{3.1}$$

Solutions of Ado (5mM, Sigma Aldrich), and AMP (5mM, Sigma Aldrich) were introduced into vacuum by applying high backing pressure behind a fused silica capillary with a 20μm inner diameter. The flow rate for all experiments was held at 0.25mL/min. All solutions were buffered at pH8 with Trizma HCl (2mM, Sigma Aldrich) and NaCl (100mM, Sigma Aldrich) was added as a counterion to mitigate streaming potentials. These showed no time-resolved photoelectron spectra.

A commercial femtosecond titanium:sapphire laser (Coherent Astrella) generated 1kHz, 35fs pulses centered at 800nm with 7mJ per pulse. Part of this output was then split and directed to a Light Conversion TOPAS-Prime optical parametric amplifier, which generated the tunable-UV pump (4.69-4.97eV), and a BBO-based sum frequency generation system, which generated the fourth harmonic probe (6.20eV). The power of each pulse was maintained between 40-60W, as measured at the liquid microjet chamber. The cross correlation (measured as σ) of the pump and probe was between 160-170fs. This is the experimental instrumental response function (IRF). Note that because the pulses are compressed before splitting into the pump and probe arms, the cross correlations are necessarily wavelength dependent. To obtain time-resolved data, the fourth harmonic was routed onto a motorized stage so the pump and probe pulses could be variably delayed between -2ps and +2ps. Static two-photon, one-color background spectra were taken for the pump and the probe.

Once ejected into vacuum, electrons were sampled through a 900μm skimmer located 1mm away from the jet along the ToF axis. The ToF spectrometer comprises a magnetic bottle and microchannel plate (MCP) chevron stack detector; the magnetic bottle comprises a 1.1T rare earth magnet stack and 10G solenoid. A phosphor screen is coupled to the MCPs, but is used for alignment purposes only. Resulting arrival time distributions were recorded by measuring the capacitively coupled current off the back MCP as a function of time.

Background scans were subtracted from spectra at each delay, and the resulting ToF data were converted to electron kinetic energy (eKE) using the appropriate Jacobian transformation. Spectra and lifetimes were extracted through a Global Lifetime Analysis (GLA) fitting routine using a minimum number of kinetic components.[60, 61] This routine has been described extensively in our previous work.[57] Briefly, GLA can decompose spectrally congested, time-evolving features by simultaneously fitting the entire time-resolved data set. Two assumptions are made. First, the spectral components are assumed to change only in intensity. Each spectral component is then separable into the spectrum of the component, $S_j(eKE)$, which depends only on kinetic energy and the kinetics of the component, $S_i(\Delta t)$, which depends only on pump-probe delay. Second, it is assumed that the kinetics can be expressed as a sum of monoexponentials. To reconstruct a TRPES data set, the spectral components are scaled by their relative photodetachment cross-sections (σ_r) and summed. This is expressed in Equation 3.2 below. Under this paradigm, data can also be represented as a sum of exponentials, convolved with the IRF $L(z - \Delta_t)$ and scaled by a constant which depends on energy—the decay associated spectrum (DAS_{τ_i})—and indexed by the kinetic time constants ($\tau_i = {}^{1}\!/_{k_i}$), as expressed in Equation 3.3. Notably, DAS are not inherently spectra; a kinetic scheme must first be assumed and the σ_r known before a spectrum can be

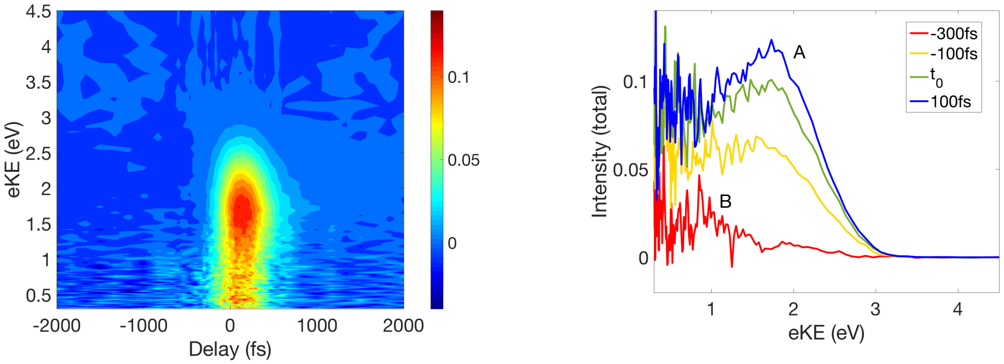

(a) Time-resolved data (b) Spectral lineouts

Figure 3.3: Ado data photoexcited at 4.78eV and photodetached at 6.20eV: (a) filled contour plot of the background-subtracted time resolved photoelectron spectra, (b) spectral lineouts at pump-probe delays of -300, -100, 0, and 100fs. Feature B is found only to contribute to spectra within the IRF at negative delays.

recovered from the DAS.

$$S(eKE, \Delta t) = \sum_{j=1}^{n} \sigma_{r,j} \cdot S_j(eKE) \cdot S_i(\Delta t) \tag{3.2}$$

$$S(eKE, \Delta t) = \sum_{i=1}^{m} DAS_{\tau_i} \cdot \left[e^{-\,z/\tau_i} \cdot L(z - \Delta t) \right] (\Delta t) \tag{3.3}$$

3.3 Results

The background-subtracted time-resolved photoelectron spectra of Ado at 4.78eV pump and 6.20eV probe photon energies and AMP at 4.88eV pump and 6.20eV probe photon energies are presented in Figures 3.3a and 3.4a, respectively. These data are representative of all pump-probe configurations. In both, a single feature is peaked above eKE 1.5eV and spans several eV of eKE. Its intensity decays with increasing positive delay until it is fully depleted within the observation window of 2ps. In AMP, a lower eKE feature is seen to evolve over negative pump-probe delays as well. Spectral lineouts taken at several delays facilitate further inspection of the time-evolving behavior of photoexcited Ado and AMP. These are shown in Figures 3.3b and 3.4b. Here, the pump is always 4.69-4.97eV for positive delays and 6.20eV for negative delays.

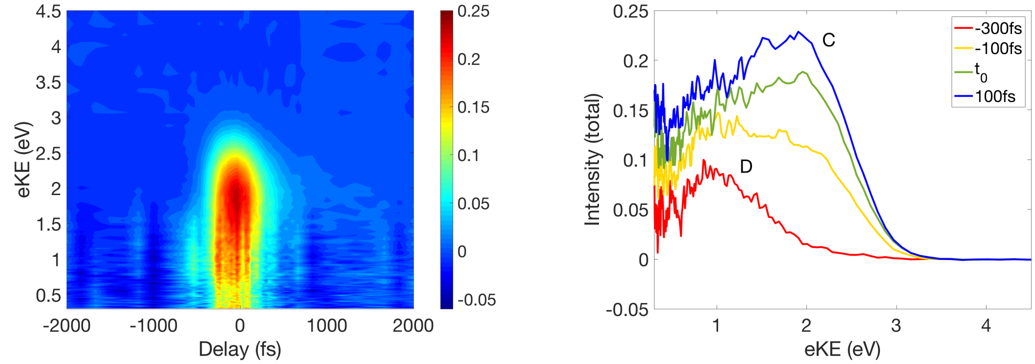

(a) Time-resolved data

(b) Spectral lineouts

Figure 3.4: AMP data photoexcited at 4.88eV and photodetached at 6.20eV for positive pump-probe delays: (a) filled contour plot of the background-subtracted time resolved photoelectron spectra, (b) spectral lineouts at pump-probe delays of -300, -100, 0, and 100fs. Feature B, located eKE 1.4eV, grows in with the IRF and decays over positive delays. Feature C, peaked at eKE 0.6eV, also grows in with the IRF and decays over negative delays. The pump-probe scheme is reversed for negative delays.

Adenosine and AMP lineouts both show two overlapping singly-peaked features, where the feature at higher eKE dominates at positive pump-probe delays, while the feature at lower eKE dominates at negative delays. In Ado, feature A is peaked at eKE ~1.7eV and feature B is peaked at ~0.8eV; in AMP, feature C is peaked at ~1.6eV and feature D is peaked ~0.7eV. Evolution of the spectral shape is not evident for any feature.

The eKE of features A and C are consistent with detachment from the S_1 $\pi\pi^*$ excited state of Ado as observed in previous TRPES studies[16], and we assign these features as such. Assignment of features B and D is somewhat more elusive. In AMP, the 6.20eV photon pulse excites an electronic transition that decays on a measureable timescale. In Ado, however, feature B shows no evolution on the timescale of the experiment, suggesting that whatever state is accessed at 6.20eV relaxes within the IRF. Near time zero, t_0, all features are present and, thus, considerable spectral contamination is likely present across the entire breadth of the spectra. Because of this complexity, we reserve assignment of features B and D until after analysis of the data by GLA, which is the preferred approach for evaluation of congested spectra. In the next section, it will be used to examine the presented time-resolved photoelectron spectra.

3.4 Analysis

Adenosine data were fit using the standard GLA routine described in Section 3.2 with one kinetic component. A minimum of two kinetic components were needed to adequately fit the AMP data by GLA. Figures 3.5a and 3.6a show the total integrated intensity of Ado and AMP, respectively, taken across the entire spectrum at each delay and plotted as a function of delay, with the corresponding GLA kinetic components. Fitted lifetimes for all pump-probe combinations are presented in Tables 3.1 and 3.2. The functional form of an individual kinetic component is a single exponential decay convolved with the Gaussian IRF and a Heaviside function, and is described by Equation 3.4. Normalized DAS for Ado and AMP are presented in Figures 3.5b and 3.6b, respectively. Spectral lineouts at ±300fs are presented alongside the DAS for comparison and are scaled accordingly. These delays were chosen because they lie outside of the Gaussian IRF centered at t_0 and the features in one are thus reasonably uncontaminated by features in the other. Finally, a comparison of DAS_A and DAS_C across pump photon energies of 4.69-4.97 are shown in Figures 3.5c and 3.6c.

$$f(t-t_0) = \frac{I_0}{2} e^{(\sigma^2/2\tau^2 - t \, - \, t_0/\tau)} \Big[erf\Big(\frac{t-t_0}{\sigma\sqrt{2}} - \frac{\sigma}{\tau\sqrt{2}} \Big) + 1 \Big] \tag{3.4}$$

Global lifetime analysis recovers a lifetime of <300fs for the decay of the S_1 $\pi\pi^*$ excited state in Ado and AMP (DAS_A and DAS_C, respectively) for all pump-probe combinations. As the pump photon energy increases, the S_1 lifetime is seen to decrease. This effect is somewhat less pronounced in AMP. Furthermore, the S_1 lifetime in AMP for a given pump photon is slightly longer than in Ado. Spectral evolution reflecting relaxation along the electronic excited state is expected to be seen prior to internal conversion if the decay does indeed correspond to passage of S_1 through the conical intersection into vibrationally hot S_0. Typically, this is evidenced by a photoelectron feature which shifts to lower eKE and narrows as the pump-probe delay increases. As indicated in Section 3.3, evidence for this behavior in the photoelectron spectra at positive delays is sparse. Furthermore, features which shift on a timescale equivalent to or greater than the IRF are expected to be evidenced by a single DAS with positive components at higher eKE and negative components at lower eKE, corresponding to a population exchange between these regions.[57] Clearly, the DAS for features A and C do not show this lineshape and instead overlap well with spectral lineouts taken at positive delays. Thus GLA is considered to accurately report the lifetime of these features.

Notably, however, the DAS peaks are spaced by somewhat less than the difference in pump photon energy (see Tables 3.1 and 3.2), although this difference is challenging to report with a high degree of accuracy given our experimental resolution (~0.1eV). If the measured signal results only from internal conversion, the peak of the DAS would be expected to be

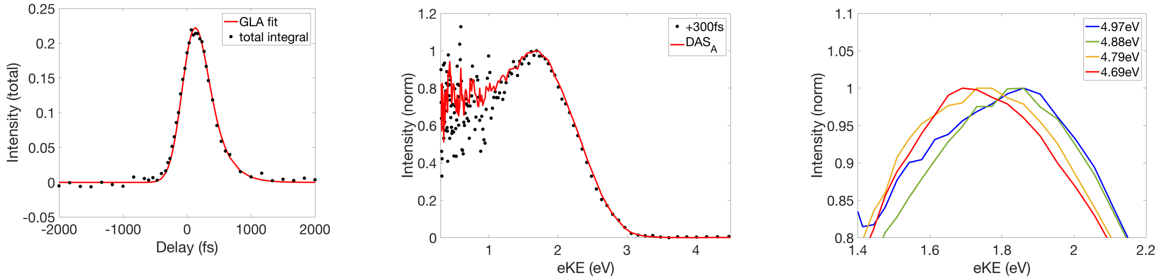

(a) Total integral (b) DAS_A (c) DAS comparison

Figure 3.5: GLA results for Ado photoexcited at 4.78eV and photodetached at 6.20eV: (a) kinetic component and total integrated intensity; (b) normalized DAS_A and spectrum at +300fs; (c) comparison of normalized DAS_A recovered for all pump photon energies.

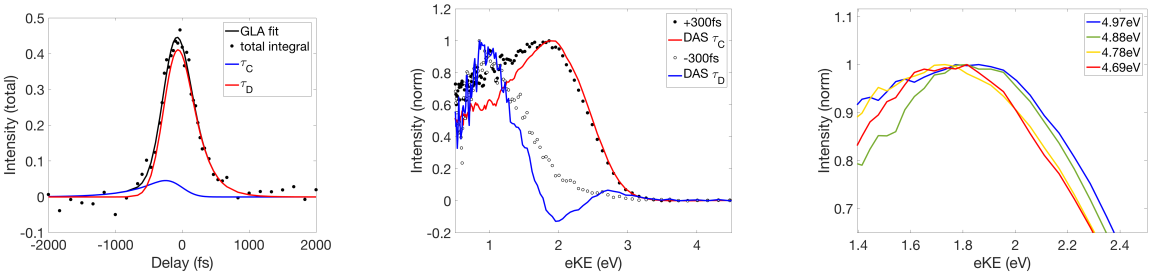

(a) Total integral (b) DAS_C and DAS_D (c) DAS_C comparison

Figure 3.6: GLA results for AMP photoexcited at 4.88eV and photodetached at 6.20eV, for positive delays: (a) kinetic components and total integrated intensity; (b) normalized DAS_C, DAS_D, and spectrum at ±300fs; (c) comparison of normalized DAS_C recovered for all pump photon energies.

invariant to the energy of the pump photon. Additionally, the photoelectron distribution extends ∼2eV above the peak, and the maximum eKE agrees well with the eKE of an electron vertically detached from S_0 at t_0. This suggests that some portion of the electron population in the excited state still has energy in excess of the lowest energy configuration of S_1. These observations both suggest that features A and C have not completely relaxed along the excited state. Consequently, the dynamics at positive delays are interpreted as follows. Within the IRF, the initially populated $\pi\pi^*$ excited state evolves. Then, this distribution undergoes internal conversion to S_0 on a timescale that is longer than the IRF.

When the system is pumped at 6.20eV, GLA only recovers a lifetime for DAS_D in AMP. DAS_B fully decays within the IRF and a lifetime cannot be accurately reported for the negative delays of Ado. Because the peak eKE of features B and D are similar (see Figures 3.3b and 3.4b), we posit that they arise from the same transition; however, the lack of measurable dynamics precludes a meaningful discussion of feature B. In contrast, DAS_D is

pump (eV)	**probe (eV)**	τ **(fs)**	**peak intensity** DAS_A **(eV)**
6.20	4.69 ... 4.97	<170.0	n/a
4.97	6.20	218.0 ± 26.3	1.8 ± 0.1
4.88	6.20	228.8 ± 30.1	1.7 ± 0.1
4.78	6.20	241.5 ± 28.1	1.7 ± 0.1
4.69	6.20	271.0 ± 71.0	1.6 ± 0.1

Table 3.1: Lifetimes and the location of the peak intensity in for DAS_A in Ado photoexcited and photodetached at UV photons ranging in energy from 4.69-6.20eV. The IRF is ~170fs.

seen to decay with a lifetime ranging from 290-350fs, as shown in Table 3.2. This is longer than that for all other pump photon energies, even though the probe photon at negative delays is considerably less energetic than at positive delays. Interpretation of DAS_D is not straightforward; DAS_D agrees with feature D below ~1.5eV but shows a markedly different intensity profile than that of feature D at higher eKEs. The intensity of DAS_D is positive above ~2.5eV, negative from ~1.3-2.5eV, and then positive again below ~1.3eV. Feature D, conversely, peaks near 1.7eV eKE, and its intensity extends nearly eKE 3eV above its peak. Remarkably, the peaks of features C and D agree to within error when the difference in detachment energy are taken into account (~4.4eV).

The shape of DAS_D in the high-eKE region is consistent with a population exchange between the >2.5 and 1.3-2.5eV regions. We note that this second kinetic component is necessary to obtain a reasonable GLA fit and that, strictly speaking, GLA cannot distinguish between a population transfer caused by the relaxation of a vibrationally hot electronic state or the internal conversion of one state to another.[57] However, the population exchange in DAS_D is between a higher- and lower-eKE region, which is characteristic of a shifting feature. This suggests a complex non-adiabatic relaxation process can be attributed to this portion of the photoelectron spectrum. The underpinnings of this finding will be discussed in Section 3.5.

3.5 Discussion

The photon energies used in this series of experiments access both the 260 and 200nm (4.77eV and 6.20eV) absorption bands observed in Ado and AMP. It is generally understood that a $\pi\pi^*$ transition is responsible for the 260nm (4.77eV) band[3, 6, 15, 62], while the 200nm (6.20eV) absorption band is believed to arise from higher-lying excited states also of $\pi\pi^*$ character.[49, 50] Here, pump energies ranging from 4.69-4.97eV are only able to excite the lowest $\pi\pi^*$ excited state, while the 6.20eV pump is also able to promote electrons into higher-

pump (eV)	**probe (eV)**	τ_C **(fs)**	**peak intensity** DAS_C **(eV)**
4.97	6.2	220.8 ± 30.3	1.9 ± 0.2
4.88	6.2	287.8 ± 67.5	1.9 ± 0.2
4.78	6.2	291.8 ± 43.4	1.7 ± 0.2
4.69	6.2	260.3 ± 30.0	1.8 ± 0.2
pump (eV)	**probe (eV)**	τ_D **(fs)**	**peak intensity** DAS_D **(eV)**
6.2	4.97	348.8 ± 52.8	0.8 ± 0.2
6.2	4.88	303.0 ± 82.8	0.7 ± 0.1
6.2	4.78	305.3 ± 119.9	0.6 ± 0.1
6.2	4.69	287.3 ± 108.9	0.7 ± 0.1

Table 3.2: Lifetimes and the location of the peak intensity in for DAS_C and DAS_D in AMP photoexcited and photodetached with photons ranging in energy from 4.69-6.20eV. The IRF is ∼170fs.

lying excited states. Previous studies have found a sub-500fs lifetime for the S_1 $\pi\pi^*$ excited state subsequent to photoexcitation near the band maximum.[12, 16–18, 33, 34, 37, 38, 40, 44] However, little is known about the photodeactivation dynamics of Ado and AMP excited at 6.20eV. We will now discuss the TRPES data presented in this paper in the context of this energetic picture (see Figure 3.2).

The lifetimes of Ado and AMP photoexcited at 4.69-4.97eV and photodetached at 6.20eV are found to decay with a sub-ps lifetime. General agreement between TRPES findings with those of both TA and FU measurements suggest that all observe the decay of the lowest lying $\pi\pi^*$, or fluorescent, excited state.[5] DAS_A and DAS_C peak near eKE 1.6eV, extend up to 3.6eV, and are not seen to shift. Taken as a whole, these results suggest the following mechanistic picture. First, the pump pulse initially populates S_1 with some excess energy. This nascent distribution then undergoes rapid relaxation to the energetic minimum with a lifetime that is somewhat faster than that of internal conversion to S_0. Once here, the population undergoes internal conversion to hot S_0 with a lifetime ranging from 220-270fs. Theoretical studies suggest that this CI is a nearly barrierless.[6]

To accurately report the excited state lifetime, the accessibility of the FC window should not be limited by the probe photon energy. A 5.21eV probe has been previously reported to be sufficiently energetic to access the FC window of S_1.[16] The 6.20eV probe used in the current experiments is then expected to access the photoionization FC window, regardless of pump energy, and not affect the measured lifetime. Both Ado and AMP exhibited S_1 relaxation dynamics that were consistent with previous TA, FU, and TRPES studies.[12, 16–18, 33, 34, 37–40, 44] Notably, however, the excited state lifetimes in this work are longer than those reported by Buchner and coworkers, who also studied Ado with TRPES on water microjets.[16] The lifetime of Ado photoexcited at 4.69eV and photodetached at 6.2eV in this study was found to agree to within error with the lifetime reported for a photoexcitation energy of 4.66eV and photodetachment energy of 5.0-5.21eV; although we note that the lifetime reported here is slightly longer and in better agreement with the lifetime reported by TA and FU studies. In contrast, when Ado was photoexcited at 5.0eV and photodetached at 4.66eV, the authors reported a lifetime of ∼143fs, which is significantly shorter than the lifetime of ∼218fs reported in this study subsequent to photoexcitation at 4.97eV and photodetachment at 6.20eV. This suggests that probe energies below 5.0eV are insufficient to access the FC window for the entire S_1 decay process.

The S_1 lifetime was also found to depend inversely on the pump photon energy. This trend was also observed by others[16, 18] and is explained simply as follows: if more excess energy is deposited into the excited state by the pump photon, then the wave packet motion to the S_1-S_0 CI will be faster. No contributions from other excited states were seen. In particular, there was no evidence for relaxation contributions from the nπ* state, which has been implicated to play a role in the deactivation dynamics of other nucleosides and nucleotides.[3, 5] This corroborates other TA findings[34, 44], which did not see any long-lived spectral contributions in Ado or AMP. Both Ado and AMP generally agree with the lifetime of S_1 in the biologically-relevant 9H Ade tautomer. This supports the findings of quantum chemistry calculations[5], which indicate that the aromatic ring of the nucleobase is principally responsible for the electronic structure and dynamics in NA constituents. Interestingly, the lifetime of S_1 in AMP was found to be slightly longer than in Ado. This has been reported by others[34, 44] as well but is a relatively small difference in lifetime as compared to differences seen in other nucleoside/tide pairs[37].

Finally, no evidence corresponding to vibrationally hot S_0 was found in the data. Presumably hot S_0 will lie energetically close to S_1 until it relaxes away, and it would not be wholly unreasonable to expect to see a signature of this at low eKE provided sufficient FC intensity. Pecourt and coworkers[34] observed thermal broadening of the S_0 absorption band at early times following photoexcitation of Ado at ∼4.77eV. This was attributed to vibrational cooling along S_0 and a lifetime of <2ps was ascribed to this process. Although the 6.20eV probe used in these experiments is quite energetic as compared to previous TRPES studies, it is obvious that a more energetic probe which can access the fully thermalized S_0 population (bound in excess of 7.5eV[13]) is required for a complete description of the photodeactivation of Ado and AMP by TRPES.

Markedly different dynamic behavior is observed for negative delays. The lifetime corresponding to DAS_D does not fit into the trend seen for the S_1 excited states at positive delays; given the high pump photon energy, the lifetime is expected to be shorter than those acquired at pump photon energies of 4.69-4.97eV if the 260nm absorption band was excited, but it is in fact longer. This suggests that different states are involved in the relaxation mechanism for AMP photoexcited at 6.20eV. This is reasonable, as the 6.20eV pump pulse is considerably more energetic than the center of the S_1 $\pi\pi$* absorption band and can access the ∼200nm absorption band known to exist in Ade-based DNA components. We then look to the transition responsible for the absorption band near ∼200nm (6.20eV). Study of this band is sparse, but it has been suggested that it is caused by one or more high-lying $\pi\pi^*$ states[7, 49], and we tentatively assign the observed negative-time dynamics to the deexcitation of this state. However, a close inspection of the data suggests that several states may be involved in the relaxation pathway giving rise to the 290-350fs lifetime. This is explored below.

Because only one kinetic component is required to fit the negative time data, and because the DAS shape indicates a shifting feature, the measured lifetime is thought to contain contributions from both relaxation and depletion processes. Given the relative differences in intensity of the different regions of the DAS, we suspect that most of the population—although somewhat less than seen in positive delays—has fully relaxed to the final excited state before it decays by internal conversion to hot S_0. Relating the intensity of DAS to population is not straightforward and the relative cross sections have not been accounted for, however, this picture is supported by the time-resolved spectra and is described herein. These data also aid in feature assignment in DAS_D. First, we note that the maximum eKE of feature D, which lies 3eV above the peak, is a reasonable difference in energy for two electronic states. The difference between the peak and maximum eKE of feature D is also larger in magnitude than the difference seen in either feature A or C, and further supports the notion that the pump pulse prepares an initial excited state that does not correspond to the 260nm absorption band. Second, we observe that, when the differences in detachment energy are accounted for, the peaks of features C and D agree. This suggests that population in this energy region of DAS_D could arise from the same electronic excited state as feature C, namely the S_1 excited state. This is supported by the observation that the lifetime of DAS_D increases as the variable probe photon energy increases. As discussed above for positive delays, the FC window of S_1 is only accessible for probe energies above 5.0eV. Probe photon energies for negative delays are 4.69-4.97eV.

Taken as a whole, we postulate the following deactivation pathway. First, the 6.20eV pump photon excites electrons into a high-lying $\pi\pi^*$ state, which is responsible for the modest intensity above eKE 2.5eV in DAS_D. This state then undergoes considerable nonadiabatic relaxation and shifts to a lower eKE region, indicated by the negative DAS_D intensity between ∼1.3-2.5eV. Finally, the electron population arrives at the S_1 $\pi\pi^*$ excited state, situated below ∼1.3eV in DAS_D, and is depleted by internal conversion to S_0. Mondal and Puranik[48] studied photoexcited Ade in solution at 200nm with resonance Raman and TD-DFT methods, and, although the ring distortions are somewhat different between the S_1 and higher-lying $\pi\pi^*$ state, posit that mode-specific coupling of the higher-lying $\pi\pi^*$ excited state to nearby states is possible. In particular, vibronic contributions from other electronic states to the absorption profile of Ade near 210-230nm were observed. Ultimately, however, more work is needed to fully understand the photodeactivation mechanism of AMP subsequent to excitation of the 200nm absorption band.

3.6 Conclusion

Femtosecond time-resolved photoelectron spectroscopy on water microjets has been used to interrogate the de-excitation dynamics of adenosine (Ado) and adenosine monophosphate (AMP) subsequent to photoexcitation at energies ranging from 4.69-6.20eV. This work looks at two absorption bands; 4.69-4.97eV photons populate the lowest $\pi\pi^*$ excited state, S_1, while 6.20eV photons excite a higher-lying $\pi\pi^*$ transition. In Ado, the excited state was found to decay with a lifetime of ∼220-270fs that inversely depends on the pump photon energy. Similarly, when AMP was photoexcited by photons in this energy regime, the excited state population was found to decay with a lifetime of ∼240-290fs. These lifetimes were assigned to the internal conversion of the S_1 $\pi\pi^*$ excited state to vibrationally hot S_0, and agree well with previous experiments. Upon photoexcitation at 6.20eV, a transient signal at low eKE was evident in both Ado and AMP. Notably, a lifetime for this signal was only measureable in AMP, and was found to be 290-350fs. Spectral analysis suggests that a high-lying $\pi\pi^*$ excited state is initially populated, but ultimately relaxes to the S_1 $\pi\pi^*$ excited state before internal conversion to hot S_0. Further study is required for a comprehensive understanding of the dynamics of Ado and AMP subsequent to photoexcitation at 6.20eV.

3.7 Acknowledgements

This work was funded by the National Science Foundation under the grant CHE-1663832 and by the Air Force Office of Scientific Research under the Multidisciplinary University Initiative, grant number 24086151-01. The data presented here are available on request sent to dneumark@berkeley.edu.

3.8 References

1. Ravanat, J.-L., Douki, T. & Cadet, J. Direct and indirect effects of UV radiation on DNA and its components. *J. Photochem. Photobiol. B: Biol.* **63,** 88 (2001).
2. Cadet, J., Mouret, S., Ravanat, J.-L. & Douki, T. Photoinduced damage to cellular DNA: Direct and photosensitized reactions. *Photochem. Photobiol.* **88,** 1048 (2012).
3. *Photoinduced phenomena in nucleic acids I: Nucleobases in the gas phase and in solvents* (eds Barbatti, M., Borin, A. C. & Ullrich, S.) (Springer International Publishing, Cham, 2015).

4. Middleton, C. T. *et al.* DNA excited-state dynamics: From single bases to the double helix. *Annu. Rev. Phys. Chem.* **60,** 217 (2009).
5. Crespo-Hernández, C. E., Cohen, B., Hare, P. M. & Kohler, B. Ultrafast excited-state dynamics in nucleic acids. *Chem. Rev.* **104,** 1977 (2004).
6. Improta, R., Santoro, F. & Blancafort, L. Quantum mechanical studies on the photophysics and the photochemistry of nucleic acids and nucleobases. *Chem. Rev.* **116,** 3540 (2016).
7. Shukla, M. K. & Leszczynski, J. Electronic spectra, excited state structures and interactions of nucleic acid bases and base assemblies: A review. *J. Biomol. Struct. Dyn.* **25,** 93 (2007).
8. Saigusa, H. Excited-state dynamics of isolated nucleic acid bases and their clusters. *J. Photochem. Photobiol. C: Photochem. Rev.* **7,** 197 (2006).
9. De Vries, M. S. & Hobza, P. Gas-phase spectroscopy of biomolecular building blocks. *Annu. Rev. Phys. Chem.* **58,** 585 (2007).
10. Chatterley, A. S., West, C. W., Roberts, G. M., Stavros, V. G. & Verlet, J. R. R. Mapping the ultrafast dynamics of adenine onto its nucleotide and oligonucleotides by time-resolved photoelectron imaging. *J. Phys. Chem. Lett.* **5,** 843 (2014).
11. De Camillis, S. *et al.* Ultrafast non-radiative decay of gas-phase nucleosides. *Phys. Chem. Chem. Phys.* **17,** 23643 (2015).
12. Cohen, B., Hare, P. M. & Kohler, B. Ultrafast excited-state dynamics of adenine and monomethylated adenines in solution: Implications for the nonradiative decay mechanism. *J. Am. Chem. Soc.* **125,** 13594 (2003).
13. Pluhařová, E., Jungwirth, P., Bradforth, S. E. & Slavíček, P. Ionization of purine tautomers in nucleobases, nucleosides, and nucleotides: From the gas phase to the aqueous environment. *J. Phys. Chem. B* **115,** 1294 (2011).
14. Seidel, R., Winter, B. & Bradforth, S. E. Valence electronic structure of aqueous solutions: Insights from photoelectron spectroscopy. *Annu. Rev. Phys. Chem.* **67,** 283 (2016).
15. Voet, D., Gratzer, W. B., Cox, R. A. & Doty, P. Absorption spectra of nucleotides, polynucleotides, and nucleic acids in the far ultraviolet. *Biopolymers* **1,** 193 (1963).
16. Buchner, F., Ritze, H.-H., Lahl, J. & Lübcke, A. Time-resolved photoelectron spectroscopy of adenine and adenosine in aqueous solution. *Phys. Chem. Chem. Phys.* **15,** 11402 (2013).
17. Gustavsson, T., Sharonov, A., Onidas, D. & Markovitsi, D. Adenine, deoxyadenosine and deoxyadenosine 5'-monophosphate studied by femtosecond fluorescence upconversion spectroscopy. *Chem. Phys. Lett.* **356,** 49 (2002).

18. Pancur, T., Schwalb, N. K., Renth, F. & Temps, F. Femtosecond fluorescence up-conversion spectroscopy of adenine and adenosine: Experimental evidence for the $\pi\sigma^*$ state? *Chem. Phys.* **313,** 199 (2005).

19. Evans, N. L. & Ullrich, S. Wavelength dependence of electronic relaxation in isolated adenine using UV femtosecond time-resolved photoelectron spectroscopy. *J. Phys. Chem. A* **114,** 11225 (2010).

20. Ullrich, S., Schultz, T., Zgierski, M. Z. & Stolow, A. Electronic relaxation dynamics in DNA and RNA bases studied by time-resolved photoelectron spectroscopy. *Phys. Chem. Chem. Phys.* **6,** 2796 (2004).

21. Canuel, C. *et al.* Excited states dynamics of DNA and RNA bases: Characterization of a stepwise deactivation pathway in the gas phase. *J. Chem. Phys.* **122,** 074316 (2005).

22. Barbatti, M. *et al.* Relaxation mechanisms of UV-photoexcited DNA and RNA nucleobases. *Proc. Natl. Acad. Sci. U. S. A.* **107,** 21453 (2010).

23. Barbatti, M., Aquino, A. J. A. & Lischka, H. The UV absorption of nucleobases: Semi-classical ab initio spectra simulations. *Phys. Chem. Chem. Phys.* **12,** 4959 (2010).

24. Perun, S., Sobolewski, A. L. & Domcke, W. Ab initio studies on the radiationless decay mechanisms of the lowest excited singlet states of 9H-adenine. *J. Am. Chem. Soc.* **127,** 6257 (2005).

25. Barbatti, M. & Ullrich, S. Ionization potentials of adenine along the internal conversion pathways. *Phys. Chem. Chem. Phys.* **13,** 15492 (2011).

26. Serrano-Andrés, L., Merchán, M. & Borin, A. C. Adenine and 2-aminopurine: Paradigms of modern theoretical photochemistry. *Proc. Natl. Acad. Sci. U.S.A.* **103,** 8691 (2006).

27. Serrano-Andrés, L., Merchán, M. & Borin, A. C. A three-state model for the photophysics of adenine. *Chem. Eur. J* **12,** 6559 (2006).

28. Blancafort, L. Excited-state potential energy surface for the photophysics of adenine. *J. Am. Chem. Soc.* **128,** 210 (2006).

29. Conti, I., Garavelli, M. & Orlandi, G. Deciphering low energy deactivation channels in adenine. *J. Am. Chem. Soc.* **131,** 16108 (2009).

30. Mennucci, B., Toniolo, A. & Tomasi, J. Theoretical study of the photophysics of adenine in solution: Tautomerism, deactivation mechanisms, and comparison with the 2-aminopurine fluorescent isomer. *J. Phys. Chem. A* **105,** 4749 (2001).

31. Yamazaki, S. & Kato, S. Solvent effect on conical intersections in excited-state 9H-adenine: Radiationless decay mechanism in polar solvent. *J. Am. Chem. Soc.* **129,** 2901 (2007).

32. Santoro, F. *et al.* Relative stability of the L_a and L_b excited states in adenine and guanine: Direct evidence from TD-DFT calculations of MCD spectra. *J. Phys. Chem. Lett.* **5,** 1806 (2014).

33. Pecourt, J.-M. L., Peon, J. & Kohler, B. Ultrafast internal conversion of electronically excited RNA and DNA nucleosides in water. *J. Am. Chem. Soc.* **122,** 9348 (2000).

34. Pecourt, J.-M. L., Peon, J. & Kohler, B. DNA excited-state dynamics: Ultrafast internal conversion and vibrational cooling in a series of nucleosides. *J. Am. Chem. Soc.* **123,** 10370 (2001).

35. Lan, Z., Lu, Y., Fabiano, E. & Thiel, W. QM/MM nonadiabatic decay dynamics of 9H-adenine in aqueous solution. *Chemphyschem* **12,** 1989 (2011).

36. Ludwig, V. *et al.* Photophysics and photostability of adenine in aqueous solution: A theoretical study. *Chem. Phys. Lett.* **492,** 164 (2010).

37. Peon, J. & Zewail, A. H. DNA/RNA nucleotides and nucleosides: Direct measurement of excited-state lifetimes by femtosecond fluorescence up-conversion. *Chem. Phys. Lett.* **348,** 255 (2001).

38. Onidas, D., Markovitsi, D., Marguet, S., Sharonov, A. & Gustavsson, T. Fluorescence properties of DNA nucleosides and nucleotides: A refined steady-state and femtosecond investigation. *J. Phys. Chem. B* **106,** 11367 (2002).

39. Stuhldreier, M. C. & Temps, F. Ultrafast photo-initiated molecular quantum dynamics in the DNA dinucleotide d(ApG) revealed by broadband transient absorption spectroscopy. *Faraday Discuss.* **163,** 173 (2013).

40. Kwok, W.-M., Ma, C. & Phillips, D. L. Femtosecond time- and wavelength-resolved fluorescence and absorption spectroscopic study of the excited states of adenosine and an adenine oligomer. *J. Am. Chem. Soc.* **128,** 11894 (2006).

41. Gustavsson, T. *et al.* A joint experimental/theoretical study of the ultrafast excited state deactivation of deoxyadenosine and 9-methyladenine in water and acetonitrile. *Photochem. Photobiol. Sci.* **12,** 1375 (2013).

42. Improta, R. & Barone, V. The excited states of adenine and thymine nucleoside and nucleotide in aqueous solution: A comparative study by time-dependent DFT calculations. *Theor. Chem. Acc.* **120,** 491 (2008).

43. Platt, J. R. Classification of spectra of cata-condensed hydrocarbons. *J. Chem. Phys.* **17,** 484 (1949).

44. Crespo-Hernández, C. E., Cohen, B. & Kohler, B. Base stacking controls excited-state dynamics in A·T DNA. *Nature* **436,** 1141 (2005).

45. Sprecher, C. A. & Johnson, W. C. Circular dichroism of the nucleic acid monomers. *Biopolymers* **16,** 2243 (1977).

46. Holmén, A., Broo, A., Albinsson, B. & Nordén, B. Assignment of electronic transition moment directions of adenine from linear dichroism measurements. *J. Am. Chem. Soc.* **119,** 12240 (1997).

47. Voelter, W., Records, R., Bunnenberg, E. & Djerassi, C. Magnetic circular dichroism studies. VI. Investigation of some purines, pyrimidines, and nucleosides. *J. Am. Chem. Soc.* **90,** 6163 (1968).
48. Mondal, S. & Puranik, M. Ultrafast structural dynamics of photoexcited adenine. *Phys. Chem. Chem. Phys.* **19,** 20224 (2017).
49. Fülscher, M. P., Serrano-Andrés, L. & Roos, B. O. A theoretical study of the electronic spectra of adenine and guanine. *J. Am. Chem. Soc.* **119,** 6168 (1997).
50. Clark, L. B. Transition moments of 2'-deoxyadenosine. *J. Phys. Chem.* **99,** 4466 (1965).
51. Perun, S., Sobolewski, A. L. & Domcke, W. Photostability of 9H-adenine: Mechanisms of the radiationless deactivation of the lowest excited singlet states. *Chem. Phys.* **313,** 107 (2005).
52. Faubel, M., Schlemmer, S. & Toennies, J. P. A molecular beam study of the evaporation of water from a liquid jet. *Z. Phys. D: At., Mol. Clusters* **10,** 269 (1988).
53. Smith, J. D., Cappa, C. D., Drisdell, W. S., Cohen, R. C. & Saykally, R. J. Raman thermometry measurements of free evaporation from liquid water droplets. *J. Am. Chem. Soc.* **128,** 12892 (2006).
54. Wilson, K. R. *et al.* Investigation of volatile liquid surfaces by synchrotron X-ray spectroscopy of liquid microjets. *Rev. Sci. Instrum.* **75,** 725 (2004).
55. Shreve, A. T., Elkins, M. H. & Neumark, D. M. Photoelectron spectroscopy of solvated electrons in alcohol and acetonitrile microjets. *Chem. Sci.* **4,** 1633 (2013).
56. Shreve, A. T., Yen, T. A. & Neumark, D. M. Photoelectron spectroscopy of hydrated electrons. *Chem. Phys. Lett.* **493,** 216 (2010).
57. Elkins, M. H., Williams, H. L. & Neumark, D. M. Dynamics of electron solvation in methanol: Excited state relaxation and generation by charge-transfer-to-solvent. *J. Chem. Phys.* **142,** 234501 (2015).
58. Elkins, M. H., Williams, H. L. & Neumark, D. M. Isotope effect on hydrated electron relaxation dynamics studied with time-resolved liquid jet photoelectron spectroscopy. *J. Chem. Phys.* **144,** 184503 (2016).
59. Kruit, P. & Read, F. H. Magnetic field paralleliser for 2π electron-spectrometer and electron-image magnifier. *J. Phys. E: Sci. Instrum.* **16,** 313 (1983).
60. Van Stokkum, I. H. M., Larsen, D. S. & van Grondelle, R. Global and target analysis of time-resolved spectra. *Biochim. Biophys. Acta* **1657,** 82 (2004).
61. Knutson, J. R., Davenport, L. & Brand, L. Anisotropy decay associated fluorescence spectra and analysis of rotational heterogeneity. 1. Theory and applications. *Biochemistry* **25,** 1805 (1986).
62. Callis, P. R. Electronic states and luminescence of nucleic acid systems. *Annu. Rev. Phys. Chem.* **34,** 329 (1983).

Part III

High Harmonic Generation for Future Experiments

Chapter 4

Principles of High Harmonic Generation

4.1 Overview

The electronic ground state of most solvated species is bound in excess of the fourth harmonic of our laser (6.2eV).[1] To photodetach these states, a more energetic probe pulse is needed than can be generated by a traditional solid state non-linear crystal. Instead, a noble gas will be used as the non-linear medium to upconvert the fundamental to energies on the order of 10eV—this technique is called high harmonic generation (HHG).

High harmonic generation has enabled table-top extreme ultraviolet (XUV) and soft X-ray femtosecond and attosecond science.[2–9] Previously, only large synchrotron light sources and free-electron lasers could access this energy regime, generally with nano- to picosecond capabilities.[10] We will implement a widely-used technique—HHG by a semi-infinite gas cell (SIGC)—and aim to generate harmonics ranging from 20-100eV with our new setup, "XUV femtosecond time-resolved photoelectron spectroscopy in liquid microjets (XUV LPES)." As of this writing, the apparatus has been largely designed and is being built, but harmonics have yet to be generated. Herein, the principles of HHG will be discussed; Chapter 5 will focus on instrumental design.

4.2 Three Step Model

Under the influence of an intense laser field, the Coulomb potential of an atom can be significantly distorted such that a valence electron readily tunnel ionizes.[2, 3] The interaction of such a laser with a single atom was first described (semi-classically) by Paul Corkum with

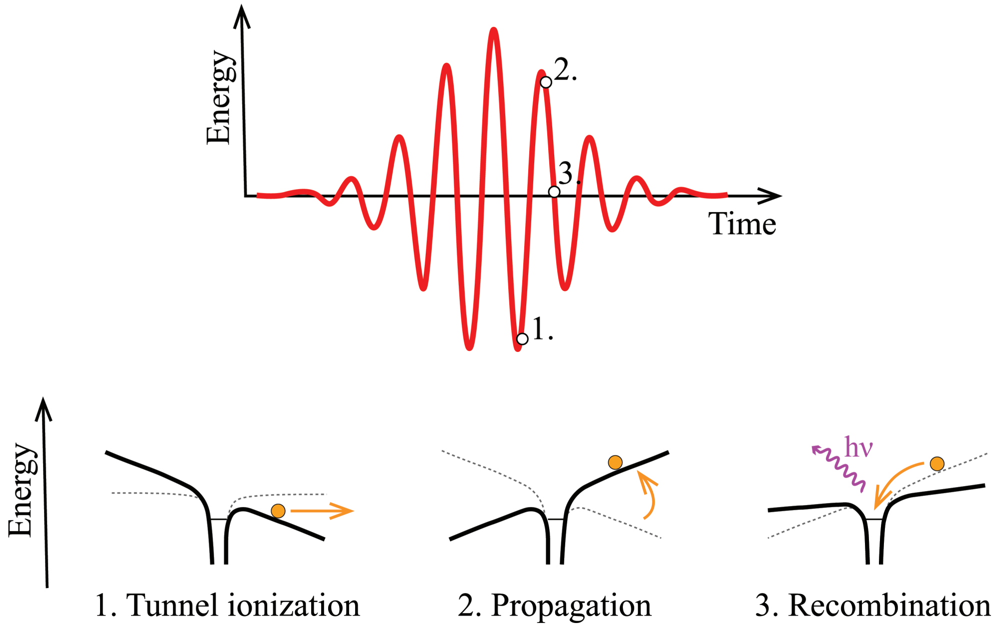

Figure 4.1: The Three Step Model of HHG. The driving laser pulse is pictured on top, with the locations of the three steps indicated, for one cycle, by open circles. The distorted Coulomb potential and electron motion corresponding to each step are shown below. Adapted from Reference [10].

his so-called "three step model".[5, 11] This is summarized in Figure 4.1. First, the electron tunnel ionizes near the peak of the laser field, when the distortion of the Coulomb potential is greatest. Once unbound, the electron is influenced wholly by the field of the laser. The electron is accelerated away from the parent atom until the laser field changes sign. Then, it is accelerated back to the atom core, picking up kinetic energy along the way. Finally, the electron and core radiatively recombine.

This process repeats for the duration of the driving field, such that an XUV burst is emitted every half cycle of the laser. The energy of the XUV photons correspond to odd, integer multiples of the driving fundamental. Because the non-linear medium must possess inversion symmetry, even harmonics are forbidden.[10]

The energy of the emitted photon is given by Equation 4.1, where I_P is the ionization potential of the atom and $\bar{T}$ is the average kinetic energy the electron gains in the continuum.

$$E_{XUV} = I_P + \bar{T} \tag{4.1}$$

We can readily see from Equation 4.1 that different energy regimes can be accessed by

element	Xe	Kr	Ar	Ne	He
I_p **(eV)**	12.13	13.99	15.76	21.56	24.58

Table 4.1: Ionization potentials of the noble gases.

tunnel ionizing target gases with different ionization potentials.[12] The ionization potentials of the noble gases typically used in HHG are presented in Table 4.1.

Notably, two different electron trajectories can result the same kinetic energy at the time of the electron-core recombination. These are referred to as the "short" and "long" trajectories, in accordance with their respective travel times of 1/2 and one optical period.[4, 13] The interference of these two electron quantum paths depends on their different dipole phases, and control of this effect can be used to modify the properties of the emitted harmonics.[10]

Because this ionization process is synchronized to the sub-cycles of the laser pulse, the photons are inherently emitted in ultrashort bursts of radiation.[1] In attosecond science, the driving pulses are few-cycle to facilitate the generation of an attosecond train of XUV pulses. Future XUV LPES experiments will only use one selected harmonic and will have a driving field that has a FWHM of 35fs.[2]

4.2.1 Cut-Off Energy

High harmonic generation is a strong field phenomenon and is thus non-perturbative. This has a number of consequences, including the fact that high order harmonics are equally intense up to a "cut-off energy".[10] This is distinct from the BBO-based SFG processes (see Section 2.6.1) by which lower order harmonics are typically generated. These low order harmonics are generated in the weak field, or perturbative, regime where the probability of a n-photon excitation process decreases exponentially with n.[3]

The strong and weak field regimes are distinguished by the Keldysh parameter (see Figure 4.2).[10] This is defined in Equation 4.2, where γ is the Keldysh parameter and U_p is the ponderomotive energy. If $\gamma \ll 1$, tunnel ionization occurs; if $\gamma \gg 1$, multiphoton ionization occurs because the tunneling time is longer than the laser period.

---

[1] This is a consequence of the energy-time uncertainty principle—shorter pulses have broader spectral bandwidth and *vice versa*.

[2] So, the time duration of the XUV pulse will be on the order of tens of femtoseconds.

[3] This is because only a single photon can be emitted for n photons absorbed.

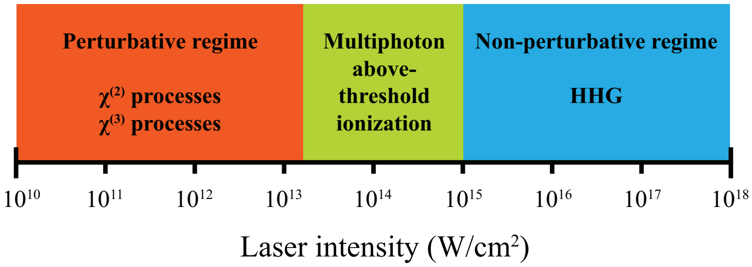

Figure 4.2: Different nonlinear effects generated in various laser intensity regimes. Adapted from Reference [6].

$$\gamma = \sqrt{\frac{I_p}{2U_p}} \tag{4.2}$$

The maximum XUV photon energy—or cut-off energy—is determined by the maximum kinetic energy of the photoionized electron and I_p of the parent atom. This is defined in Equation 4.3, where E_{cutoff} is the cut-off energy. The maximum kinetic energy is $\sim 3.17U_p$.[4]

$$E_{cutoff} = 3.17U_p + I_p \tag{4.3}$$

The ponderomotive energy is defined in Equation 4.4, where q is the charge of an electron, E_0 is the amplitude of the laser field, m_e is the electron mass, and ω_0 is the driving laser frequency. Physically, this is the kinetic energy the ionized electron gains in the continuum.

$$U_p = \frac{q^2 {E_0}^2}{4m_e {\omega_0}^2} \tag{4.4}$$

4.2.2 Propagation Effects

High harmonic generation involves many atoms which are coherently excited by the driving laser pulse; however, the three step model only considers the microscopic case of a single atom. To adequately describe the phase matching conditions—that is to say, the phase

---

[4] This is numerically calculated by determining the kinetic energy of the electrons when they recombine with the core at various phases of the laser field. Maximum kinetic energy in imparted when the electron is ionized at a phase of 18°, near the peak of the laser field!

relationship that must be maintained during propagation of the fundamental and XUV beams for coherent radiative emission—we must consider the macroscopic limit (*i.e.* the many atom case).[10, 14, 15] The wavevector mismatch between the driving pulse and the XUV in a collinear geometry can be described by Equation 4.5, where $\vec{k}$ is the phase vector and m is the mth harmonic of ω_0.

$$\Delta k = m\vec{k}_{\omega_f} - \vec{k}_{m\omega_f} \tag{4.5}$$

To achieve proper phase matching, Δk must tend to zero in the macroscopic limit.[16] Dispersion off the neutral gas, off the laser-generated plasma, and that arising from the geometry of the HHG apparatus itself will all affect the phase matching conditions.

Finally, it is important to note the additional constraints imposed on HHG in the macroscopic regime. In the single atom limit, the cut-off energy can be extended by increasing the laser intensity and decreasing the laser frequency (see Equation 4.4); however, in the macroscopic limit this tunability is hampered.[17] Effects from plasma generation at high laser intensities and decreased recombination efficiencies at longer driving wavelengths ultimately limit the ability to shift the cut-off energy.[6] Reabsorption of harmonics by the parent atoms also poses a considerable problem at high laser intensity.

Photoabsorption cross sections of HHG by the generation gas medium are generally high, owing in part to the large photon energy.[10] The absorption length, L_a, is the distance light can propagate before its intensity drops by $^1/_e$, and is described by Equation 4.6, where ρ is the gas density and σ is the absorption cross section of the gas.

$$L_a = \rho\sigma \tag{4.6}$$

The intensity of the generated harmonics would increase as the square of the length of the gas medium, L, *sans* these absorption effects. Under ideal phase-matching conditions, the coherence length, L_c, of the harmonics—defined as $^\pi/_{\Delta k}$—is much greater than L_a. Practically, in order to produce roughly half the maximum HHG intensity for long coherence and propagation lengths, the conditions in Equation 4.7 must be met.[10]

$$\begin{aligned} L &> 3L_a \\ L_c &> 5L_a \end{aligned} \tag{4.7}$$

technique	**length**	**pressure (Torr)**
PV	1 - 2mm	10
FGC	$\mathcal{O}$(confocal parameter)	<50
SIGC	N × confocal parameter	100

Table 4.2: Comparison of different HHG methods. Adapted from Reference [18].

4.3 HHG Methods

High harmonic generation can be practically implemented by tightly focusing the driving laser pulse into a rare gas target. Pulsed valves (PVs), finite gas cells (FGCs), and semi-infinite gas cells (SIGCs) are all common approaches to gas-based HHG.[18] These are briefly compared in Table 4.2.

As we have seen in the sections above, the efficiency of HHG depends on several parameters, chief among them the 1) number density of the gas, 2) length of the interaction region, 3) reabsorption by the gas, and 4) quasi-phase matching. We can see that SIGCs are favorable due to their long interaction length and high gas density. Additionally, with its with a simple geometry and loose focus, implementation of this configuration is relatively straightforward.

In a SIGC, the driving laser beam is focused at the pinhole exit of cell filled with some amount of noble gas. The gas cell is "semi-infinite" because the propagation length is several times the confocal parameter. As a result of this design, the harmonic flux is typically greater from a SIGC as compared to other HHG techniques—conversion efficiencies are in excess of 10^{-6}.[18] Conversely, these parameters also favor re-absorption of the harmonics by the medium. The implementation of a SIGC will be discussed at length in Section 5.2.

4.4 References

1. Seidel, R., Winter, B. & Bradforth, S. E. Valence electronic structure of aqueous solutions: Insights from photoelectron spectroscopy. *Annu. Rev. Phys. Chem.* **67,** 283 (2016).
2. Ferray, M. *et al.* Multiple-harmonic conversion of 1064 nm radiation in rare gases. *J. Phys. B At. Mol. Opt. Phys.* **21,** L31 (1988).
3. McPherson, A. *et al.* Studies of multiphoton production of vacuum-ultraviolet radiation in the rare gases. *J. Opt. Soc. Am. B* **4,** 595 (1987).

4. Lewenstein, M., Balcou, P., Ivanov, M. Y., L'Huillier, A. & Corkum, P. B. Theory of high-harmonic generation by low-frequency laser fields. *Phys. Rev. A* **49,** 2117 (1994).
5. Corkum, P. B. Plasma perspective on strong field multiphoton ionization. *Phys. Rev. Lett.* **71,** 1994 (1993).
6. Brabec, T. & Krausz, F. Intense few-cycle laser fields: Frontiers of nonlinear optics. *Rev. Mod. Phys.* **72,** 545 (2000).
7. Popmintchev, T., Chen, M.-C., Arpin, P., Murnane, M. M. & Kapteyn, H. C. The attosecond nonlinear optics of bright coherent X-ray generation. *Nature Photonics,* 822 (2010).
8. Ramasesha, K., Leone, S. R. & Neumark, D. M. Real-time probing of electron dynamics using attosecond time-resolved spectroscopy. *Annu. Rev. Phys. Chem.* **67,** 41 (2016).
9. Chang, Z., Corkum, P. B. & Leone, S. R. Attosecond optics and technology: Progress to date and future prospects. *J. Opt. Soc. Am. B* **33,** 1081 (2016).
10. Pfeifer, T., Spielmann, C. & Gerber, G. Femtosecond X-ray science. *Rep. Prog. Phys.* **69,** 443 (2006).
11. Corkum, P. B. & Krausz, F. Attosecond science. *Nature Physics* **3,** 381 (2007).
12. Chang, Z. *Fundamentals of attosecond optics* (CRC Press, Boca Raton, 2011).
13. Lewenstein, M., Salières, P. & L'Huillier, A. Phase of the atomic polarization in high-order harmonic generation. *Phys. Rev. A* **52,** 4747 (1995).
14. Mette, B. G., Jennifer, L. T. & Kenneth, J. S. Macroscopic aspects of attosecond pulse generation. *J. Phys. B At. Mol. Opt. Phys.* **41,** 132001 (2008).
15. Salières, P. & Christov, I. *Strong field laser physics* (Springer New York, New York, NY, 2009).
16. Rundquist, A. *et al.* Phase-matched generation of coherent soft X-rays. *Science* **280,** 1412 (1998).
17. Shiner, A. D. *et al.* Wavelength scaling of high harmonic generation efficiency. *Phys. Rev. Lett.* **103,** 073902 (2009).
18. Brichta, J.-P. *et al.* Comparison and real-time monitoring of high-order harmonic generation in different sources. *Phys. Rev. A* **79,** 033404 (2009).

Chapter 5

Design of a New XUV Source

5.1 Overview

The XUV LPES apparatus will comprise three distinct regions under vacuum: (1) the SIGC, (2) the XUV analyzer, and (3) the harmonic selection and pump-probe collinear recombination regions. The output of the Astrella will be split between this new XUV probe arm and the TOPAS-Prime, which will generate the tunable UV pump pulse. No changes to the liquid microjet trap and magnetic bottle chambers are expected at this time. An overview of the new XUV source can be seen in Figure 5.1 and machine drawings are in Appendix C.

All of the vacuum chambers in these regions will be secured to a new laser table system (Newport, RS2000 series) that has been recently installed. Our narrow room necessitates a somewhat strange table geometry. One 4' × 10' × 12" table is monolithically joined in a side-by-side configuration to another 4' × 12' × 12" table. The tables are offset length-wise[1] by 4' and are each supported by four rigid legs 23.5" in height. The Astrella and TOPAS-Prime sit on the 10' long table and the XUV source will sit on the 12' long table. These tables are *not* floating because they must be precisely coupled to the rigid liquid microjet and magnetic bottle chambers which are externally supported.

The microjet and magnetic bottle chambers are mounted on a new frame designed by Eric Granlund. This frame is made of T-slotted aluminum framing (80/20 Inc.). Two inches of travel across both the x- and y-planes of the frame are afforded by a home-built manually adjustable two-axis rail system. This is critical to the proper alignment of the apparatus—the microjet and XUV beam line positions are fixed, necessitating another degree of freedom to align the XUV beam onto the microjet.

---

[1] Like a left snake tetromino

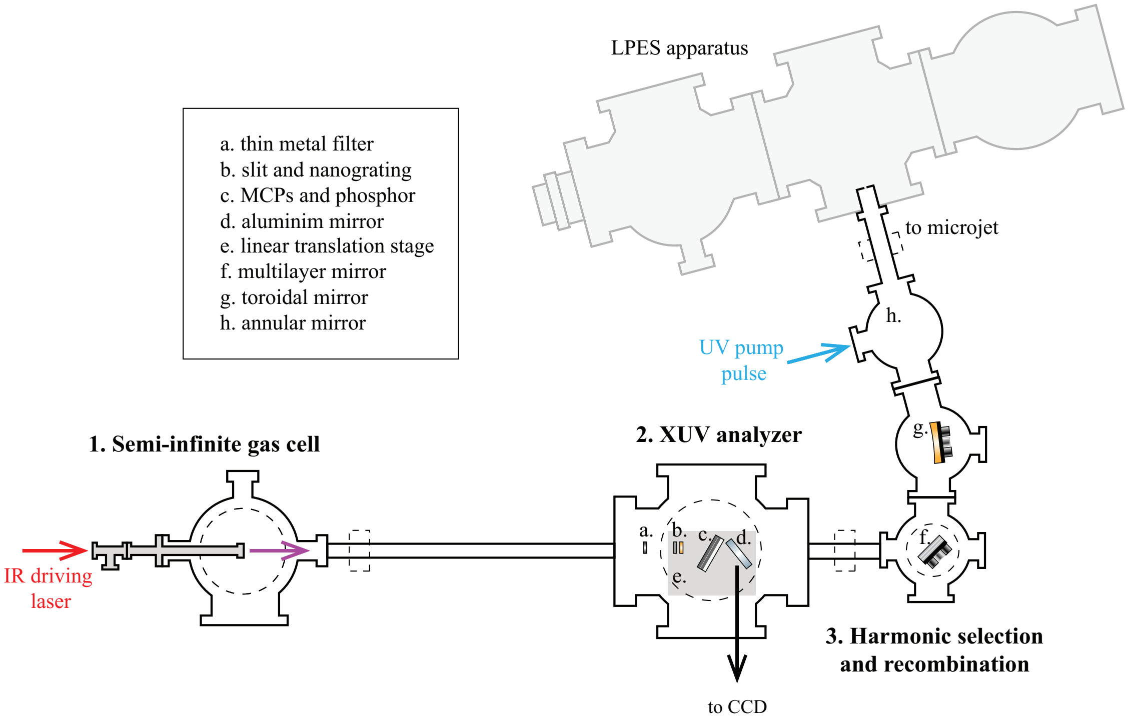

Figure 5.1: Schematic of the new XUV source (top view). Dashed circles indicate where turbomolecular pumps are located, and dashed rectangles indicate gate valves. A key identifying internal components can be found in the upper left corner of the figure.

The chambers are differentially pumped by three turbomolecular pumps (Leybold, TURBOVAC 1000C and TURBOVAC 450i) with a combined pumping speed of 1900$^{L}/_{s}$.[1] Each turbomolecular pump is backed by a rotary vane roughing pump (Pfeiffer, DUO 11 M). Because of space constraints, the turbomolecular pumps are mounted on top of the chambers. Other femtosecond HHG-based experiments in the Leone group at UC Berkeley employ a similar design and have not found considerable issues with vibrational stability. Several gate valves joined to small segments of formed bellows allow for easy venting of select regions of the XUV source. These will also need to be routed into an interlock system to protect the custom optical components from ice fragments that can fly off of frozen microjets. Additional uninterruptible power supplies will also need to be installed to protect the turbomolecular pumps in the event of a power outage.

5.2 Semi-Infinite Gas Cell

The SIGC configuration chosen was originally designed by Eric R. Hosler and Andrew R. Attar.[2, 3] The designs were updated with the help of Eric Granlund.

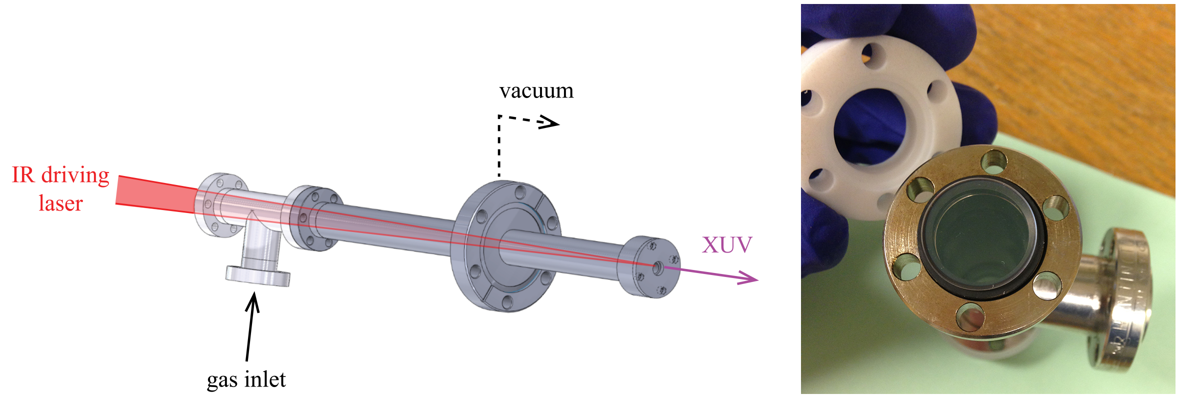

(a) Schematic of the SIGC (b) SIGC top view

Figure 5.2: The semi-infinite gas cell (a) The IR driving laser pulse is focused into the SIGC which is filled with the noble gas; (b) The Teflon cap, Viton gasket, and custom entrance window.

The cell comprises an anti-reflective coated window mounted to a 1-1/3" mini-CF tee that is mated to a capped 1" diameter tube.[2] This is shown in Figure 5.2. The window is 3/4" ø × 1mm and was custom-made by CVI Laser Optics (W1-PW1-0704-UV-800-0). It sits inside a Teflon flange, and a Viton CF gasket with a flat cross-section is used to mate the seal with the mini-CF tee (see Figure 5.2b). The cap at the opposite end of the gas tube holds a Viton O-ring (Sealing Devices Inc., 2-032) and a replaceable thin Teflon disk[3] (0.5"ø × 0.03"), which is drilled through by the focused fundamental laser beam. The total distance between the mini-CF tee input and the Teflon disk output is 14". A 2-3/4" CF flange sits midway along the tube to mount the cell to a vacuum chamber for differential pumping.

The cell is filled with gas through the mini-CF tee and the positive pressure in the SIGC is monitored with a Baratron gauge (MKS Instruments, 622C13TBE). The harmonics exit the cell through the hole in the Teflon disk, which sits in the center of a 10" to 8" CF reducing tee vacuum chamber. An 8" acrylic flange serves as a viewport. The 10" tube is equipped with three 2-3/4" ports: two are perpendicular to the 8" half nipple and serve as the input and output for the SIGC, while the third is welded across from the 8" half nipple and serves as a port for a thermocouple gauge to measure pressure in the chamber. The $1000\,{}^{L}\!/_{s}$ turbomolecular pump should afford chamber pressures of a few milliTorr.

---

[2] Plate nuts are used *in lieu* of standard hex nuts because of the limited clearance between the flange and the tubing.

[3] The Teflon disk is punched using a hammer-driven steel hole punch (McMaster-Carr, 3427A15), but a shim punch could also be used if a cleaner cut is needed (Precision Brand, 40105).

A short length of formed bellows and a gate valve (VAT Incorporated) are mated to the 2-3/4" output arm to allow this region to be readily isolated from the high-vacuum chambers downstream. Based on discussions with members of the Leone group, we expect to change the thin Teflon disk every week. A ~65cm-long stainless steel tube then connects the gate valve to the XUV analyzer region. At least 1m of defocussing length is required to prevent the residual fundamental from burning through the thin metal filters positioned at the entrance of the XUV analyzer.

Finally, instead of using standard copper gaskets, copper plates with holes drilled in the centerline are used to facilitate differential pumping between the SIGC and SUV analyzer and to block any scattered light. Based on discussions with members of the helium nanodroplet collaboration with Oliver Gessner at Lawrence Berkeley Laboratory, three plates will be implemented between the SIGC and the beam analyzer. These connect the formed bellows to the SIGC vacuum chamber, the gate valve to the defocussing tube, and the defocussing tube to the analyzer. The diameters of the drilled holes are 10, 8, and 6mm, respectively.

5.3 XUV Analyzer

In order to recover the eBE of the photoelectron spectral features, and to optimize SIGC parameters, the XUV probe pulse must be characterized. To this end, an XUV analyzer will be used. It is heavily inspired by the device used by the Gessner group.[4, 5] It comprises an XUV spectrometer and beam profiler. Because the analyzer is of considerable size and has several vacuum feedthroughs, a 6-way, 10" CF cross from the liquid microjet apparatus was re-purposed. This was originally used to house the 7L liquid nitrogen dewar and has been since replaced by a 4-way, 10" CF cross. Figure 5.3 shows the analyzer in detail.

The XUV beam first passes through a beam enclosure tube to a 50μm wide and 3mm long precision laser-drilled slit (Lenox Laser, mounted A-SLIT-3/8-DISC). Then, it passes through a transmission nanograting with an 100nm period (LumArray Inc.) at 0° incidence. Harmonics are horizontally separated in space by the nanograting; the slit is used to ensure that different harmonics do not significantly overlap as this would complicate analysis considerably. The diffraction angle, φ, for this geometry is given by Equation 5.1, where η is the diffraction order, λ is the XUV wavelength, and d is the grating period.

$$sin\varphi = \frac{\eta\lambda}{d} \tag{5.1}$$

The nanograting is made of free-standing silicon nitride developed from a silicon frame by achromatic lithography.[6, 7] Three "windows" each expose an area of the nanograting

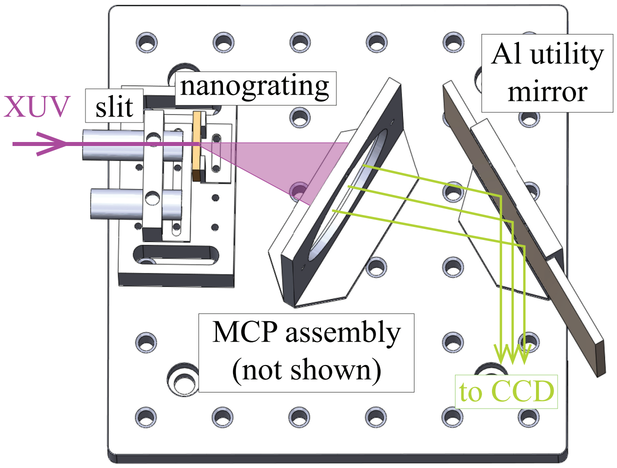

Figure 5.3: Schematic of the XUV analyzer, with the beam path indicated. Note that only the MCP assembly holster is pictured.

to be used in the spectrometer. These windows are 0.5mm × 4.5mm and are spaced by 2mm. The support has a period of 1.5μm and bars that are ∼0.17μm wide; these run approximately perpendicular to the nanograting.[4] The small period of the grating affords a sub-nm resolution at wavelengths of tens of nanometers.[6, 7] Notably, the incident XUV light will diffract off of the support grating, resulting in crescent shaped diffraction patterns. These are described in detail in Reference [5] The nanograting is pictured in Figure 5.4.

The diffracted XUV beam is then collected on a 2" ø MCP matched-set chevron with a P-43 phosphor screen detector (Beam Imaging Solutions, BOS-40-IDA-CH-MS). The MCP pore size is 25μm in diameter. The detector is angled by 30° relative to the nanograting and supported by custom aluminum holsters (see Appendix C). XUV photons are sufficiently energetic to cause an electron cascade in the MCP. Light emitted by the phosphor screen is then sent out of vacuum by an enhanced aluminum utility mirror and onto a digital camera for analysis. The analysis procedure is described in the dissertation of Camila Bacellar C. Silveira.[4] The mirror was purchased from Newport (75J00ER.3) and cut to size (2" × 4") with a diamond blade in the College of Chemistry machine shop.

By interchanging a series of thin metal foils (Lebow Company)[5] before the nanograting, the harmonics can be identified. These foils act as filters, blocking the residual driving laser light, and are only transmissive to a certain range of XUV energies. A selection of filters and their transmission regions can be found in Table 5.1. A 2-3/4" CF half nipple welded to the

---

[4] The bars block ∼11% of the signal.

[5] Foils are mounted on LS-Lebow standard UHV sandwich rings.

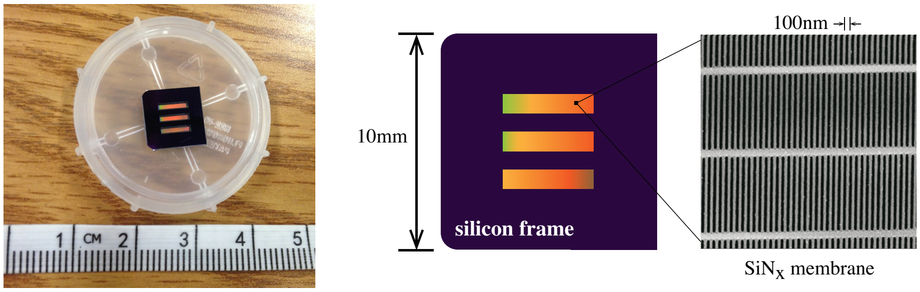

(a) Nanograting (b) SEM image of nanograting

Figure 5.4: (a) Picture of the transmission nanograting in storage container, with metric measuring tape for reference and (b) top view schematic with the scanning electron micrograph of the SiN$_x$ grating.

Foil	Al	Zr	Sn	In
Transmission (eV)	20-100	60-210	130-550	140-500

Table 5.1: Approximate transmission ranges for select 0.2μm thick thin metal foils.[8] Note that the foil thickness will depend on the total incident photon flux.

XUV input arm of the chamber serves as a feedthrough for the filters, which are holstered and attached to a push-pull mount.

The entire XUV analyzer assembly is mounted on a vacuum-compatible 2” travel linear translation assembly. Rough alignment is achieved by a 2” travel standard linear motion feedthrough (MDC Vacuum, 660006) and fine adjustment is achieved by a vacuum-compatible picomotor piezo actuator (Newport, 8302-V); each is coupled to a vacuum-compatible single-axis translation stage (Newport, custom). When the XUV spectrometer is not needed, it is simply moved out of the beam path. To operate this analyzer as a beam profiler, the stage is moved so that the entire XUV beam bypasses the nanograting and is incident on the MCP chevron stack. Maximizing the intensity of the beam profile is a good first step for SIGC optimization.

5.4 Harmonic Selection and Pump-Probe Recombination

To acquire XUV LPES data that can be interpreted, a single harmonic must be selected for the probe. If the entirety of the generated XUV spectrum acted as a probe pulse, one state would be represented by several peaks, each corresponding to a different detachment harmonic. This can be experimentally accomplished by several means—including by implementation of a transmission grating monochromator[9] or multilayer mirrors (MLMs). We have opted to implement a MLM because of its simple geometry and ease of alignment.

Multilayer mirrors comprise nanolayers of alternating materials with high and low refractive indices and atomic numbers.[10] As such, MLMs act as interference reflectors, where the layer thicknesses and angle of incidence are optimized to fulfill the Bragg equation for some peak wavelength, λ_{max}. This is given by Equation 5.2, where m is the order of the reflection, n is the refractive index, θ is the angle of incidence, and $d = d_A + d_B$ is the structure period for materials A and B of thicknesses d_A and d_B, respectively. A schematic of a MLM is also shown in Figure 5.5.

$$m\lambda_{max} \approx 2ndcos\theta \tag{5.2}$$

Modern MLMs consist of tens to hundreds of alternating layers, and are commonly made of molybdenum and silicon (Mo/Si). An ideal Mo/Si multilayer with 100 layers will have a reflectivity near 70% for 80-120eV photons at a 90° angle of incidence.[11] This is the theoretical upper limit for the reflectivity of current Mo/Si MLMs.

Of chief interest to the XUV LPES application is the spectral bandwidth ($^{\lambda}/_{\Delta\lambda}$)—or selectivity—of the MLM. Although the reflectivity of MLMs is generally good, the selectivity can be problematic.[12] The bandwidth may include multiple harmonics, and if the reflectivity of the undesirable harmonic is too large, the MLM cannot fulfill its primary function. Two identical MLMs near normal incidence have been used by others to increase the selectivity ($<$ 10% contribution from neighboring harmonics), but the reflectivity drastically drops, often to under 10%.[13]

An active line of communication has been opened with Eric Gullikson at the Center for X-ray Optics at Lawrence Berkeley Laboratory.[6] He has suggested that, for our initial target regime of 20-100eV, a 45° angle of incidence MLM be selected. Consequently, we will first test if the selectivity of one MLM of this type is sufficient for the purposes of XUV LPES. This preliminary geometry is reflected in the apparatus scheme shown above in Figure 5.1.

After the harmonic is selected, it will be focused onto the liquid microjet with a toroidal mirror (ARW Optical Corporation) on a motorized, vacuum-compatible mount. Rather conveniently, the fundamental laser beam travels a roughly equivalent path as the XUV harmonics, and can be used for alignment purposes before pump down. To collinearly recombine the pump and probe arms, the OPA-generated UV pump will be sent into vacuum and reflect off of an annular mirror with a dielectric UV high-reflectance coating. The beam

---

[6] CXRO is a world leader in multilayer coating research and their databases are extraordinarily useful.

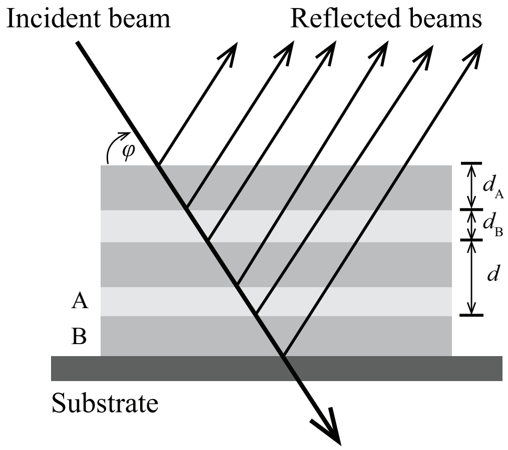

Figure 5.5: Schematic of a MLM, labeled in accordance with Equation 5.2. Adapted from Reference [10].

diameter of the XUV probe is significantly smaller than that of the UV pump, and will be sent through the hole in the center of the mirror. To protect the optics from frozen microjet debris, a gate valve will be implemented and a beamline skimmer is recommended.

5.5 References

1. Moore, J. H., Davis, C. C. & Coplan, M. A. *Building scientific apparatus* 4th ed. (Cambridge University Press, 2009).
2. Hosler, E. R. *Ultrafast strong-field vibrational dynamics dtudied by femtosecond extreme-ultraviolet transient absorption spectroscopy* PhD dissertation (UC Berkeley, 2013).
3. Attar, A. R. *Photochemical reaction dynamics studied by femtosecond soft X-ray transient absorption spectroscopy* PhD dissertation (UC Berkeley, 2016).
4. Bacellar C. Silveira, C. *Ultrafast dynamics in helium nanodroplets probed by XUV spectroscopy and X-ray imaging* PhD dissertation (UC Berkeley, 2017).
5. Kornilov, O., Wilcox, R. & Gessner, O. Nanograting-based compact vacuum ultraviolet spectrometer and beam profiler for *in situ* characterization of high-order harmonic generation light sources. *Rev. Sci. Instrum.* **81,** 063109 (2010).
6. Savas, T. A., Shah, S. N., Schattenburg, M. L., Carter, J. M. & Smith, H. I. Achromatic interferometric lithography for 100-nm-period gratings and grids. *J. Vac. Sci. Technol. B Microelectron. Nanometer Struct. Process. Meas. Phenom.* **13,** 2732 (1995).

7. Savas, T. A., Schattenburg, M. L., Carter, J. M. & Smith, H. I. Large-area achromatic interferometric lithography for 100 nm period gratings and grids. *J. Vac. Sci. Technol. B Microelectron. Nanometer Struct. Process. Meas. Phenom.* **14,** 4167 (1996).
8. *Center for X-ray Optics filter transmission engine* `http://henke.lbl.gov/optical_constants/filter2.html` (accessed November 22, 2017).
9. Von Conta, A., Huppert, M. & Wörner, H. J. A table-top monochromator for tunable femtosecond XUV pulses generated in a semi-infinite gas cell: Experiment and simulations. *Rev. Sci. Instrum.* **87,** 073102 (2016).
10. *X-ray data booklet* `http://xdb.lbl.gov` (accessed November 22, 2017).
11. *Multilayer coatings: A mini-tutorial* `http://henke.lbl.gov/multilayer/mltutor.html` (accessed November 22, 2017).
12. Gullikson, E. M. *et al.* Molybdenum/silicon multilayer components for high harmonic generation sources. *Appl. Opt.* **54,** 4280 (2015).
13. Zürch, M. *et al.* Real-time and sub-wavelength ultrafast coherent diffraction imaging in the extreme ultraviolet. *Sci. Rep.* **4,** 7356 (2014).

Part IV

Appendices

Appendix A

Principles of Ultrafast Lasers

A.0.1 Light Amplification by Stimulated Emission of Radiation

A laser is an optical device that amplifies light through stimulated emission to produce a highly directional, coherent source of radiation.[1][1, 2] Lasers can be operated in several different configurations, but this discussion will focus on continuous-wave (cw) and mode-locked lasers. Continuous-wave lasers are continuously pumped, and continuously lase. Mode-locked lasers emit a train of ultrafast laser pulses at some repetition rate.

Lasers can be simply constructed out of a gain medium, sandwiched between two mirrors, that is optically pumped to excite the medium. Initially, light is spontaneously emitted from the medium subsequent to excitation. Light propagating along the length of the cavity defined by the two mirrors is captured and used to stimulate emission in the medium. With each pass, successively more photons stimulate emission. If one mirror is ∼1% transmissive, the laser light can be extracted for experiments.

Spontaneous and stimulated emission can be described by Einstein coefficients.[3] If we assume that the ground state is given by $|1\rangle$ and the excited state by $|2\rangle$, these coefficients are given by Equations A.1 and A.2, where g_i is the degeneracy of state i, $h\nu$ is the photon energy, and c is the speed of light. B_{12} is absorption ($|1\rangle + h\nu \rightarrow |2\rangle$), B_{21} is stimulated emission ($|2\rangle + h\nu \rightarrow |1\rangle + 2h\nu$), and A_{21} is spontaneous emission ($|2\rangle \rightarrow |1\rangle + h\nu$).

$$B_{12} = \frac{g_2}{g_1} B_{21} \tag{A.1}$$

---

[1] "L.A.S.E.R." is an acronym for light amplification by stimulated emission of radiation.

$$A_{21} = \frac{8\pi h\nu^3}{c^3} B_{21} \tag{A.2}$$

To achieve lasing, a population inversion must be created and maintained in the gain medium. This occurs when more population is in the excited state than would be statistically populated according to a Boltzmann distribution. This distribution is given by Equation A.3, where N_i is the number of electrons in state i, E_i is the energy of state i, k_B is the Boltzmann constant, and T is temperature. The condition for a population inversion is defined by Equation A.4.

$$\frac{N_2}{N_1} = \frac{g_2}{g_1} e^{-(E_2 - E_1)/k_B T} \tag{A.3}$$

$$N_2 > \frac{g_2}{g_1} N_1 \tag{A.4}$$

A population inversion cannot be sustained in a 2-level system; hence, a 4-level system is often used. Many different types of materials can serve as a gain medium for a laser, including gas mixtures, dyes, semiconductors, and solid state media. For most modern femtosecond lasers—including the Astrella—the gain medium is titanium-doped sapphire (Ti:Al_2O_3, or Ti:Sapph). The relevant states in Ti:Sapph are given by Figure A.1.[4] Electrons quickly relax from vibrationally excited ${}^2E_g{}^*$ to thermalized ${}^2E_g$ and from vibrationally excited ${}^2T_{2g}{}^*$ to thermalized ground state, ${}^2T_{2g}$. Lasing occurs between ${}^2E_g$ and ${}^2T_{2g}{}^*$, where a population inversion can be maintained. The transition from ${}^2T_{2g}$ to ${}^2E_g{}^*$ can be continuously pumped.

The absorption and emission spectra of Ti:Sapph are pictured in Figure A.1a. Lasing is possible above ~670nm, and this broad lasing bandwidth allows Ti:Sapph to produce short pulses. This is consequent to the frequency-time uncertainty principle for a laser pulse given by Equation A.5, where the value of the constant C depends on the temporal shape of the pulse. For a Gaussian pulse, $C = 0.441$.[5] When this relation is equivalent, a pulse is said to be transform-limited.

$$\Delta\nu\Delta t \geq C \tag{A.5}$$

A.1 Ultrafast Lasers

Ti:Sapph cannot directly amplify a femtosecond pulse beyond peak powers of $10^{GW}/_{cm^2}$.[6] Above this limit, the crystal will burn and can no longer act as a lasing medium on the burn

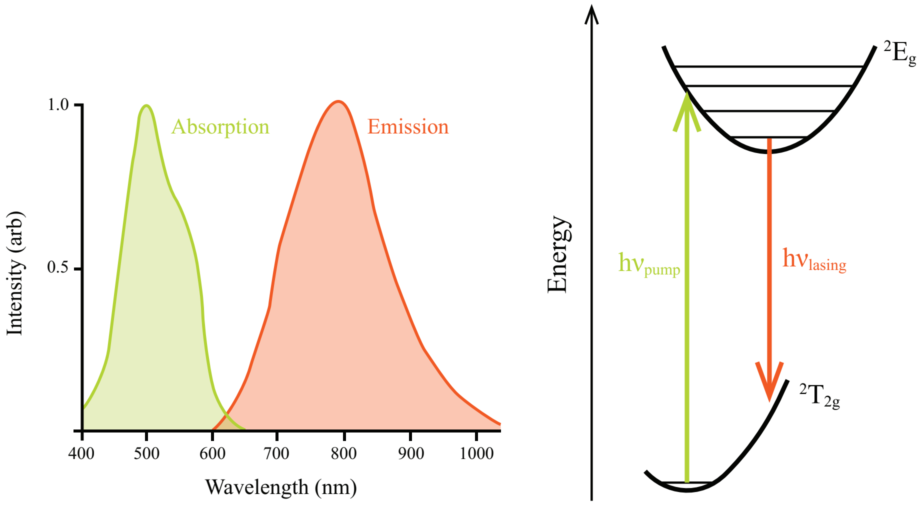

(a) Absorption and emission spectra (b) Energy level diagram

Figure A.1: (a) Ti:Sapph absorption and emission spectra, where lasing can only occur at emission wavelengths that do not overlap with the absorption region, and (b) the energy levels relevant to the lasing transition in Ti:Sapph. Adapted from [1] and [4].

spot. The Kerr lens effect—the non-linear effect whereby intense coherent light will modify the refractive index of a material and consequently self-focuses in the material—further aggravates this condition.[1] To circumvent damage while still amplifying the peak power beyond the damage threshold of Ti:Sapph, chirped pulse amplification (CPA) is used. This comprises three steps: 1) the "seed" pulse is stretched in time to reduce the peak power, 2) the seed is amplified, 3) the amplified pulse is re-compressed to its original pulse duration.[7] The seed pulse dictates the amplified laser pulse properties.

To generate the seed pulse, an oscillator is used. This is a laser which generates pulses through so-called "Kerr lens mode-locking."[1] Then, CPA is used to amplify the power of this pulse by orders of magnitude for use in experiments. Mode-locking occurs when the standing laser modes inside the oscillator cavity are forced into equal phase. This results in a wave interference pattern that generates an intense, short burst of light. If the oscillator is not properly mode-locked, the laser will be cw. Kerr lens mode-locking uses the Kerr lens self-focusing phenomenon to suppress cw operation and establish stable mode-locking.[2] Kerr lens mode-locking is illustrated in Figure A.2 and the repetition rate, τ, is given by Equation A.6, where L is the cavity length.

---

[2] Generally, oscillators are either passively or actively mode-locked. In active mode-locking an acousto-optical modulator or electro-optical modulator is used to sustain mode-locking.

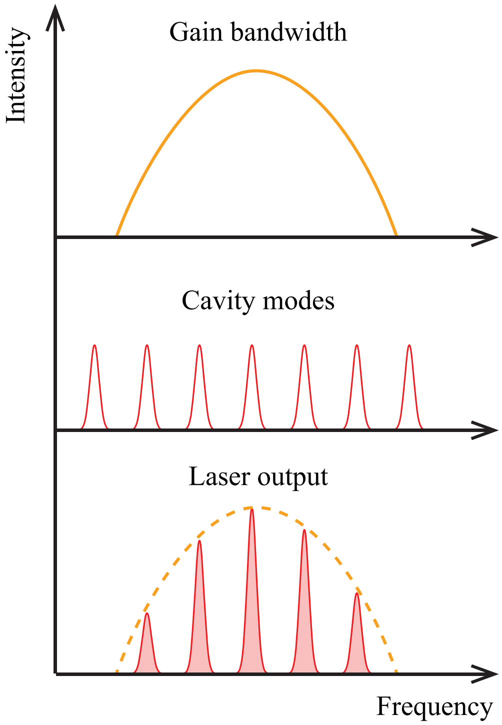

Figure A.2: Principles of Kerr lens mode-locking. The gain bandwidth is the frequency region that the cavity can mode-lock, the cavity modes are all possible modes, and the laser output is the modes which are selected through Kerr lens mode-locking. Adapted from Reference [1].

$$\tau = \frac{c}{2L} \tag{A.6}$$

Pulses are stretched and re-compressed with the aptly named stretcher and compressor components, which are typically gratings. These can be single gratings or pairs of gratings, and can be reflective or transmissive. Regardless, the stretcher and compressor are matched so that the compressor can undo the work of the stretcher once the pulse is fully amplified. The gratings change the pulse duration by introducing group velocity dispersion (GVD)—or "chirp"—into the pulse. Group velocity dispersion is the spectral separation of a pulse in time and the grating accomplishes GVD through spectral dispersion. When a pulse is "negatively chirped," the red edge leads the blue edge (see Figure A.3).

Once the seed passes through the stretcher, it will be sent to the amplifier. Amplifier cavities come in many designs, but can generally be either classified as regenerative or multi-pass.[1, 5] This discussion will focus on regenerative amplifiers (regens), like the Spitfire and

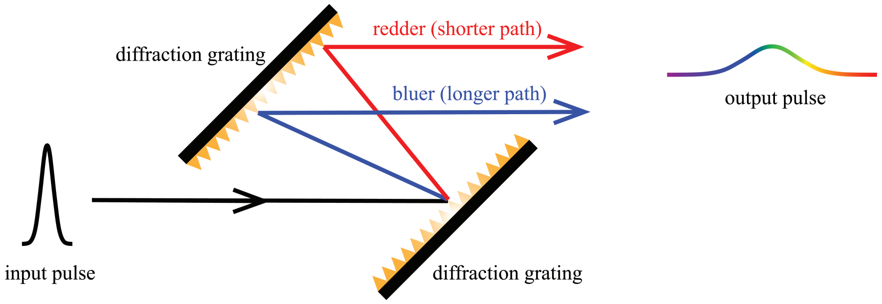

Figure A.3: Schematic of how a stretcher assembly introduces negative chirp.

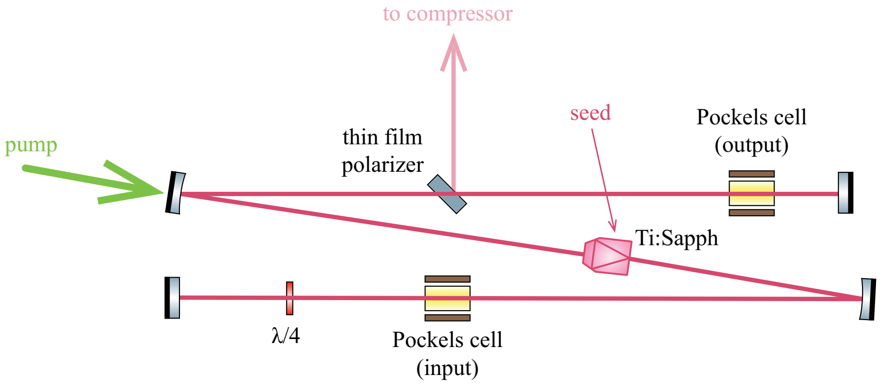

Figure A.4: Example regen design. The first Pockels cell picks the input pulse by flipping the polarization of the seed so the pulse is trapped in the cavity. After some time, the second Pockels cell flips the polarization of the amplified light so that it will reflect off of the the thin film polarizer and be sent to the compressor. The cavity beam path, and the input locations of the pump and seed beams, are indicated. Adapted from Reference [4]

Astrella.[3] A simple regen design is given in Figure A.4.

Pulses are trapped in a cavity by their polarization, which can be rotated by a Pockels cell—an electro-optic device that acts as a $^1/_4$-waveplate when a high voltage is applied.[1, 5] A thin film polarizer and one or more Pockels cell can be used both to let a seed pulse in for amplification, and subsequently kick the amplified pulse out to be re-compressed. Pockels cells do not perfectly pick pulses—a small fraction of the previous and subsequent pulse in the pulse train often leak out. The Pockels cells are birefringent, and this ultimately limits the contrast ratio of the main pulse to the pre- and post-pulses. A contrast ratio of 1000:1 and 100:1 are expected for the main pulse to the pre- and post-pulses, respectively.

Pulses are picked-off and sent to the compressor after they have made enough round trips

---

[3] The KM Labs Dragon used in the gas-phase TRPES project is a multi-pass amplifier.

to reach maximum gain. After this point, each successive pass in the cavity results in losses that reduce the total gain. Generally the pulse with the highest intensity gives the best power, but the pulse after this in the cavity pulse train gives the most stable output with minimal power losses. A well aligned cavity will have the smallest possible build up time (*i.e.* require the fewest number of passes to reach gain saturation).

A.2 Alignment Notes for New Ultrafast Laser System

A.2.1 Astrella

Much of the Astrella is closed-box,[4] and, as such, the Verdi-G, Revolution, Vitara, and stretcher/compressor components cannot be self-serviced. However, the Vitara output, Revo output, and Astrella cavity can be aligned and characterized. The diagnostic and alignment procedures for the Verdi, Revolution, and Astrella amplifier cavity are provided below.

The Verdi-G is a 5W pump laser, that is set to 3W. Pumped at 3W, the Vitara oscillator should give ∼200mW of seed into the stretcher unit. The Astrella can be seeded with as little as 10mW, but an order of magnitude more power is typical. The alignment of the seed into the stretcher and cavity regions is straightforward. Two mirrors before the stretcher module can be used to align the seed onto an iris into the stretcher and a cross hatch at the opposite side of the module. This cross hatch catches a higher-order dispersion off of the stretcher grating. To align into the cavity, the two steering mirrors at the stretcher module exit are aligned onto preset irises.

A beamsplitter before the stretcher diverts some of the Vitara beam to an output port which can be uncovered so the seed can be analyzed when necessary. Notably, the Vitara specrum is normally double-bumped. Part of the 800nm is blocked so it does not dominate the spectrum and a wider bandwidth (∼85nm) can be achieved. Finally, the Vitara is the master trigger for the entire experiment, and runs at 80MHz. The fast photodiode inside the oscillator is hooked into the back of the synchronization and delay generator (SDG) box. If this is hooked into an oscilloscope, the amplitude of the peaks should be above 500mV, otherwise the bandwidth detector interlock will be triggered and the rest of the system will turn off.

The Revolution threshold is ∼10.5A; lasing in the Astrella cavity begins around 12-15A. An internal power meter provides a constant power readout on the Revolution software, but,

---

[4] *i.e.* void warranty if opened

because this includes the afterburner, the reported value is ∼2W higher than the actual power. To measure the power out, a frosted mirror has been provided and is bolted next to the Revolution. This can be moved into the beamline at the Revolution output and act as a pick-off mirror so the power can be accurately measured. The Revolution is a slave to the Vitara, and is triggered off of channel D4 on the SDG. Finally, the Revolution cavity has a transit time of 9ns, while the Astrella amplifier cavity has a transit time of 12ns. About 14 round trips, or about 132ns of build-up time, are required in the amplifier.

Below is a brief summary of some important notes on the Astrella's amplifier cavity.

- The amplified spontaneous emission (ASE) and burn-in reduction time should always be checked when the amplifier cavity is re-aligned or the power out is low but the seed alignment looks good. To measure these, block the seed *after* the stretcher and open up the timing on the second Pockels cell until the power of the ASE is equivalent to the seeded power, when both are measured into the compressor. The burn-in reduction time on a good cavity alignment should be ∼35ns. Slight ridging in the ASE spectrum is normal, and is caused by the Pockels cells.
- Whenever the amplifier cavity has been realigned from scratch, the delay on the second Pockels cell should be closed down to ∼30ns to keep the power low when realigning the compressor. This protects the gratings in the compressor unit from accidental burns. The Astrella output just barely passes through the compressor unclipped. If the very edges image the grating, the alignment is acceptable.
- The pre-pulse contrast is 1000:1 for this system. The post-pulse contrast is 100:1.
- Before the output of the Astrella is sent through a beamsplitter, it must be expanded and collimated. Any passage through transmissive optics for such short-duration, high-energy pulses can cause self-phase modulation and GVD that can considerably distort the pulses. These effects can be mitigated by expanding the beam diameter with reflective telescope optics.
- To align the amplifier cavity, first align the seed with the irises, then tweak on the cavity end mirrors for the most efficient buildup in the cavity. This can be measured by hooking the amplifier photodiode into an oscilliscope. Then, the Revolution pump and afterburner can be aligned for the best power. The power should be ∼9.3W as measured before the iris into the compressor.

A.2.2 White-Light TOPAS-Prime with NiRUVis Extension

The purpose of this section is to elaborate on alignment procedures for the TOPAS-Prime. The beam layout and a description of the operation of the TOPAS-Prime can be found in its user's manual (p.p. 19-29), and is not reproduced herein. This discussion will adhere to the labeling convention for various optics that is established in the manual.

A.2.2.1 Alignment Notes for a Quick Tune-Up

1. Align the pump onto the removable pinhole after NC2 with the first telescope lens (labeled T3) into the TOPAS-Prime.
2. Align the white light continuum (WLC) onto the same pinhole with the turning mirror into the unit (labeled WL).
3. Tweak the alignment for power and far-field alignment with M5. If needed, tweak DM3 to improve the fresh pump alignment.

A.2.2.2 Full Alignment Notes

1. Check the rough alignment into the TOPAS-Prime and adjust it with the two telescope lenses (T3 and T4) and WL directly before the unit. Keep the flag down, and dial down the power out of the Astrella if the alignment is potentially dramatically off. The beam diameter should be 11mm into the TOPAS-Prime.
2. Align the first pass: Block the first pass pump before L5, and verify that the WLC is centered onto A2. The WLC should be focused in NC1. Then, unblock the first pass pump and verify that it is focused after NC1. L5 can be moved to adjust the focus. Tweak M3 and M4 as needed to align the pump onto the WLC. Finally, move the flag in front of M5 as needed. Only the signal should pass the flag, if the pump passes it could damage M5. Check the alignment at 1300nm and 1500nm, as the position of the signal onto M5 will be slightly different for each.
   a) Note that the pump and the WLC are non-collinear.
   b) The first stage amplification generates the WLC and impacts the output power greatly. If the output power drops significantly when the signal is tuned between 1300 and 1500nm, the alignment of the first pass is not good.
   c) After M5, there should be 2-3mW of seed at 1300nm, and ~1mW at 1500nm.
3. Use M5 to align the seed onto NC2, and use DM1 for power after NC2. At 1300nm, there should be ~2mW of signal. The seed should be uniformly bright and pass through NC2 without significantly clipping.
4. Align the second pass: Use M8 to align the second pass pump onto the removable pinhole after NC2. To align the second pass pump onto the seed signal in the far field,

use DM2. The manual delay of M8 will need to be tweaked for the best temporal overlap by looking at the intensity of the far field output.

   a) At 1300nm, there should be ~320mW after the second stage amplification; at 1500nm, the power should not change by more than 30mW.

5. Align the fresh pump: Remove the external set screw to access M15. Use M15 to align the fresh pump to the TOPAS-Prime output at the entrance of the NiRUVis Extension unit. Then, use DM3 to align the pump and TOPAS-Prime output at the exit of the NiRUVis Extension. When the two beams are spatially overlapped, move the fresh pump delay (M16/M17 retroreflector) to optimize power. The Astrella compression or the mixing crystal angle may also need to be tweaked.

   a) To filter out the sum frequency signal, the 400nm high-reflector can be put into the NiRUVis Extension.

A.3 Pulse Characterization

Characterization of laser pulses is critical to time-resolved experiments. To meaningfully report a lifetime, τ, the pump-probe cross-correlation, σ, must be shorter than τ. Moreover, the temporal profile of the pulse can act as a diagnostic tool for the laser system. There are a number of techniques we employ to characterize our pulses, including cross-correlation and frequency-resolved optical gating (FROG) measurements.

A.3.1 Autocorrelation, Cross-Correlation and FROG

To measure the pulse duration of ultrafast lasers, the pulses are typically used to measure *themselves*.[8] The simplest device used to perform such a measurement is an intensity autocorrelator.[9] Here, the input pulse is split into the two arms of a Michelson interferometer by a beamsplitter. The arms are delayed relative to each other by the interferometer and then non-collinearly recombined inside a non-linear crystal to frequency-double the pulses by second-harmonic generation (SHG). The intensity of SHG depends on the temporal overlap of the two pulses, according to Equation A.7, where $I_{(auto)}$ is the time-dependent intensity of the frequency-doubled light, *I(t)* is the time-dependent intensity of the input light, and $t^{'}$ is the relative time delay.

$$I_{(auto)}(t,t^{'}) \propto I(t)I(t-t^{'}) \tag{A.7}$$

However, the diode array detectors inside most autocorrelators are too slow to record this in real-time, and instead they measure the intensity convolution, $A(t^{'})$, given by Equation A.8. This is the intensity "autocorrelation".

$$A_{(auto)}(t^{'}) = \int_{-\infty}^{\infty} dt I(t) I(t - t^{'}) \tag{A.8}$$

This is called a "cross-correlation" if the pulses are not identical (e.g. not the same wavelength). $A(t^{'})$ is now described by Equation A.9, where subscripts a and b denote the different pulses.

$$A_{(cross)}(t^{'}) = \int_{-\infty}^{\infty} dt I_a(t) I_b(t - t^{'}) \tag{A.9}$$

Importantly, if we assume that the pulses have a Gaussian temporal profile, then the convolution will return a Gaussian whose width[5] (variance, σ) is described by Equation A.10, where σ_{cross} is the width of the cross-correlation and σ_a and σ_b are the widths of pulses a and b, respectively.

$$\sigma_{cross}^2 = \sigma_a^2 + \sigma_b^2 \tag{A.10}$$

As we have seen, in order to return meaningful information about the pulse width, we must assume a pulse shape (e.g. Gaussian, sech). This is a major shortcoming of the autocorrelation technique. Furthermore, this approach cannot provide insight into pulse distortions; we employ FROG to obtain this information.

FROG is an autocorrelation measurement that is spectrally resolved—the time and frequency domain measurements are made simultaneously.[10] The intensity of a FROG trace is given by Equation A.9, where $E(t)$ is the time-dependent laser field of frequency ω.

$$I(\omega, t^{'}) = \left| \int_{-\infty}^{+\infty} dt E(t) |E(t - t^{'})|^2 e^{-i\omega t} \right|^2 \tag{A.11}$$

When the spectral and temporal profiles of the input pulse are measured in this way, the temporal pulse shape, the pulse width, the spectral bandwidth, and any chirp in the pulse can be recorded. Recovery of the intensity and phase information requires solving a

---

[5] Note, pulses are often reported by full width at half maximum (FWHM), where FWHM $= 2\sqrt{2ln(2)}\sigma$ or as the average single pulse duration, ${}^{FWHM}/_{\sqrt{2}}$.

2D phase-retrieval problem. A functional form is imposed on the pulse, typically by SHG, allowing for this problem to be uniquely solved.

Our project uses a GRating-Eliminated No-nonsense Observation of Ultrafast Incident Laser Light E-fields, or GRENOUILLE, *in lieu* of a traditional FROG. This design uses a Fresnel biprism and a thick SHG crystal instead of an interferometer and a spectrometer, respectively, but recovers the same information as a FROG in a much more compact and inexpensive design.

A.3.2 Finding Time Zero

For all TRPES experiments, two time-stamps must be measured: the time when the pump pulse first hits the microjet and the time when the pump and the probe pulses are maximally overlapped (time zero, or t_0). Determining when the laser hits the microjet is fairly straightforward. Light scatters off of the microjet and is energetic enough to cause an electron cascade on the MCP. Because this light travels faster than any electron, and because the scope only bins 2ns, we assume this electron cascade is a good estimate for the time when the laser pulse hits the microjet. We set the trigger for the scope (which is sent from the Astrella's SDG box) to be 16ns after this laser spike; this time delay must be re-added back when converting data from ToF to eKE.

To find time-overlap of the pump and probe pulses, the path length of each arm is first measured and adjusted to be roughly equivalent. Overlap can then be found in one of two ways. Conventionally, the UV pump and probe pulses are independently difference-frequency mixed with residual 800nm that is on a delay line at the entrance of the liquid microjet chamber. A thin window is set before the mixing BBO crystal (90μm, 45°) to account for the additional delay added from the entrance window of the liquid microjet chamber. The transmitted light is then spatially separated by wavelength with a Pellin Broca prism so the DFG signal can be readily seen. A thicker BBO can be initially used because it generates a brighter DFG signal. Because the TOPAS-Prime line is fixed, it is first mixed with 800nm. Once overlap is established between the two, the 800nm stage position is fixed and then mixed with the quadrupler or tripler arm, which is also on a delay line. Alternatively, time-overlap of the pump and probe can be found on the microjet itself. Solvated electrons are readily generated in aqueous solutions of 100mM potassium iodide and give strong signal near ToF 800ns when the pump and probe pulses are overlapped in space and time. This is often the preferred approach to finding t_0 because of its simplicity.

A.3.3 Instrument Response Function

The cross-correlation of the pump and probe pulses *is* the instrumental response function (IRF) in our experiment. Traditionally, we have directly measured this by independently difference-frequency mixing residual fundamental with the pump and probe pulses before the microjet trap chamber entrance window, as described above. By varying the delay time between one pulse relative to the other and measuring the intensity of the DFG light on a photodiode, we can recover the cross-correlation of two pulses. From these cross-correlations, we can back out the cross-correlation of the pump and probe together.[6] This process is often labor-intensive, particularly for the fourth harmonic. We can also fit our data, as described in Section 2.5, to return the IRF.

A.4 References

1. *Femtosecond laser pulses: Principles and experiments* 2nd ed. (ed Rullière, C.) (Springer, 2005).
2. Paschotta, R. *Field guide to: Lasers* (SPIE Press, 2008).
3. Hilborn, R. C. Einstein coefficients, cross sections, f values, dipole moments, and all that. *Am. J. Phys.* **50,** 982 (1982).
4. *Spitfire: Ti:Sapphire regenerative amplifier systems user's manual* (Spectra Physics, 2004).
5. Paschotta, R. *Field guide to: Laser pulse generation* (SPIE Press, 2008).
6. François Salin, J. S. & Piché, M. Mode locking of Ti:Al_2O_3 lasers and self-focusing: a Gaussian approximation. *Opt. Lett.* **16,** 1674 (1991).
7. Elkins, M. H. *Dynamics of electron relaxation studied using time-resolved photoelectron spectroscopy in liquid microjets* PhD dissertation (UC Berkeley, 2015).
8. *Swamp Optics: Tutorials* `http://www.swampoptics.com/tutorials.html` (accessed November 25, 2017).
9. *Swamp Optics tutorial: Intensity autocorrelation* `http://www.swampoptics.com/assets/tutorials_autocorrelation-2015.pdf` (accessed November 25, 2017).
10. *Swamp Optics tutorial: FROG* `http://www.swampoptics.com/assets/tutorials-frog-2015.pdf` (accessed November 25, 2017).

---

[6] Mixing the pump and probe directly in a BBO would require a non-physical angle.

Appendix B

Updated Code for Executable Computer Programs

B.1 Automated Background Scans

The original LabVIEW code (termed a virtual instrument, or VI) was written by Alexander T. Shreve, and is detailed in his dissertation. This code was then modified in early 2014 to enable automated background scans. A code flow diagram for the new block diagram components is presented in Figure B.1, and described herein.

To acquire data for each delay, the VI first compares the number of scans taken at a delay to the target number of scans. These values are located in the configuration table CSV file, which is updated by the VI after data is taken at each delay position. The vectors for the acquired and target number of scans are compared and the result is fed into a case structure. If the two vectors are not equal, the first stage position with the least number of scans is selected and the stage is instructed to move accordingly. If the stage position corresponds to the ASCII character “a”, “b”, or “c,” the background character is read and written to the Arduino UNO so the appropriate beam can be blocked. For all other stage positions, the code writes “0” to the Arduino UNO to instruct all servo motors to move to unblocked positions. For more details regarding the Arduino UNO and servo motors, see Section 2.4.

B.2 Arduino Servo Motors

Arduino Software is an open-source integrated development environment that allows the user to write programs (called sketches) and upload them to a microcontroller board. The

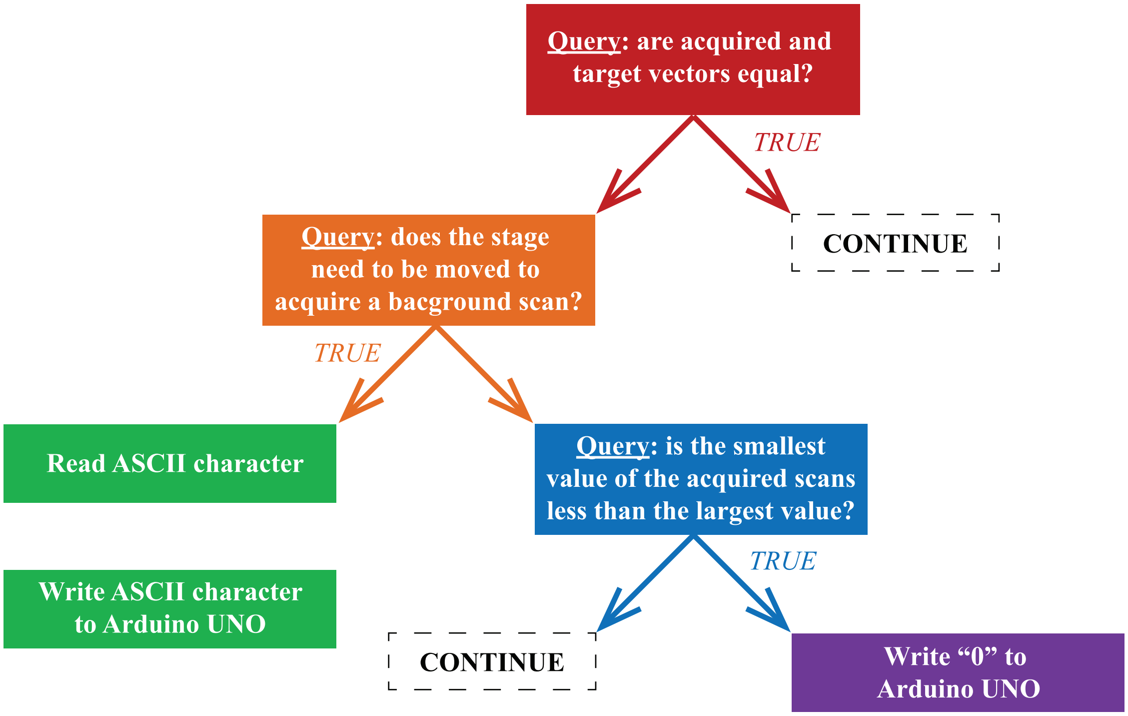

Figure B.1: LabVIEW code flow for automated background scans.

beam blocks are controlled by an Arduino UNO board.[1] This device has digital and analog I/O ports, a USB interface, and a 5V power pin. Three high-torque standard servo motors equipped with home-built flags are used to block laser pulses. The flags are rotated into and out of position by the drive shaft of a servo. The rotation of the shaft is determined by pulse width modulation signals sent from the UNO and can vary between 0° and ±90°. Servos run on 5V DC. Beam block positions are set to 45° because the mechanical stop mechanism at 90° introduces a slight jitter.

Below is the sketch that was written to the UNO to control these motors. Digital pinouts 9, 10, and 11 are attached to the servo objects and the motion of the motors is controlled through a switch statement. The LabVIEW data acquisition code will send an ASCII character to the UNO, and the servo motors will rotate to different positions based on the character received. Character "a" blocks beam 1, "b" blocks beam 2, and "c" blocks beam 3. When one beam is blocked, the other two servos are set to unblock their beams. All other characters will command all three beams to be unblocked.

---

[1] This device is commonly used by hobbyists interested in robotics and is inexpensive (∼30USD).

```
#include <Servo.h> // call the servo library

Servo beam1; // create a servo object to control each servo
Servo beam2;
Servo beam3;

void setup()
{
  beam1.attach(9); // attach servos on pins to servo object
  beam2.attach(10);
  beam3.attach(11);

  Serial.begin(9600); //connect to USB port

  // Initialize the servos to the baseline
  beam1.write(45);
  beam2.write(45);
  beam3.write(45);
}

// block and unblock beams one at a time with a switch statement
void loop()
{
 // get the number of bytes available to read from the serial port
 if (Serial.available() > 0)
 {
   int inByte = Serial.read(); //read incoming byte
   // choose between several discrete options
   switch (inByte)
   {
     case 'a' : // beam1 blocked
      beam1.write(135);
      beam2.write(45);
      beam3.write(45);
      break;
     case 'b' : // beam2 blocked
       beam1.write(45);
       beam2.write(135);
       beam3.write(45);
       break;
     case 'c' : // beam3 blocked
       beam1.write(45);
```

```
      beam2.write(45);
      beam3.write(135);
      break;
    default: // if nothing matches, unblock all
      beam1.write(45);
      beam2.write(45);
      beam3.write(45);
  }

  delay(15);
  Serial.write(inByte);
 }
}
```

Appendix C

Machine Drawings for New XUV Liquid Microject Photoelectron Spectroscopy Project

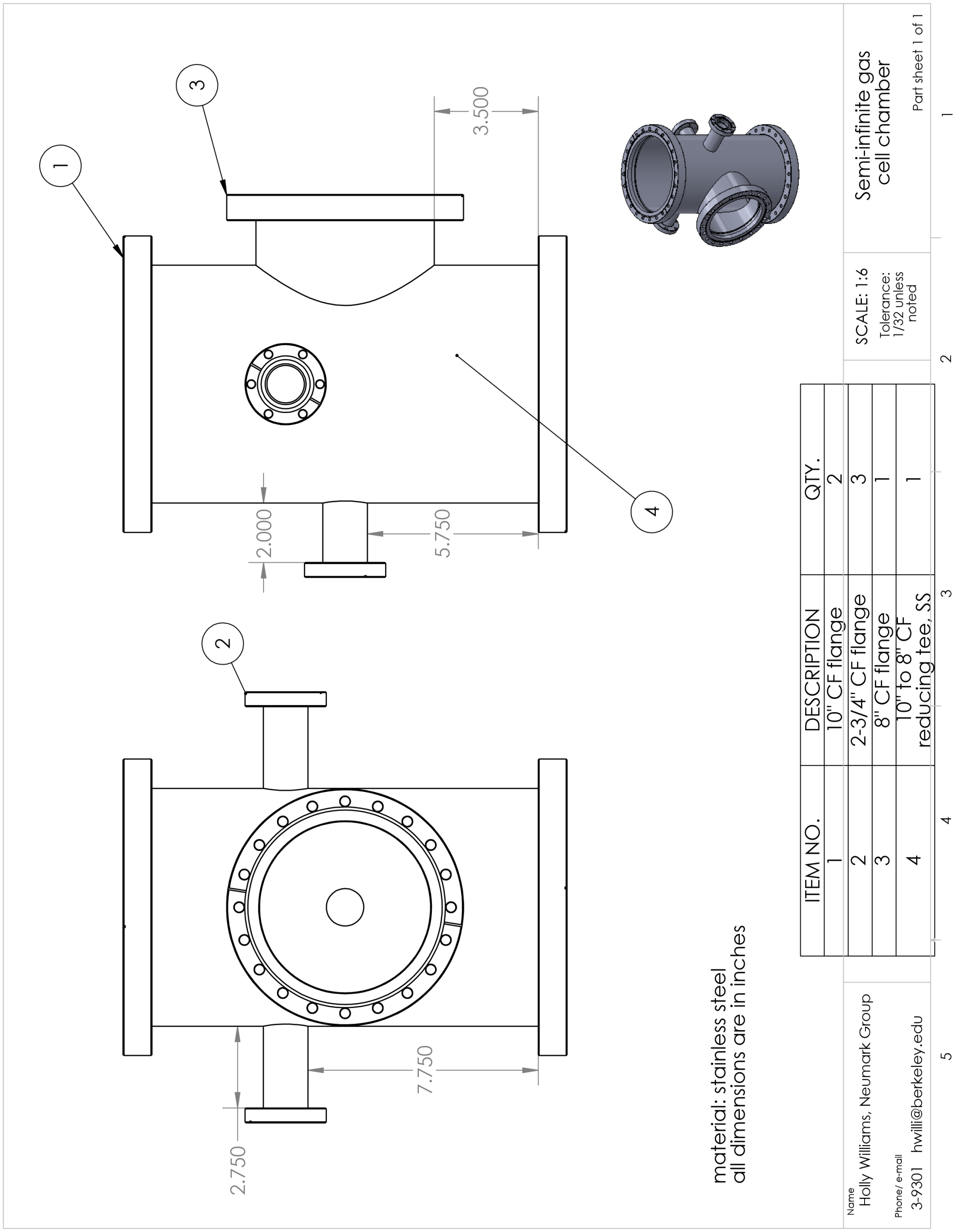

ITEM NO.	DESCRIPTION	QTY.
1	10" CF flange	2
2	2-3/4" CF flange	3
3	8" CF flange	1
4	10" to 8" CF reducing tee, SS	1

Figure C.1: SIGC vacuum chamber machine drawing. The 10” to 8” CF reducing tee was purchased with flanges, and the 2-3/4” CG half nipples were installed by the College of Chemistry machine shop. The bottom 10” CF flange is rotatable; all other flanges are fixed. All components are made from stainless steel (304 SS).

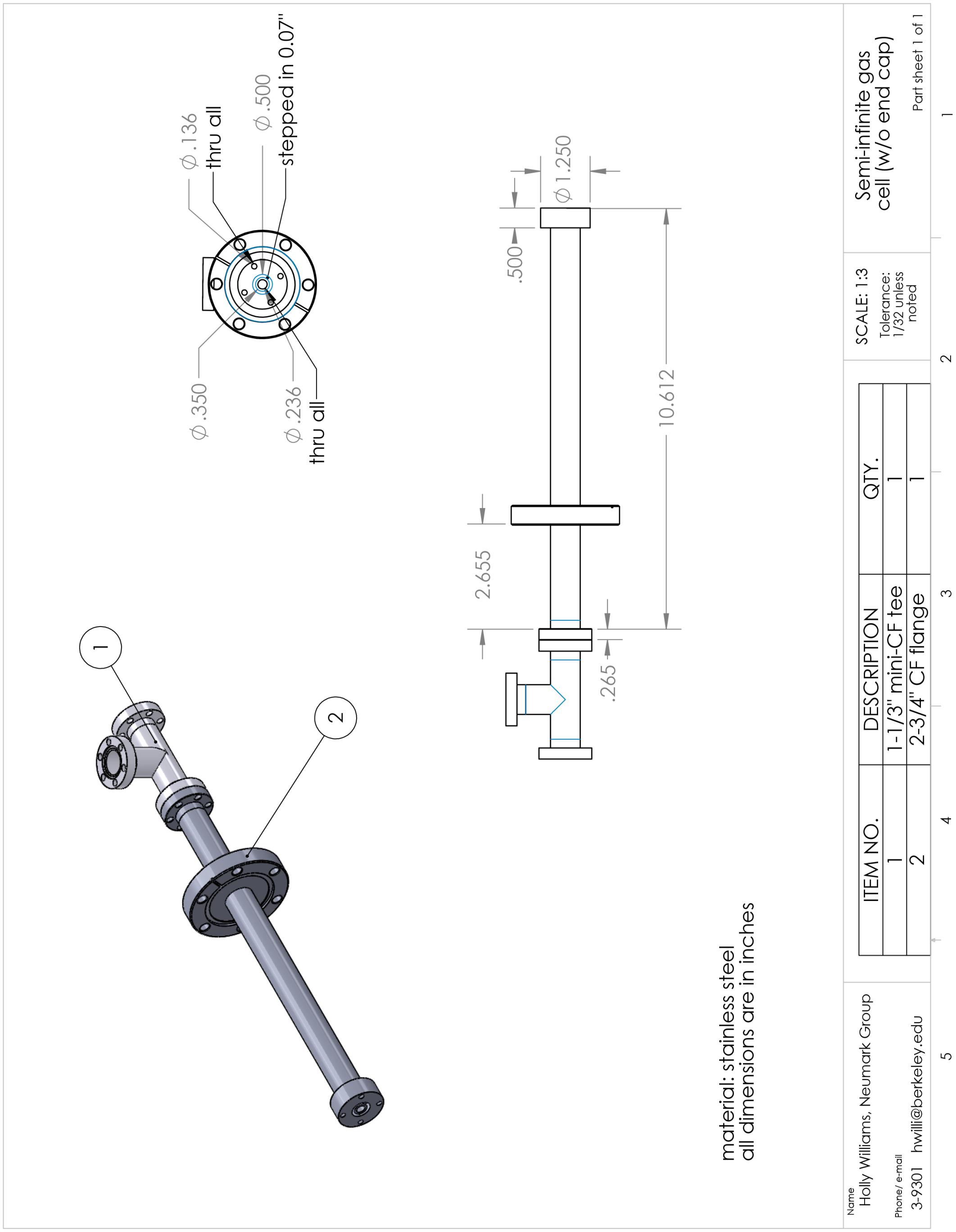

Figure C.2: SIGC machine drawing. The 1-1/3" mini-CF tee was purchased and used as is, and the 2-3/4" CF flange is rotatable. The end cap is pictured in Figure C.3. The cap is made from stainless steel (304 SS).

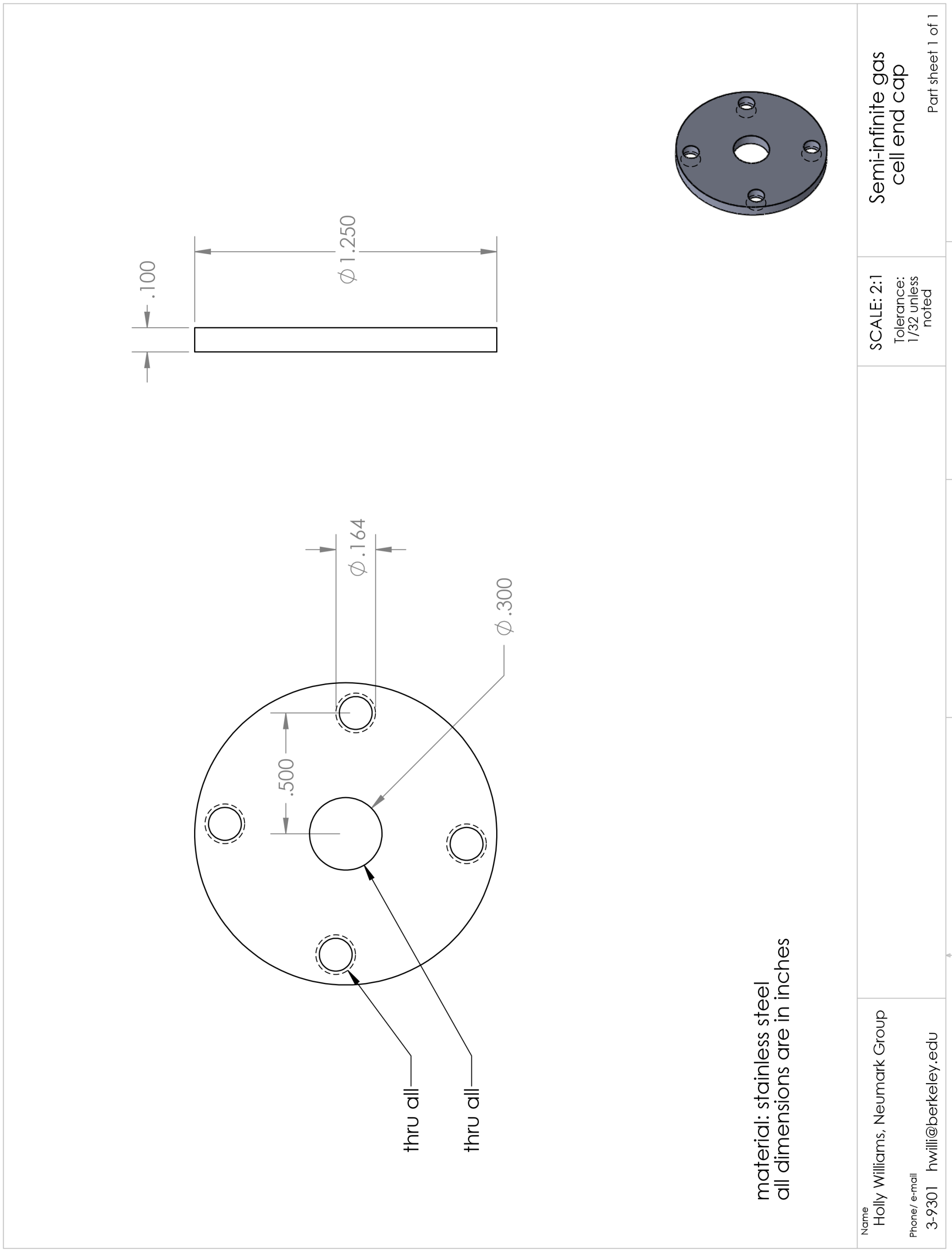

Figure C.3: SIGC end cap machine drawing, and is made from stainless steel (304 SS).

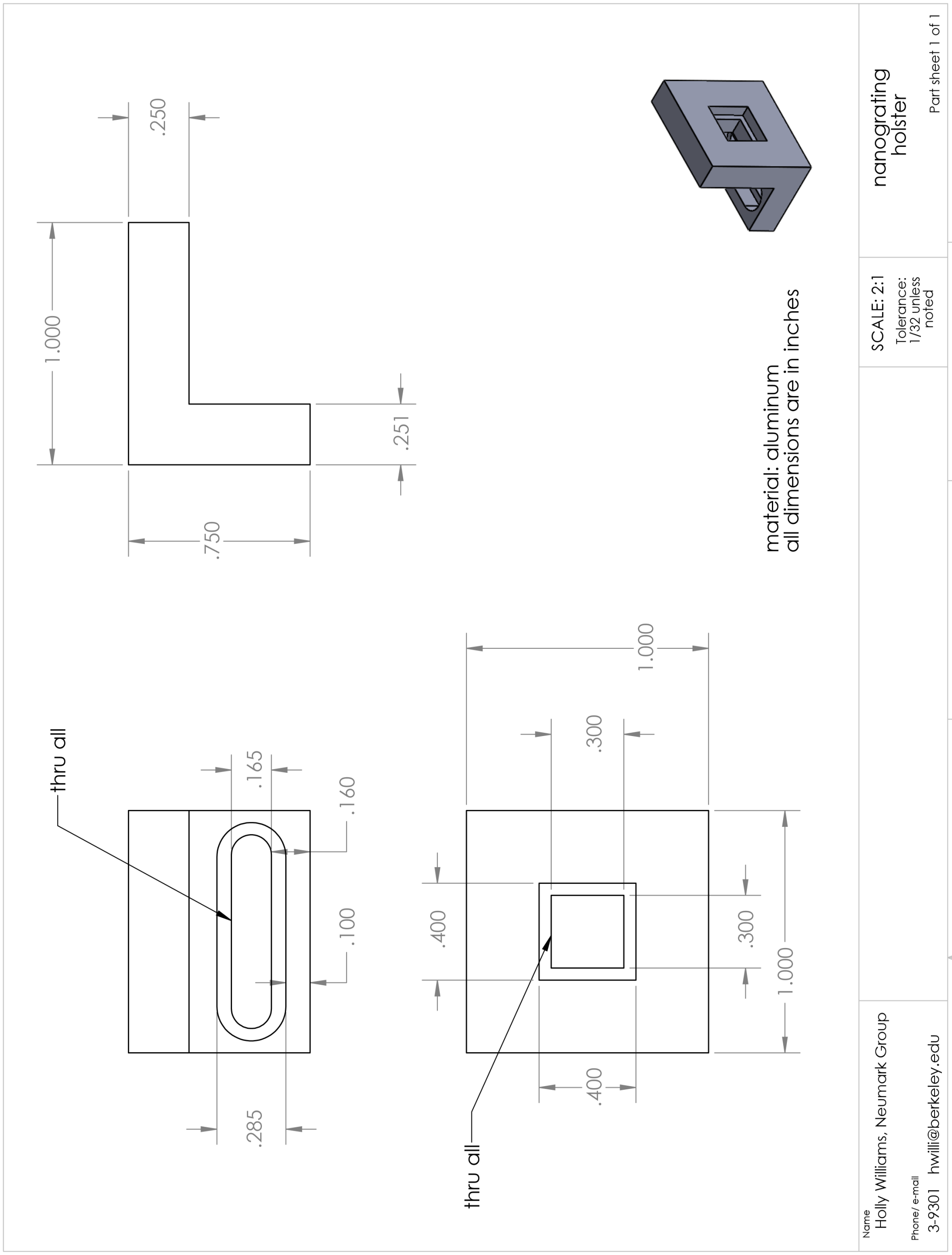

Figure C.4: Nanograting holster machine drawing. Tabs are drilled into the corners of the 0.4” × 0.4” shelf to house dabs of epoxy, which will be used to affix the nanograting to the holster. These are not shown in the drawing. The holster is made from aluminum.

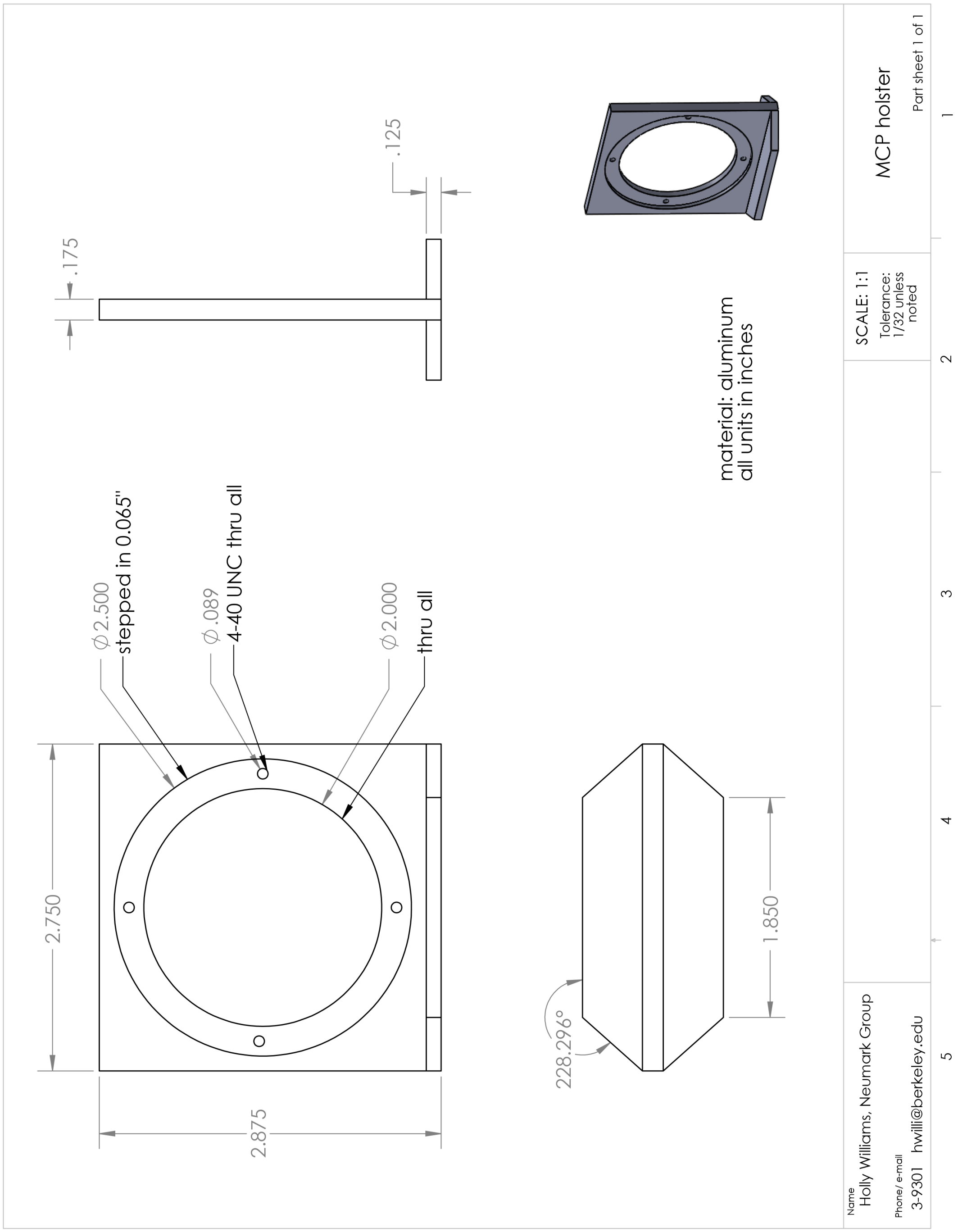

Figure C.5: MCP and phosphor holster machine drawing. Toe clamps will be used to fasten the holster to the breadboard of the stage. The holster is made from aluminum.

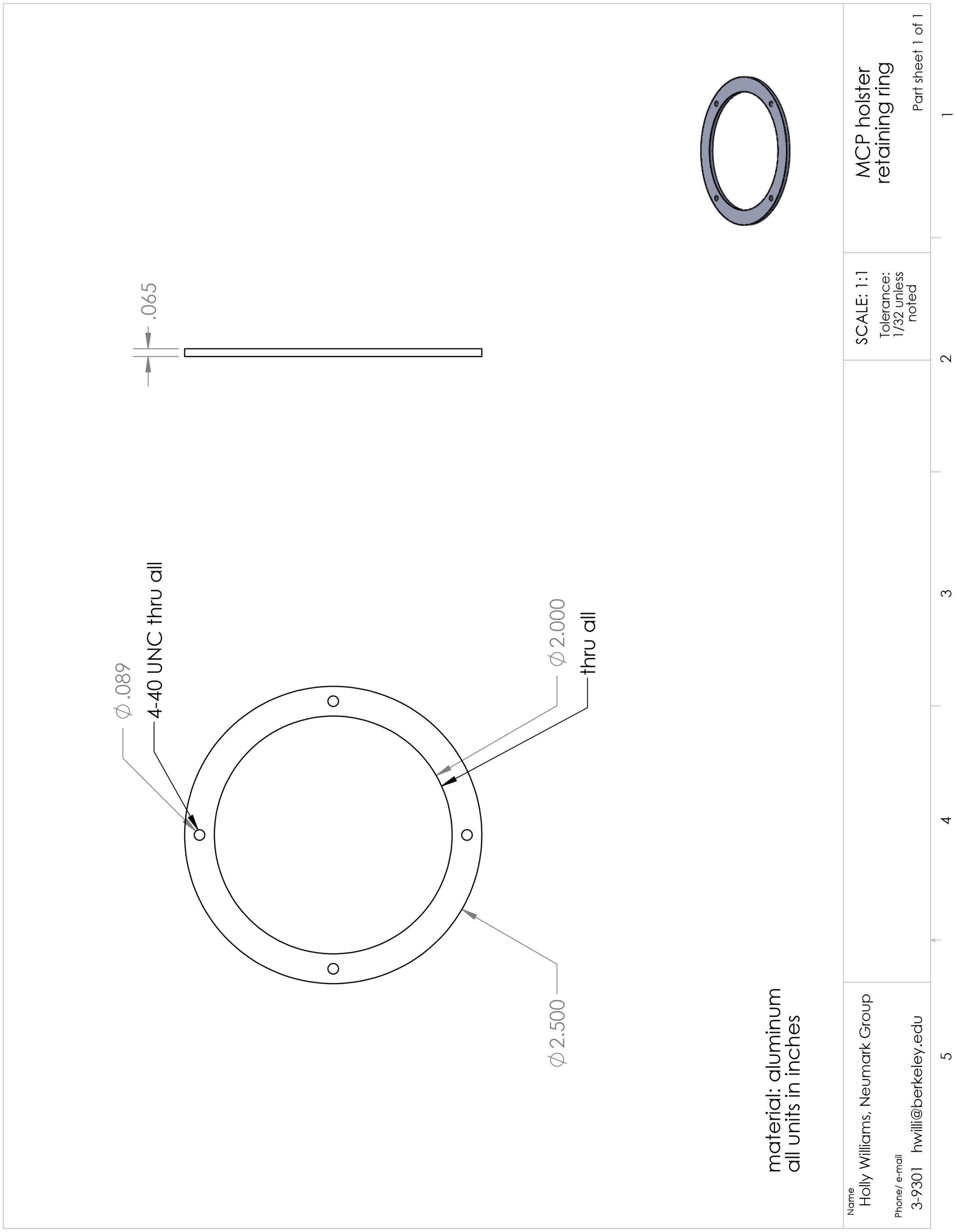

Figure C.6: MCP retaining ring, made of aluminum.

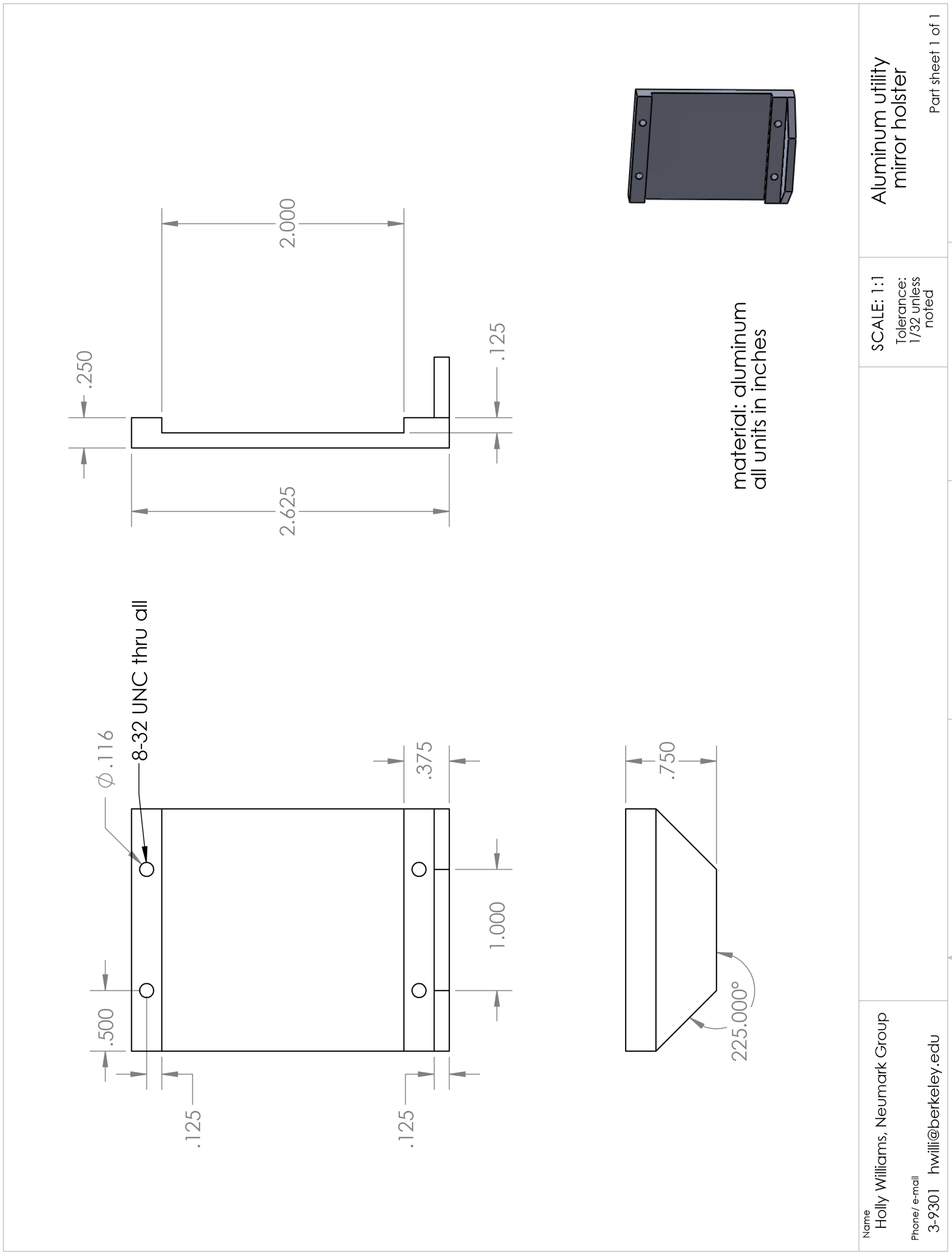

Figure C.7: The holster for the aluminum utility mirror. Two strips of Teflon sit over the 8-32 bolt holes to hold the mirror in place. Toe clamps will be used to fasten the holster to the stage breadboard. The holster is made of aluminum.

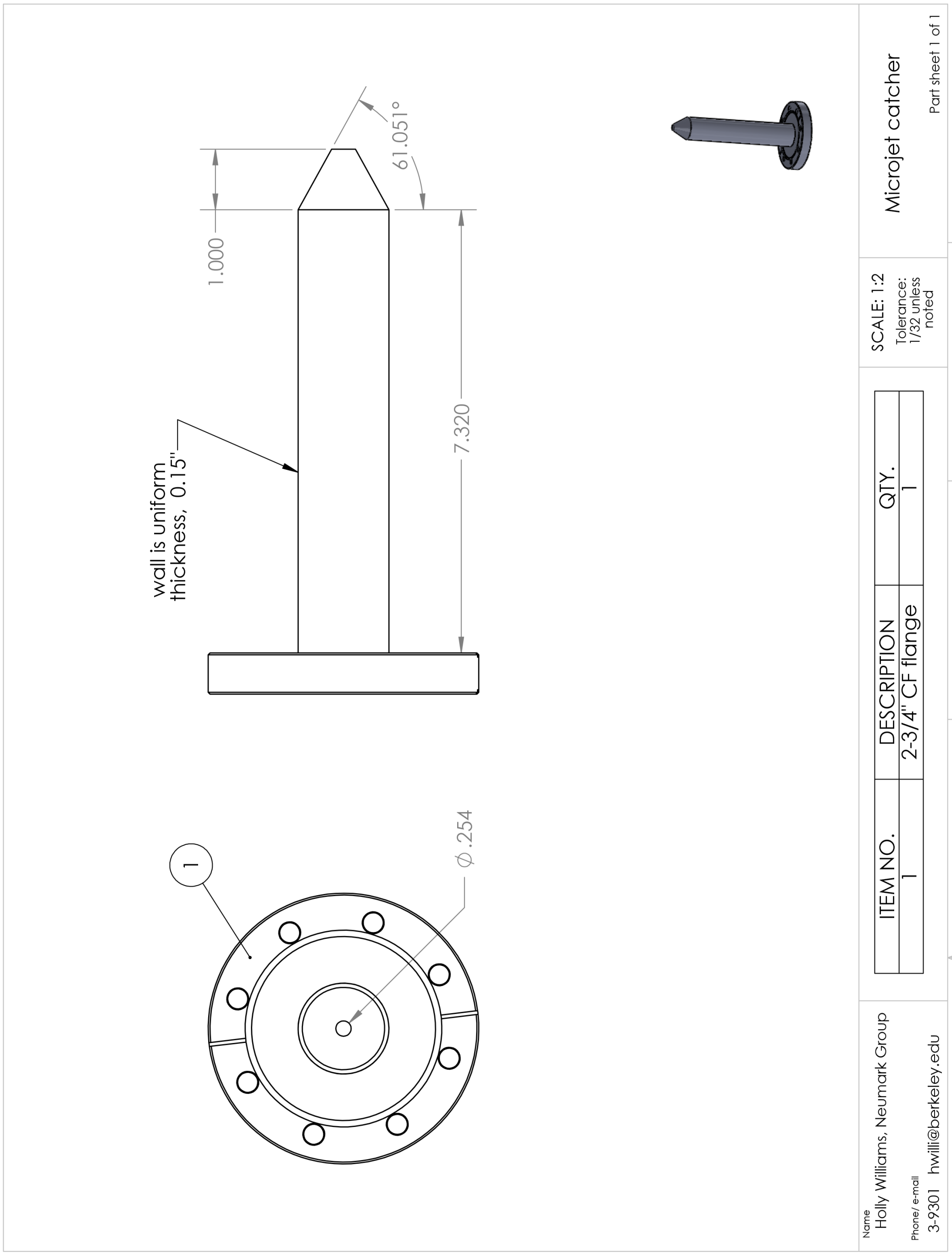

ITEM NO.	DESCRIPTION	QTY.
1	2-3/4" CF flange	1

Figure C.8: A microjet catcher made of stainless steel. When placed a few millimeters under the microjet to the catcher can reduce the pressure in the microjet chamber.

Appendix D

Publications from Graduate Work

1. Elkins, M. H., **Williams, H. L.**, Shreve, A. T. & Neumark, D. M. Relaxation mechanism of the hydrated electron. *Science* **342**, 1496 (2013).

2. Elkins, M. H., **Williams, H. L.** & Neumark, D. M. Dynamics of electron solvation in methanol: Excited state relaxation and generation by charge-transfer-to-solvent. *J. Chem. Phys.* **142**, 234501 (2015).

3. Elkins, M. H., **Williams, H. L.** & Neumark, D. M. Isotope effect on hydrated electron relaxation dynamics studied with time-resolved liquid jet photoelectron spectroscopy. *J. Chem. Phys.* **144**, 184503 (2016).

4. **Williams, H. L.**, Erickson, B. A. & Neumark, D. M. Time-resolved photoelectron spectroscopy of adenosine and adenosine monophosphate photodeactivation dynamics in water microjets. *In Preparation* (2017).

Appendix E

Acronyms

Ade Adenine. 47

Ado Adenosine. 17, 47

AMP Adenosine Monophosphate. 17, 47

ASE Amplified Spontaneous Emission. 89

BBO β-Barium-Borate. 40, 68, 93

BOA Born-Oppenheimer Approximation. 8

CD Circular Dichroism. 48

CF ConFlat. 25, 75

CI Conical Intersection. 5, 12, 48

CPA Chirped Pulse Amplification. 85

cw Continuous-wave. 83

DAS Decay Associated Spectrum. 37

DFG Difference-Frequency Generation. 41, 93, 94

DNA Deoxyribonucleic Acid. 2, 17, 46

eBE Electron Binding Energy. 7

eKE Electron Kinetic Energy. 7

FC Franck-Condon. 9, 48

FGR Fermi's Golden Rule. 8

FROG Frequency-Resolved Optical Gating. 91

FU Fluorescence Upconversion. 47

FWHM Full Width at Half Maximum. 34, 92

GLA Global Lifetime Analysis. 37

GVD Group Velocity Dispersion. 86

HHG High Harmonic Generation. 66

IRF Instrument Response Function. 36, 51, 94

ISC Intersystem Crossing. 4

MCP Microchannel Plate. 29, 77

MLM Multilayer Mirror. 79

NA Nucleic Acid. 3, 47

NB Nucleobase. 3

OPA Optical Parametric Amplifier. 42, 79

PEEK Polyether Ether Ketone. 22

PES Photoelectron Spectroscopy. 7

regen Regenerative Amplifier. 86

SDG Synchronization and Delay Generator. 88, 93

SFG Sum Frequency Generation. 40, 68

SHG Second Harmonic Generation. 41, 91

SIGC Semi-Infinite Gas Cell. 66, 71

TA Transient Absorption. 47

TD-DFT Time-Dependent Density Functional Theory. 49

Ti:Sapph Titanium-doped Sapphire. 84

ToF Time-of-Flight. 24

TRPES Time-Resolved Photoelectron Spectroscopy. 10, 47

UV Ultraviolet. 3

VBE Vertical Binding Energy. 10

VI Virtual Instrument. 95

WLC White Light Continuum. 42, 90

XUV Extreme Ultraviolet. 66

XUV LPES XUV Time-Resolved Photoelectron Spectroscopy on Microjets. 66, 73